Canicules et sécheresses en Méditerranée : contributions des processus couplés surface-atmosphère à méso-échelle

Marc Stéfanon

▶ **To cite this version:**

Marc Stéfanon. Canicules et sécheresses en Méditerranée : contributions des processus couplés surface-atmosphère à méso-échelle. Géophysique [physics.geo-ph]. Ecole Polytechnique X, 2012. Français. NNT : . pastel-00747124

HAL Id: pastel-00747124
https://pastel.hal.science/pastel-00747124

Submitted on 30 Oct 2012

HAL is a multi-disciplinary open access archive for the deposit and dissemination of scientific research documents, whether they are published or not. The documents may come from teaching and research institutions in France or abroad, or from public or private research centers.

L'archive ouverte pluridisciplinaire **HAL**, est destinée au dépôt et à la diffusion de documents scientifiques de niveau recherche, publiés ou non, émanant des établissements d'enseignement et de recherche français ou étrangers, des laboratoires publics ou privés.

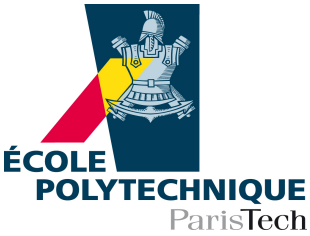

THÈSE

pour l'obtention du grade de Docteur de l'École polytechnique

spécialité : Physique

présentée par

Marc Stéfanon

Heat waves and droughts in Mediterranean : contributions of land-atmosphere coupled processes on mesoscale

Canicules et sécheresses en Méditerranée : contributions des processus couplés surface-atmosphère à méso-échelle

Thèse préparée au
Laboratoire de Météorologie Dynamique
Institut Pierre Simon Laplace

Soutenu le 1 octobre 2012 devant le jury composé de :

Président de jury :	M. Hervé Le Treut
Rapporteurs :	M. Jean-Christophe Calvet
	M. Pascal Yiou
Examinateurs :	M. Christophe Cassou
	M. Erich Fischer
Directeur :	M. Philippe Drobinski
Co-Directeur :	M. Fabio D'Andrea

THÈSE

pour l'obtention du grade de Docteur de l'École polytechnique

spécialité : Physique

présentée par

Marc Stéfanon

Heat waves and droughts in Mediterranean : contributions of land-atmosphere coupled processes on mesoscale

Canicules et sécheresses en Méditerranée : contributions des processus couplés surface-atmosphère à méso-échelle

Thèse préparée au
Laboratoire de Météorologie Dynamique
Institut Pierre Simon Laplace

Soutenu le 1 octobre 2012 devant le jury composé de :

Président de jury :	M. Hervé Le Treut
Rapporteurs :	M. Jean-Christophe Calvet
	M. Pascal Yiou
Examinateurs :	M. Christophe Cassou
	M. Erich Fischer
Directeur :	M. Philippe Drobinski
Co-Directeur :	M. Fabio D'Andrea

Remerciements

Ce manuscrit vient conclure 3 ans de thèse au sein du laboratoire de météorologie dynamique qui sont passés remarquablement vite. J'y endosse l'unique responsabilité de ses fautes d'anglais, choix de couleur hasardeux dans les figures et autres formulations douteuses. Pour le reste m'approprier la parenté exclusive de ce manuscrit serait une imposture et je tiens à exprimer sur cette courte page ma reconnaissance la plus sincère à celles et ceux qui y ont contribué de manière aussi infime qu'elle soit.

Celle-ci s'adresse d'abord à Philippe Drobinski et Fabio d'Andrea, pour m'avoir accompagné et formé tout au long de ces 3 ans. Bien que chacun ait son propre style, leur complémentarité et leur grande expertise scientifique ont fait que cette thèse est une réussite. J'espère pouvoir encore apprendre d'eux.

Cette association n'aurait jamais pu avoir lieu sans Bertrand Bessagnet, qui a permis que les bonnes personnes se rencontrent au bon moment et pour cela je l'en remercie.

Toute ma reconnaissance va également au GIS climat et à ceux qui sans me connaître ont fait confiance à ceux qui m'ont fait confiance.

Beaucoup d'autres ont contribué à cette thèse de par leur conseils avisés ou leurs aides techniques. Je pense notamment à mon comité de thèse, Agnès Ducharne et Robert Vautard, mais également à Cindy Lebeaupin-Brossier, Alessandro Anav, Martial Mancip, Nathalie de Noblet, Nicolas Viovy, Karine Béranger, Sophie Bastin, Jan Polcher, Christophe Lavaysse, Laurent Menut, Julien Lenseigne, Karim Ramage, Sophie Cloché, Florence Stéfanon.

Comme dans beaucoup de sociétés à structure pyramidale, on exploite et on est exploité. Je remercie Bénédicte et Solveig, le nec plus ultra des stagiaires, pour m'avoir permis de passer à l'échelon supérieur du système.

Une thèse ne serait pas vraiment une thèse sans son lot de nouvelles rencontres. Je voudrais remercier les « filles » du bureau pour l'ambiance chaleureuse, voir sub-tropicale, maintenant je vais devoir ressortir mes pulls. Plus particulièrement Nadia pour sa cuisine. Ludmila pour m'avoir appris qu'il faut toujours compter sur la Russie. Hiba, je m'excuse pour n'avoir pas beaucoup amélioré mon arabe en 3 ans.

Sur les sentiers tortueux de la procrastination j'ai rencontré un certain nombre de camarades, certains m'ayant suivi de manière fort inconsidérée dans X'Doc et ailleurs pour le meilleur et le pire, mais toujours dans la bonne humeur. J'ai une pensée spéciale pour Blaise, Gauthier, Hélène, David, Tatiana, Marie, Abdul, Louis, Julien Myosine, Alessandra, Xue, Alberto, Antoine, Morgan, Magali, Alberto, Jérôme, Amélie, Evgeny, Nayely, Nicolas, Paul-Étienne, Aurélie, Natacha, Grégory, Maud Andréa et Pauline. J'en oublie sûrement certain(e)s, qu'ils ne m'en tiennent pas rigueur.

J'adresse ma mention spéciale du jury à Claire, la voie de la sagesse, pour ses conseils et son assistance téléphonique 24/24 (mes onéreuses factures de téléphone en attestent).

Parfois au cours de la thèse, effectuer un retour au vert -à des choses simplement différentes- est

nécessaire. Merci à Louiset, Cambier, Racon, Elaudais E et N ; pour avoir amélioré l'ordinaire de la Grémuse.

Merci infiniment à toute ma famille, pour m'avoir soutenu sans faille tout au long de mon cursus universitaire, surtout mes parents, mes frère et sœurs, Florence, Pierre et Cécile.

Contents

Remerciements **3**

Contents **7**

1 Introduction **11**

2 Simulations of heat waves **23**
2.1 Simulations with the distributed version of WRF 23
2.2 Simulations with the MORCE numerical platform 26

3 Role of soil moisture during heat waves **37**
3.1 Heat waves classification over Europe and the Mediterranean region 37
3.2 The soil-moisture temperature feedbacks during heat waves at mesoscale 47

4 Impact of vegetation on the 2003 summer heat waves **67**
4.1 Effects of interactive vegetation phenology 67
4.2 Effects of anthropogenic land cover change 86

5 Conclusions and perspectives **101**
5.1 Conclusions 101
5.2 Perspectives 103

Bibliography **107**

Abstract

In a context defined as that of global warming, with fears that one summer out of two could be very similar to the 2003 European heat wave, the significant role played by droughts and land-atmosphere coupling in the enhanced and persistent high temperatures during heat-wave events has been highlighted by various studies.

I have developed an original classification based on the spatial structures of the heat waves ocurring in the Euro-Mediterranean area. Classification are generally designed to classify numerous events, so we have had to adapt to classifying rare events, by introducing three criteria grounded on temperature and the spatio-temporal extension of the phenomena to be described. The classification has enabled us to sort out six different categories of heat wave. In course of the investigation, I then proceeded to focus on one of the categories, id est on Westen Europe heat wave. I carried out numerical sensitivity tests in order to analyse how the hydric deficit of soils contributes to amplifying heat waves and was able to bring out different behaviours. In the continental plains, the atmospheric boundary layer temperatures are largely controlled by local dry convection processes. In the mountainous and coastal areas, mesoscale circulations such as slope winds and sea breezes contribute to mitigating heat waves by allowing fresh and moist air to advect and precipitations to form.

The effect of vegetation on heat waves was also examined. To do so, I have developed modelling tools which couple atmospheric dynamics with vegetative dynamics and thus present an innovative view on heatwave and drought conditioning processes in Western Europe. This modelling development is part of a larger project that aims at developing a model for regional climatic system and which has been undertaken at the Institut Pierre Simon Laplace (IPSL) as part of the MORCE-MED project. This question has so far been little addressed in the scientific literature.

I have shown that the inclusion of an interactive vegetation into modelling enable to simulate the modifications of the phenological cycle that control plant growth and development as well as evapotranspiration. Used to analyse the heat waves of June and August 2003, I have been able to demonstrate that the interaction of vegetation had a mitigating effect on the June 2003 heat wave, while it had a reversed effect in August, id est that of reinforcing. Lastly, we have measured the effects of land cover change that would allow to mitigate the consequences of heat waves on humans. In a preliminary study, I replaced anthropized surfaces (mainly agricultural land) by forests and meadows. There again, the effects noted were more contrasted than expected and presented a mitigation of the heat in June and an increase in the temperatures in August, with a high spatial variability on a mesoscale.

Résumé

Dans un contexte de réchauffement climatique où un été sur deux pourrait être similaire à l'été 2003, plusieurs études ont mis en lumière l'importance de la sécheresse et du couplage surface-atmosphère dans l'amplification et le maintien des fortes températures lors d'une canicule.

Au cours de cette thèse j'ai développé une nouvelle méthode de classification des canicules d'après leurs structures spatiales dans la zone Euro-Méditerranée. Les méthodes de classification, généralement conçues pour classer un grand nombre d'évènements, ont été adaptés aux évènements rares en introduisant trois critères portant sur la température et l'extension spatio-temporelle de la vague de chaleur. Cette méthode a permis d'extraire six classes distinctes de canicules. Mon analyse de processus s'est focalisé par la suite sur l'une de ces classes localisé en Europe de l'ouest. Un ensemble d'expérinces numériques de sensibilité a permis de mettre en évidence la contribution du déficit hydrique du sol sur l'amplitude des canicules. Différents comportements sont observés, en plaine la température dans la couche limite atmosphérique est largement contrôlé par la convection à l'échelle locale. Sur les zones côtières et montagneuses, les circulations de méso-échelle de type vent de pente et brises de mer contribuent à atténuer considérablement la canicule en favorisant l'advection d'air frais et humide et la formation de précipitations.

L'effet de la végétation sur l'amplitude des canicules a par la suite été analysé. Pour ce faire, j'ai développé des outils de modélisation couplant dynamique atmosphérique et dynamique de la végétation qui ont permis de mieux comprendre les processus de conditionnement des canicules et sécheresses en Europe de l'ouest. Ce développement s'inscrivait dans un cadre plus large de mise en place d'un modèle du système climatique régional entrepris à l'Institut Pierre Simon Laplace (IPSL) au sein du projet MORCE-MED. Ce volet de ma thèse est le plus original car peu exploré dans la littérature.

De par ces outils j'ai pu tout d'abord montré qu'inclure une végétation interactive dans un modèle atmosphérique régional permettait de simuler les modifications du cycle phénologique qui contrôle le développement de la végétation et l'évapotranspiration. Appliquée aux canicules de juin et août 2003, j'ai montré que la prise en compte d'une végétation interactive atténuait l'amplitude de la canicule de juin et accentuait celle d'août. Enfin, dans un contexte plus applicatif, j'ai évalué l'effet d'un changement d'usage des sols pouvant permettre d'atténuer les effets de ces canicules sur l'homme. Dans une démarche préliminaire, j'ai remplacé les surfaces anthropisées (essentiellement surfaces agricoles) par des forêts et prairies. Là aussi, les effets constatés ont été plus contrastés qu'anticipées, avec une atténuation de la canicule de juin et une accentuation de la canicule d'août avec une variabilité spatiale forte à méso-échelle.

Chapter 1

Introduction

The investigation of extreme events is a specific field of the climatological science. The classical statiscal approach cannot be used to study events which are defined as being singular and scarce. There is no average extreme event because each event highly varies from one to the other and they have to be studied on a case by case basis. These phenomena are not only characterized by their scarcity but also by the remarkable intensity of one or more meteorological variables. Heat waves, droughts, flash floods and storms are related to surface temperature, precipitation and wind. The combination of a complex hierarchy of processes with highly nonlinear interactions is often responsible for the appearance and persistence of such events. During the 2003 summer the heat waves were generated by a high pressure system, strengthened by a drought and a warm Mediterranean sea surface temperature and possibly teleconnected with tropical latitudes. The Mediterranean Sea is a breeding ground for these combinations due to its configuration and location. The Mediterranean is characterized by a quasi-closed ocean basin and a marked orography on its periphery (Figure 1.1), the climate is highly-contrasted with a meridional gradient of temperature and moisture and is directly under the influence of both mid-latitudes and tropical variability. The north is influenced by the effect of the Atlantic Ocean (*Xoplaki*; *Trigo et al.*, 2004) whereas the southern part is under the influence of the descending branch of the Hadley cell. The Mediterranean physiography is complex, comprising numerous mountainous systems, irregular coastlines and a very heterogeneous land cover. Moreover the sea itself acts as a moisture and heat reservoir which can generate high-impact weather systems such as heavy precipitations. These mesocale features induce specific circulations such as sea-breeze, wind slope and convection (*Simpson*, 1989) which may modify the heat waves mesoscale variability.

Issues

Today the improvement of forecast tools for a warning system enables forecasting heatwave events at one week within the acceptance level of confidence (*Pascal et al.*, 2006; *Matsueda*, 2011), but they are hardly predictable beyond and the ability to predict such high-impact climatic events and their consequences remains low (*Weisheimer et al.*, 2011). Soil moisture is a possible long-term indicator, controlling much longer time-scales. Its dynamic and memory effect can affect surface temperature and precipitation, but underlying processes remain insufficiently understood. A better description, understanding and modelling of the land-atmosphere interaction would improve the predictability at both daily (*Trier et al.*,

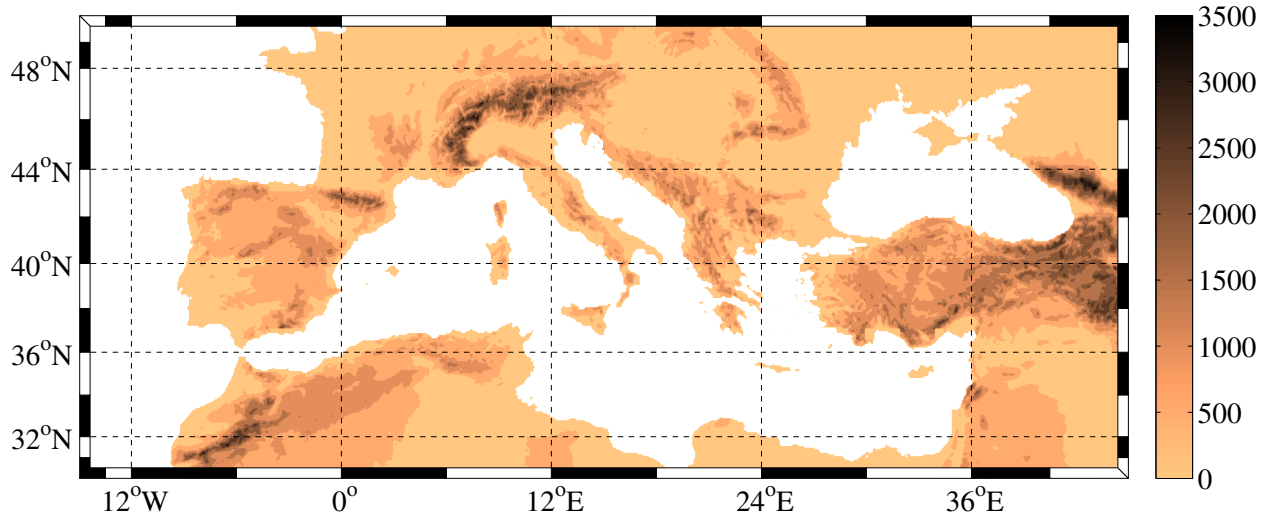

Figure 1.1: Map of the Mediterranean basin. The color shading indicates the height of the topography (m).

2004; *Sutton et al.*, 2006) and subseasonal scale (*Douville and Chauvin*, 2000; *Ferranti and Viterbo*, 2006; *van den Hurk et al.*, 2012). The mesoscale variability of heat waves remain largely unknown within the Mediterranean basin. As the region is affected by specific local coupled processes and feedback loops, a better understanding of land-atmosphere interaction at mesoscale would increase the spatial forecast quality. The characterization of events and their anticipation are important points in reducing the social, economic and environnmental impacts of heat waves through adaptation and mitigation policies.

Heatwaves have very serious social consequences as far as for morbidity, mortality, economy and ecosystems are concerned. Typical examples are the summer of 1995 in Chicago (*Semenza et al.*, 1996), or summers 1976 (*Ellis et al.*, 1980) and 2003 in Europe. This last event in particular was the warmest over the last 500 years over Europe according to (*Luterbacher et al.*, 2004) and in the distant past the only remarkable and comparable event with thousands of victims took place in Beijing in 1749 (*Besancenot*, 2002). The remarkable intensity of the heatwave gave birth to numerous studies that highlighted its consequences on preventive measures and alert systems (*Fouillet et al.*, 2008), air pollution increase (*Vautard et al.*, 2005), the economic and ecological systems, through reduction in the productivity of natural and cultivated vegetation (*Ciais et al.*, 2005; *COPA-COGECA*, 2003), lower energy supply and electricity restriction (*Fink et al.*, 2004).

However we have in mind the overall increased mortality in the European states during the 2003 events which caused 15,000 extra deaths (*Hémon and Jougla*, 2003) in France and 70,000 in 12 European Countries (*WHO*, 2010). In terms of epidemiology the mortality rate increases above an optimum temperature, this threshold varies according to the local context and adaptation of the local populations. Depending upon the city and location, the mortality rate rose by 21 to 31% per degree Celsius on the Iberian Peninsula (*Garcia-Herrera et al.*, 2005). Surveys also show a contrast between rural and urban areas where mortality rises more rapidly with the degree of urbanization. Owing to urban heat island effect, the downtowns (densely built up) have stagnant air and store the heat causing higher temperatures (*Besancenot*, 2002). This is far from being the only reason *Vautard et al.* (2005) highlighted the excep-

tional episodes of air pollution (mainly from ozone and fine particles). The synergy between heat and pollution favors respiratory and cardiac pathologies (*Kovats et al.*, 2004; *Filleul et al.*, 2006), which are among the main death causes during heat waves, along with heat stroke, hyperthermia and dehydration (*Fouillet et al.*, 2006).

Natural ecosystems are also affected by heat waves. Heat can inhibit the protein biosynthesis, degrade enzymes and damage the integrity of cell membranes, causing irreversible effects (*Wahid et al.*, 2007). If high temperatures do not directly cause the destruction of plants, they alter their operating functions. The additionnal effect of heat and drought induces significant water stress which brings long-term consequences on vegetation development (*Gobron et al.*, 2005). Based on FLUXNET observations and modeling studies, *Ciais et al.* (2005) showed that during the summer of 2003 the primary production fell by 33%. The primary production corresponds to the carbon from the atmosphere captured by the plants in order to create their own organic matter, the photosynthesis as a process acts as a sink for atmospheric carbon. The decrease in plant growth transformed the usual CO_2 sink into carbon source. The deficit in CO_2 sequestration was compared to a conventional release of 3 to 5 years of classic sequestrations. As far as viticulture is concerned, drought and heat waves combination have reduced leaf activity, grape feedings and polyphenol synthesis. The 2003 vintage year was early and incomplete except for great vintage and syrupy wines, some of them have produced high quality vintage (*Nau*, 2004).

Natural and anthropogenic systems such as forests and crops have different behavior under heat waves conditions (*Teuling et al.*, 2010). Crops and grasses can evaporate more than trees during heat waves as long as moisture is not limited. On the long term, the conservative water use of trees mitigates drought effect whereas crops collapse. Even if the managed lands can benefit from irrigation to mitigate the heat effects, yields dropped by 15 to 60% for potatoes, cotton or fodder (*COPA-COGECA*, 2003). It resulted in an increase in the cost of basic products like French fries. Economic consequences do not stop there. There are impacts on tourism with a change in attendance countries and sites, a change in tourism pattern and habits. With the drought and precipitation deficit before and during heat waves, many rivers saw their water flow reached their lowest historical level, like the Rhine (1/3 of its usual level) (*Fink et al.*, 2004). Many thermal power plants and nuclear reactors had to cut their energy production, because they were not able to cool down efficiently with water from nearby rivers. In Amsterdam the cost of electricity doubled over the 2003 summer compared to the same period in 2002. The United Nations have estimated that the total economic loss exceeded 13 billion euros (*Warning and Threats*, 2004).

Although such heatwaves are exceptional, several studies have shown that in the context of global warming, associated with an increase in average temperature and variability, these phenomena may become not only more frequent but also longer and more intense (*Easterling et al.*, 2000; *Räisänen*, 2002; *Klein Tank and Konnen*, 2003; *Beniston*, 2004; *Schär et al.*, 2004; *Meehl and Tebaldi*, 2004; *Klein Tank et al.*, 2005; *Della-Marta et al.*, 2007). This is especially true in the Mediterranean, pointed by *Giorgi* (1996) as one of the most sensitive region to climate change, according to an index based on the mean change and interannual variability in precipitation and temperature. The average changes in temperature in the Mediterranean must be distinguished from the variability increase, more pronounced in Central Europe (Fig. 1.2). The change in precipitation could also lead to a change in vegetation cover and soil structure, inducing a trend towards a desertification of the northern Mediterranean, as experienced by the southern and eastern parts of the basin (*Lavee et al.*, 1998).

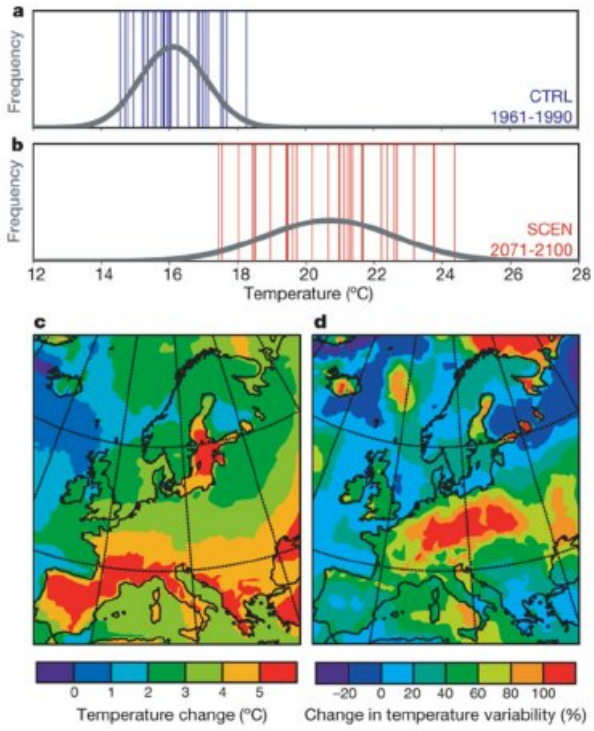

Figure 1.2: Results from an RCM climate change scenario representing current (CTRL 1961–90) and future (SCEN 2071–2100) conditions. a, b, Statistical distribution of summer temperatures at a grid point in northern Switzerland for CTRL and SCEN, respectively. c, Associated temperature change (SCEN–CTRL, °C). d, Change in variability expressed as relative change in standard deviation of JJA means ((SCEN–CTRL)/CTRL, %). (*Schär et al.*, 2004)

Scientific context

The addition of several mechanisms described below - such as atmospheric stability, sea surface temperature anomaly and drought - led to the very exceptional 2003 heat waves with a temperature up by 12.5°C with respect to climatological observations realised between 1971-2000 (*Levinson and Waple*, 2004). Many of these physical mechanisms related to heatwaves have been studied and listed by order of importance. Heat waves are related to specific large-scale circulations of the atmosphere called " weather regimes " (*Yiou and M*, 2004; *Cony et al.*, 2010). The weather regimes rely on atmospherical configurations defined as the most frequent or the most persistent pattern (*Cheng and Wallace*, 1993; *Michelangeli et al.*, 1995; *Plaut and Simmonnet*, 2001). *Cassou et al.* (2005) identified two patterns favoring hot periods and heat waves, they are defined as an atmospheric blocking or — for Europe — as an Atlantic low putting western Europe under persistent southerly wind conditions. The blocking is the positive phase of the North Atlantic Oscillation (NAO) (*Hurrell et al.*, 2003), with an anticyclone centered over Scandinavia and the North Sea. The Atlantic low is characterized by a strong depression covering the North Atlantic while a block extends from the Iberian Peninsula to the Baltic Sea. Inspired by *Colacino and Conte* (1995), *Baldi et al.* (2006) evaluate the position of the westerly jet, divided into main branches over Europe :

Scandinavian and Mediterranean. When the Mediterranean jet moves north of the Alps, they noted that an anticyclonic vorticity appeared over the Mediterranean provoking strong subsidence and adiabatic warming. These atmospheric anomalies are the consequences of synoptic variability, the reason for that shifting from one regime to another are still unknown but they may be generated by large-scale climate forcings.

Cassou et al. (2005); *Cassou* (2008) has investigated the influence of tropical oceans on weather patterns in the North Atlantic. They showed that the Madden-Julian Oscillation (MJO) and anomalous tropical convection partially controlled their distribution. The eastward MJO propagation from the western tropical Pacific initiates a wave train favouring the positive phase of the NAO, the atmospherical configuration for August 2003. *Black and Sutton* (2007) use a mechanism described in *Rodwell and Hoskins* (1996) to explain the teleconnexion with the Indian Ocean. In some cases, the monsoon and anomalous sea surface temperature may create subsidence over the Mediterranean region and therefore inhibit convection. Hence precipitation and cloud cover are reduced on the mainland. *Ogi et al.* (2005) relate the heat waves to the anomalies in the upper air jets and the August 2003 synoptic situation can be viewed as an abnormal positive phase of the summer Northern Annular Mode (NAM). This planetary circulation linked European and Canadian warm temperature with Japanese cold weather. However the blocking alone is not sufficient to explain such a temperature anomaly, others factor play a role as the surface – atmosphere interactions or the Sea Surface Temperature (SST). *Cassou et al.* (2005) suggested that the conjunction of several physical mechanisms led to warmer conditions in Europe.

Feudale and Shukla (2010) suggested that an increase in sea surface temperature in the North Sea, the North Atlantic Ocean and the Mediterranean regions created a barotropic response of the atmosphere that have reduced the meridional gradient of temperature, consistent with a northward shift of the Inter-Tropical Convergence Zone and of the descending branch of the Hadley cell. The subsidence motion over the Mediterranean inhibits the convection, creates a clear sky and enhances the solar radiation. Consequently the warm SST strengthens the atmospherical blocking and heats up the surface. About the atmospherical blocking, with a climatological SST everywhere or in selected regions *Nakamura et al.* (2005) showed that the blocking location is not correctly reproduced, especially without the 2003 SST in the vicinity of the Gulf Stream.

The study of soil-atmosphere coupling is far from being a recent research field (see *Seneviratne et al.* (2010) for an extensive review). Beyond dynamical processes on the planetary and synoptic scales, land-atmosphere feedbacks can significantly modify both local and regional climates. Several process studies have investigated mechanism controlling the linkage between soil moisture, temperature and precipitation. Interactions between land and atmosphere are crucial for a better understanding of the climate variability, in particular for the transitional area between dry and wet climates (*Koster*, 2004), as the Euro-Mediterranean region. They act over a wide range of spatial scales from local to global (*Schär et al.*, 1999; *Pielke*, 2001; *Koster*, 2004; *Betts et al.*, 1996; *Beljaars et al.*, 1996) and also according to different timescales, from seconds to hours through biogeochemical processes, momentum, energy and water exchanges (plus other chemical components such as CO_2).

When heat wave conditions, especially if preceded by drought, the land and atmosphere coupling can amplify the temperature anomaly by increasing the sensible heat flux locally (*Ferranti and Viterbo*, 2006; *Fischer et al.*, 2007a,b). The sensitivity analysis is a classic way to investigate the relationship between two variables. To quantify the relationship between soil moisture and temperature, *Fischer et al.* (2007a)

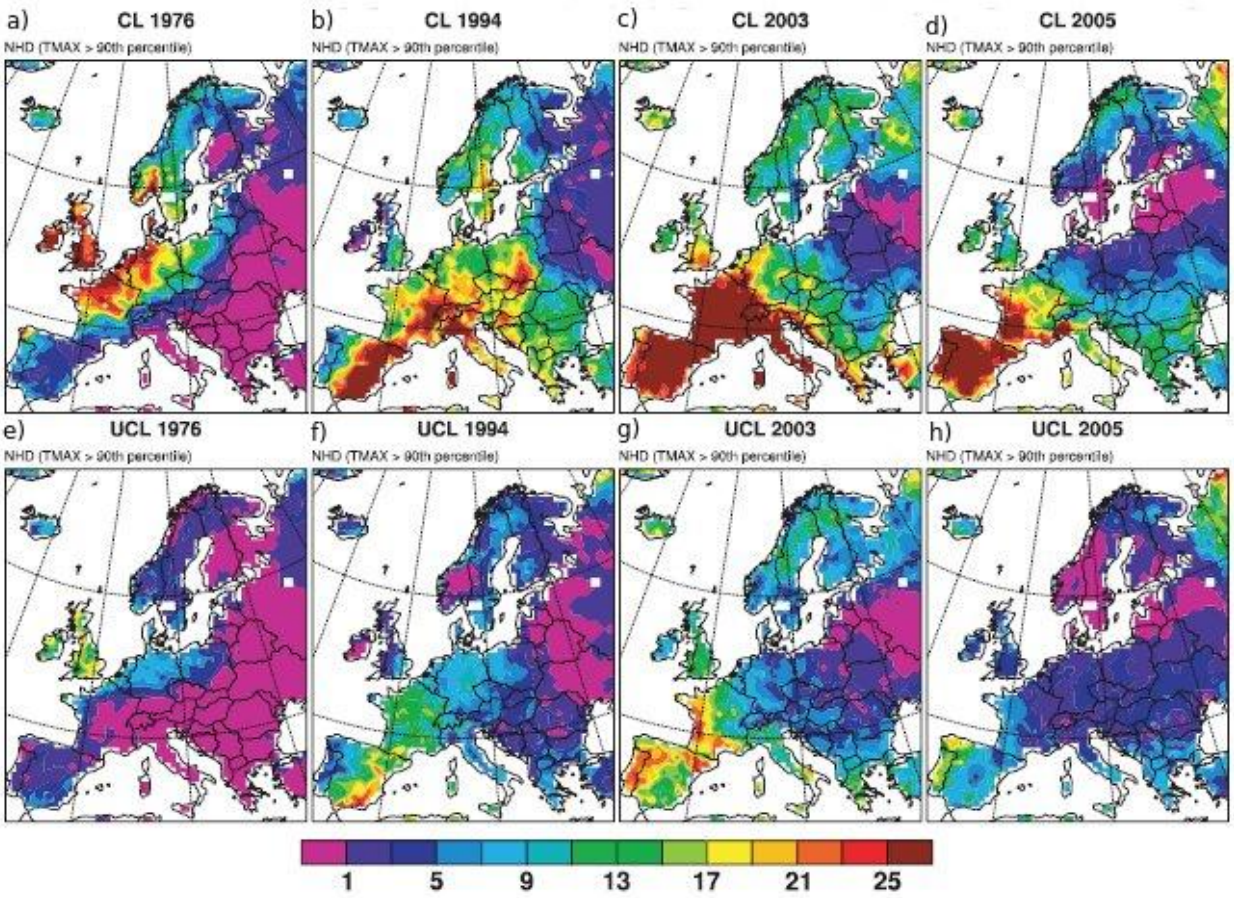

Figure 1.3: Number of hot days (NHD) derived (a–d) the simulations with (CL) and (e–h) without land-atmosphere coupling (UCL) during the summers (JJA) 1976, 1994, 2003, and 2005. NHD is defined as the number of days where the daily maximum temperature exceeds the long-term 90th percentile of local probability function over the 1960-2005 period. (*Fischer et al.*, 2007a)

used two simulations with and without coupling between atmosphere and land surface by prescribing an average seasonal cycle of soil moisture. The coupling alone represents 50 to 80% of the total number of hot days during the four major European heat waves over the past 50 years (1976, 1994, 2003, 2005, see also Fig. 1.3). This surface-atmosphere coupling also increases the temperature anomaly on a seasonal scale and in particular strengthens the temperature during the hot days. In the coupled simulation, the dry soil favors a sensible heat flux increase (at the expense of latent), which enhances the surface temperature. The same simulations are performed by maintaining the coupling but with a disturbing soil moisture. They show that without drought, the summer temperature anomaly is reduced by 40% (*Fischer et al.*, 2007b).

This positive feedback between soil moisture and temperature is based on the conversion of solar radiation into heat at the expense of evapotranspiration, the relations with cloudiness and water vapour are not being taken into account. This assumption is right because heat waves occur under blocking synoptic conditions associated with sunny weather (*Cassou et al.*, 2005; *Fink et al.*, 2004). The underlying soil-moisture precipitation feedback is partly straightforward and intuitive. A rainfall deficit creates a

lack of soil moisture which induces less evapotranspiration and a drier atmosphere with consequently less clouds and precipitation.

Lorenz et al. (2010) also studied the link between drought and heat waves. They showed that soil moisture with constant values or prescribed seasonal cycle, even with dry conditions, tends to shorten persistent heat waves. In contrast soil moisture interactivity increases the persistence of heat waves, by extending their duration of 5 to 10% on average. This illustrates the fact that soil moisture memory plays a key role in the process.

In Europe, the effect of drought can also be non-local (*Vautard et al.*, 2007; *Zampieri et al.*, 2009) with the advection of dry and cloudiness air from the Mediterranean to Northern Europe during spring. *Vautard et al.* (2007) showed that the 10 hottest summers in Western Europe were systematically preceded by winter rainfall deficit conditions in Mediterranean Europe. They proposed the following mechanism. The lack of rainfall creates, drought and dry air mass which spread northward through Europe in early summer, due to atmospheric transport of air during southerly wind episodes. This process was confirmed by *Zampieri et al.* (2009) with numerical modeling, who showed clearly that the signal in the precipitation deficit is consistently linked to higher summer temperatures. However these studies focus on limited geographical areas and predetermined years, restricting the field of investigation. They are based solely on the 2003 event, or they define heatwaves from temperature anomalies averaged over the whole European continent.

Vegetation is an integral part of the land system. Atmosphere and vegetation interactions are based on an enhanced exchange of heat, moisture, trace gases, aerosols, and momentum between the surface and the overlying atmosphere, since the vegetation can use a deep root zone. Both sides perpetually interact and evolve differently. The interaction can modify local, regional, and global climate from seconds to yearly timescale and involved physical changes to land surface (biogeophysical feedback) and changes in the chemical atmospheric composition (biogeochemical feedback) (*Bounoua et al.*, 2000; *Lu and Shuttleworth*, 2002; *Bonan*, 1997). Vegetation distribution itself is determined by temperature range, light and water availability and CO_2 (*Budyko*, 1974; *Nemani et al.*, 2003). The induced albedo change, flux partitionning and CO_2 related effect can affect climate and compensate global change. On a seasonal scale vegetation phenology (leaf onset and fall, vegetation density) is controlled by temperature and precipitation and can in turn affect temperature, surface energy and hydrological budget (*Kaufmann et al.*, 2003). Recent studies have shown that interannual phenologic variations influence hydrological flux variations (*Guillevic et al.*, 2002). On an instantaneaous timescale plant stomata quickly react to short-wave radiation variations induced by cloudiness (*Pielke et al.*, 1990) and the groundwater budget is modified through changes in evapotranspiration, interception loss and percolation. The control on evapotranspiration by stomata is the most important biophysical feature, given that plant transpiration is the main contributor to evapotranspiration (Fig. 1.4). The daytime boundary layer height is strongly dependent on solar radiation partitioning into sensible and latent heat fluxes. Larger sensible heat fluxes create deeper planetary boundary layers with less air moisture.

More research on climate-vegetation interactions was conducted over the 1990 decade, as technological tools, such as new scientific satellites, allowed to assess vegetation cover and provided new inputs for land surface schemes. Some studies have simply changed the foliar surface as prescribed by doubling or by dividing the climatological LAI (*Bounoua et al.*, 2000). They showed that variations in LAI caused proportionate changes in evapotranspiration and carbon sequestration. However the representation of

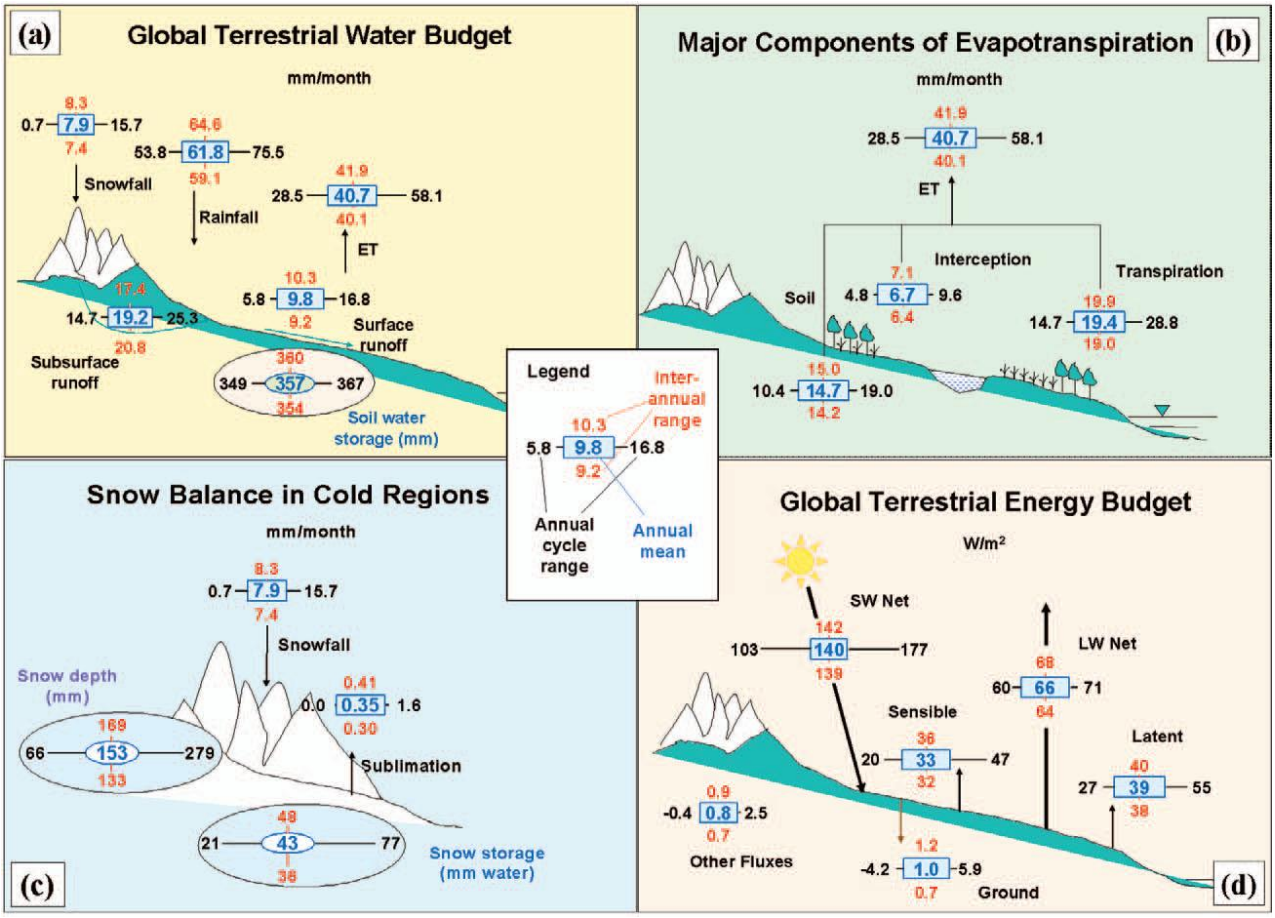

Figure 1.4: Components of (a) the surface hydrologic balance, (b) total evapotranspiration, (c) the surface snow balance, and (d) the surface energy balance. (*Dirmeyer et al.*, 2006)

vegetation in the models involved remained very simplified and was fixed or evolved regardless of climate and water limitation effects. The seasonal evolution of LAI was prescribed, with daily or monthly values without interannual variability.

Recently the use of a dynamic vegetation model, more sophisticated, has made it possible at global (*Foley et al.*, 1998; *Bonan et al.*, 2003) as well as regional scale (*Jung et al.*, 2007; *Vetter et al.*, 2008; *Morales et al.*, 2005; *Santaren et al.*, 2007; *Keenan et al.*, 2009; *Mahecha et al.*, 2010; *Anav et al.*, 2010b) to validate the hydrological cycle and carbon with measuring stations. There are still two limitations, either the horizontal resolution is low (several degrees), or there is no interactive coupling (one-way). Under such conditions it is difficult to study mesoscale phenomena that influence and alter the spatial variability of temperatures during heat waves. The changes in soil moisture have the larger impact on the surface climate on timescales ranging of days to seasons. Exceptionally for a specific year, as in 2003, the effect of drought on tree growth can persist until the following year (*Gobron et al.*, 2005; *Granier et al.*, 2007).

Lu and Shuttleworth (2002) came down to 50 km over Colorado with a regional climate model (RCM). Their sensitivity study showed that the LAI spatial heterogeneity had a greater impact on the regional

water cycle than its seasonal variations, because it induced mesoscale circulations that would trigger moist convection and precipitation. They emphasized the vegetation spatial distribution influence on soil heating and convection in privileged areas (*Pielke*, 2001).

However, in these modelling studies the vegetation/atmosphere feedbacks were not investigated, since this would request a fully coupled numerical model at high resolution. LSMs explicitly consider the role of vegetation in affecting water and energy balance by taking into account its physiological properties, in particular, leaf area index (LAI) and stomatal conductance. These two physiological properties are also the basis of evapotranspiration parameterizations in physically based hydrological models. Although the model needs sophisticated formulation of land surface (*Weisheimer et al.*, 2011) for a correct predictability of heat waves, the most current LSMs and hydrological models do not parameterize vegetation as a dynamic component. The seasonal evolution of LAI is prescribed, and monthly or daily LAI values are kept constant year after year.

The question of vegetation distribution was raised through anthropogenic land cover change (LCC) studies. Scientists imagined several deforestation (afforestation) scenarii in order to anticipate and mitigate the climate change effects. If the global radiative impact of LCC is low compared to the forcings of increased greenhouse gases concentration (*Forster et al.*, 2007), the biogeophysical effect is not negligible on a regional level (*Findell et al.*, 2007; *Pitman*, 2009). *Stohlgren et al.* (1998) studied the sensitivity of regional climate in Colorado to the vegetation distribution. An opposition between current and potential vegetation showed that the averaged large scale impact was low (about 0.1 ° C) but the regional differences were large (5 ° C). A full temperature redistribution was made by establishing breeze circulations between plain and mountainous area, "fed" by the latent heat flux from irrigated land. In a global change context several scenarii dealt with the influence of LCC on climate although the IPCC 5th Assessment Report (AR5) does not take into account LCC. Deforestation is considered over tropical areas, focused mainly in Amazonia, the tropical rainforest is replaced by pasture. On a large scale surface warming results from higher pasture albedo offset by a lower evaporative cooling than in the forest (*Lean and Rowntree*, 1997; *da Rocha et al.*, 2004; *von Randow et al.*, 2004). On a small scale, an heterogeneous use of the land brings about mesoscale circulation and the enhancement of cumuli over deforested areas (*Chagnon et al.*, 2004). In Australia, along the bunny proof fence (separating native vegetation from agriculture), enhanced latent heat fluxes and cloudiness are observed on native vegetation in summer and conversely in winter (*Ray et al.*, 2003). Boreal forest expansion tends to warm surface through a snow masking effect, forest albedo being by far inferior to snow albedo (*Chalita and Treut*, 1994; *Snyder et al.*, 2004; *Meissner et al.*, 2003). However few studies investigated the land cover change influence on midlatitude climate and in extreme-event prospect (*Pielke et al.*, 2011). In the Mediterranean, studies tend to concur that LCC has a significant impact on regional climate, especially on the extreme-events (*Anav et al.*, 2010a), but the results are sometimes contradictory. According to *Gaertner et al.* (2001) deforestation causes a decrease in evapotranspiration and non local response for decreasing precipitation. Reduced evapotranspiration and increased sensible heat flux during summer is also observed by*Anav et al.* (2010a) but with an afforestation experiment. *Heck et al.* (2001) suggested that an afforested Mediterranean could result in a moister and cooler climate from April to mid-July, until the evapotranspiration is inhibited because the soil moisture reached a critical value. This highlights that results in the Mediterranean remain unclear because they are strongly dependent on the specificities of the land surface model and parameterization.

Process research and investigation during heat waves have sometimes been grounded on data from

global general circulation models (GCMs), which cannot apply to small scales less than 100 km. Such models do not provide information on the spatial structure of geophysical variables and do not give a full account of the high variability regarding the distribution of land use. It is all the more true for the areas of complex topography (e.g. the Alps, the Mediterranean coastlines...) where local and stationary forcings affect processes at high frequency temporal scales (e.g. precipitation frequency and intensity, surface wind variability). *Pielke and Avissar* (1990) showed that the landscape structure, including the spatial distribution of vegetation and soils, can influence the cloudiness and associated rainfall. Moreover the representation of regional and local atmospheric circulations (e.g. anabatic/katabatic cross valley winds, mesoscale convective systems, sea-breeze and inland breeze) are likewise insufficient. High-resolution data are better suited to study the impact of heat waves; they depict higher land–sea contrast and orographic effects. A high spatial resolution is combined with a high temporal resolution, which should improve the handling of the physical and dynamical processes leading to extreme events. The coupled processes are extremely sensitive to land use heterogeneity, orography and mesocale circulation and may introduce substantial modifications on temperature and precipitation through land-atmosphere feedbacks.

Thesis motivation

Heat waves over the Mediterreanean are triggered by high pressure area, favored by external large-scale forcings from the tropical Atlantic and Indian. The Mediterranean SST may strengthen high pressures whereas subsidence reduces evaporation, cloudiness and increases the temperatures. Until now the heat waves predictability from spring drought has been very limited. Few studies were performed and they were restricted to geographical reduced areas and specific cases. A deficit in soil moisture plays a crucial role by amplifying, maintaining and preconditioning heat waves; but there have been few studies conducted on the influence of local processes and circulations on a mesoscale during these events.

Vegetation is located on the land-atmosphere interface and is the main contributor to total evapotranspiration. Heat waves modelling becomes more complex when considering vegetation because of highly non-linear plants behaviour and spatial variability of different ecosystems. Phenology and vegetation distribution can specifically modify the hydrological cycle on a seasonal and decadal scale respectively. Nevertheless in regional climate models the vegetation representation is so far very simplified. For instance the leaf area index is prescribed or monthly parameterized. The fundamental process of carbon allocation, leaf out and senescence are not represented. The most important point is that the regional climate model solely takes into account one-way interactions, from vegetation to atmosphere, and not two-way interactions with atmosphere feedbacks to vegetation. Recent studies also investigated the impact of anthropogenic land cover change scenarii on climate changes in relation to those induced by the global warming, but they exhibit contradictory effects over the Mediterranean and do not converge towards robust results.

Thesis organisation

This is the climatic context that forms my thesis about the heat waves and land atmosphere interactions. My thesis consists in highlighting and understanding the functioning of coupled process between soil, vegetation and atmosphere at mesoscale during the heat waves. The chapter 2 introduces my contribution

to a numerical plateform dedicated to the improvement of regional coupled models. To achieve, this I realized the coupling of a non-hydrostatic model with a dynamical global vegetation model so as to adress land-atmosphere interactions when vegetation is better depicted and fully interactive. In chapter 3, I deepen the influence of heat waves preconditioning and conditioning by a negative soil moisture anomalies on the Euro-Mediterranean region. For this I developed different methodologies to produce a heat waves climatology and classification according to their spatial pattern. I intented to regionaly refine the presence or absence of preconditioning. Then a modeling study of heat waves on mesoscale between 1989 and 2008 was set up, by means of which I have been exploring the influence of soil moisture depletion on temperature, mesoscale circulations and processes.

The current RCM includes increasingly sophisticated LSM, nonetheless they do not take into account the coupled process between vegetation, soil and atmosphere. In the chapter 4, the effect of two-way interaction between vegetation and atmosphere on the climate and heat wave variability is studied. I use the coupled model developed in chapter 2 to demonstrate that accounting for an interactive phenology is non negligible in the temporal and spatial modulation of heat waves. Here we have analyzed the two events following the heat wave that hit Europe in the summer of 2003. Then the influence of anthropogenic land cover change is investigated for the same heat waves and with the same coupled model. Two simulations with exchanged surface properties by switching the land cover from crop to wood have been performed. I have assessed their ability to mitigate the impacts of heat waves. Finally conclusions and summaries are given in chapter 5.

Chapter 2

Simulations of heat waves

This chapter details the different numerical models and simulations that have been developed during this thesis. All simulations is use the WRF model (Weather Research and Forecast), but some are coupled with land surface models distributed with WRF and some are coupled with the IPSL land surface model ORCHIDEE. This latter version has been developed in the frame of this thesis and as part of the development of the MORCE platform. The MORCE platform is detailed in section 2.2, synthesis of the article *Drobinski et al.* (2012).

2.1 Simulations with the distributed version of WRF

The atmospheric model is based on the dynamical core of the numerical model WRF (version 3.1.1). The WRF model is developed by the National Center for Atmospheric Research (NCAR) (*Skamarock et al.*, 2008). The WRF model system also offers multiple options for various physical packages.

Two simulations have been run with WRF in order to investigate the effect of soil moisture depletion on heat waves in chapter 3. They have been performed in the context of the World Climate Research Program (WCRP) endorsed programs MED-CORDEX and HyMeX (*Drobinski et al.*, 2009, 2010).

The main objectives of CORDEX are to provide climatic data disaggregated across the recent past and projections for 21st century, make available relevant climate information over regions worldwide for input to groups conducting impact/adaptation assessments and to the IPCC 5th Assessment Report (AR5). The MED-CORDEX initiative is a coordinated contribution from the Mediterranean climate research community of HyMeX to CORDEX. HyMeX (HYdrological cycle in the Mediterranean EXperiment) aims at a better understanding and quantification of the hydrological cycle and related processes in the Mediterranean, with emphasis on high-impact weather events, by monitoring and modelling the Mediterranean atmosphere-land-ocean coupled system, its variability from the event to the seasonal and interannual scales, and its characteristics over one decade (2010-2020) in the context of global change

2.1.1 The atmospheric component

The atmospheric module of WRF solves the fully compressible euler and non-hydrostatic equations of motion including the full Coriolis terms, but a run-time hydrostatic option is available. The equations are formulated using a terrain-following σ coordinates. The coordinate are denoted by η and defined as :

$\eta = (P_h - P_{ht})/\mu$ where $\mu = p_{hs} - p_{ht}$

p_h is the hydrostatic component of the pressure, and p_{hs} and p_{ht} refer to its values at the surface and at the top domain respectively. η varies from 1 at the surface to 0 at the upper limit of the model domain. μ represents the mass per unit area within a column in the domain, the corresponding flux form variable are

$V = \mu v = (U, V, W), \quad \Omega = \mu\dot{\eta}, \quad \Theta = \mu\theta$

$v = (u, v, w)$ are the covariant velocities of horizontal and vertical directions respectively, while $\omega = \dot{\eta}$ is the contravariant vertical velovity and θ is the potential temperature.

In the governing equations (flux-form Euler equations) the geopotential ($\phi = gz$), pressure (p) and inverse density ($\alpha = 1/\rho$) are non conserved. The prognostics variables are the velocity components u and v in cartesian coordinate, vertical velocity w, perturbation potential temperature, perturbation geopotential, and perturbation surface pressure of dry air. Optionally, turbulent kinetic energy and any number of scalars such as water vapor mixing ratio, rain/snow mixing ratio, cloud water/ice mixing ratio, and chemical species and tracers. The flux-form Euler equations can be written as :

$$\begin{aligned}
\partial_t U + (\nabla \cdot Vu) - \partial_x(p\partial_\eta\phi) + \partial_\eta(p\partial_x\phi) &= F_U \\
\partial_t V + (\nabla \cdot Vv) - \partial_y(p\partial_\eta\phi) + \partial_\eta(p\partial_y\phi) &= F_V \\
\partial_t W + (\nabla \cdot Vw) - g(\partial_\eta p - \mu) &= F_W \\
\partial_t \Theta + (\nabla \cdot V\theta) &= F_\Theta \\
\partial_t \mu + (\nabla \cdot V) &= 0 \\
\partial_t \phi + \mu^{-1}\left[(\nabla \cdot V\phi) - gW\right] &= 0
\end{aligned}$$

along with the diagnostic relation for the inverse density

$$\partial_\eta \phi = -\alpha\mu$$

and the equation of state

$$p = p_0 \left(R_d\theta/p_0\alpha\right)^\gamma$$

and

$$\begin{aligned}
\nabla \cdot Va &= \partial\left(Ua\right) + \partial_y\left(Va\right) + \partial_\eta\left(\Omega a\right) \\
Va \cdot \nabla &= U\partial_x a + V\partial_y a + \Omega\partial_\eta a
\end{aligned}$$

where a is a generic variable, $\gamma = c_p/c_v = 1.4$ is the ratio of heat capacities for dry air, R_D is the gas constant for dry air, and p_0 is the reference pressure. F_U, F_V, F_W and F_Θ represent forcing terms arising from model physics, turbulent mixing, spherical projections and Earth's rotation.

Variables of the prognostic equations are transformed onto perturbation variables, sum of a reference state with their pertubation. It aims to reduce the computional errors coming from roundings and truncation in the pressure gradient and buoyancy calculations. The reference state corresponds to a function of height for an atmosphere at rest. The perturbation state is defined from a hydrostatically-balanced reference state.

The model use a time-split integration scheme. The equations can be split into a low and high frequency modes, meteorologically speaking. The slow frequency is computing using a third order Runge

Kutta integration scheme during which the physics is integrated. The high-frequency acoustic modes are integrated over smaller time steps to maintain the numerical stability with a forward–backward scheme.

The horizontal grid is a Arakawa C-grid staggering. The normal velocities are staggered one-half grid length (edges of the cell) from the thermodynamic variables (center of the cell). The C grid was superior in simulating the high frequency inertia-gravity wave, but it was less suited in simulating the low frequency processes and computing the Coriolis term (*Arakawa and Lamb*, 1977; *Adcroft et al.*, 1999).

A complete set of physics parametrizations is available, including several land surface models, and several sensitivity studies have been performed to quantify uncertainties in regional climate modeling (e.g. *Flaounas et al.*, 2010; *Crétat et al.*, 2012).

2.1.2 The land surface models

In an atmospheric model, the lower boundary conditions are provided by the land surface model (LSM). The role of the LSM is to compute heat and moisture flux over land but also roughness length or leaf area index and others canopy properties. Therefore it determines the partitionning between latent and sensible heat flux, of high importance for extreme events.

WRF uses several LSM with various degrees of sophistication, the thermal diffusion scheme (slab scheme, *Skamarock et al.*, 2008; *Eckel*, 2002), the rapid update cycle model LSM (RUC, *Smirnova et al.*, 1997, 2000), Noah LSM (*Chen and Dudhia*, 2001), Pleim-Xiu LSM (*Pleim and Xiu*, 1995, 2003). Basically a LSM solves the soil temperature and soil moisture profile, but the complexity relies on the additionnal processes and details taken into account. Explicit snow cover, root zone, LAI evolution, dynamical vegetation, or even irrigation (*De Rosnay et al.*, 2003) can be used by the most recent LSM. Hereafter we will detail only the LSM used in the thesis (SLab and RUC).

The first one is the SLab scheme, based on the MM5 soil temperature model and with a quite simple functionning. Soil temperature and heat transfert is calculated from the differential form of Fourier's Law on 5 layers, where heat flux is linearly proportionnal to temperature gradient. Soil moisture is constant per gridpoint and is land use and season dependant. These moisture values are supposed to fit to the climatological mean but cannot, but cannot represent without a significant error a particular situation. The beginning of the simulation determines the season (summer or winter) and the associated values of moisture availability. In our case, as experiment starts the 1 January 1989 and the soil moisture take winter values. Evapotranspiration is proportionnal to this moisture availibity value according to a bulk formulation from Monin-Obukhov similarity theory.

The RUC LSM comes from a numerical weather prediction and a real time 3h data assimilation used at the North Oceanic and Atmospheric Administration NOAA, operationnal version from the Mesoscale analysis and prediction system (MAPS,*Bleck and Benjamin*, 1993). It solves the vertical diffusive equation of heat and the hydrology of the soil layer is determined by Richard's equation (1931) on six layers with bottom level at 3m. It consists of diffusion, conduction, runoff, evapotranspiration and precipitation. Undergound water transport processes are defined as implemented by *Philip and de Vries* (1957).

$$\frac{\partial \eta}{\partial t} = \frac{\partial}{\partial z}\left(D_\eta \frac{\partial \eta}{\partial z}\right) + \frac{\partial K_\eta}{\partial z}$$

where respectively Dη and K$_\eta$ are diffusionnal and hydraulic conductivity. The evapotranspiration has three components. Direct evaporation from bare ground, evaporation of interception loss from canopy and

vegetation transpiration, involving water from root zone. Transpiration is formulated by *Mahrt and Pan* (1984) and is proportional to the potential evaporation and transpiration rate function, the ratio between available soil moisture content to the available moisture content at field capacity. Root distribution is supposed uniform and constant in the vertical and there is no horizontal water motion.

2.2 Simulations with the MORCE numerical platform

The current WRF land surface models have a non sophisticated vegetation to simulate two-way interactions with the vegetation. To deal with that issue, we couple WRF with the ORCHIDEE model. ORCHIDEE is dynamical vegetation model which computes the hydrological and energy budget as a classical land surface scheme but additionnaly takes into account the vegetation dynamics and leaf phenology. Further details concerning ORCHIDEE are presented in section 2.2.1. This coupling has been carried out in the framework of the MORCE project (section 2.2.2) and technical details about the coupling are given in section 2.2.3. Two sets of simulation are performed in order to analyse the effect on the 2003 heat waves of an interactive phenology and an anthropogenic land cover change (chapter 4).

2.2.1 The dynamical vegetation surface model ORCHIDEE

The LSMs have the primary purpose to provide in atmospheric models the boundary conditions and water and energy fluxes from the soil. To this end, the LSM solves an hydrologic and energy budget, coupled through the latent heat and albedo computation, both depending on soil moisture content. The land-surface model ORCHIDEE (ORganizing Carbon and Hydrology In Dynamic EcosystEms) developed at IPSL and Laboratoire de Glaciologie et Géophysique de l'Environnement (LGGE) is an LSM coupled to a biogeochemistry and a dynamic biogeography model (*Krinner et al.*, 2005). ORCHIDEE simulates the fast feedback occurring between the vegetated land surface and the atmosphere, the terrestrial carbon cycle, and also changes in vegetation composition and distribution in response to climate change. ORCHIDEE is based on three different modules operating at increasing timescales (*Krinner et al.*, 2005).

1. The first module, called SECHIBA (Schématisation des EChanges Hydriques à l'Interface entre la Biosphère et l'Atmosphère, *Ducoudré et al.*, 1993; *Viovy and de Noblet-Ducoudré*, 1997; *De Rosnay and Polcher*, 1998), describes the fast processes such as exchanges of energy and water between the atmosphere and the biosphere, and the soil water budget. Its time step is that of the amospheric model. SECHIBA also includes a routing module which transports thewater which is not infiltrated or drains at the bottom of the soil through rivers and aquifers (*d'Orgeval et al.*, 2008). This module runs at the spatial resolution of ORCHIDEE but represents more than one basin per grid box. The time step is larger than the one of SECHIBA and depends on the horizontal resolution. The tight integration of the routing within SECHIBA allows to re-evaporate the water on its way to the ocean through processes such as floodplains or irrigation (*De Rosnay et al.*, 2003).

2. The phenology and carbon dynamics of the terrestrial biosphere are simulated by the STOMATE (Saclay Toulouse Orsay Model for the Analysis of Terrestrial Ecosystems) model (*Krinner et al.*, 2005). STOMATE simulates, with a daily time step, processes as photosynthesis, carbon allocation, litter decomposition, soil carbon dynamics, maintenance and growth respiration, and phenology.

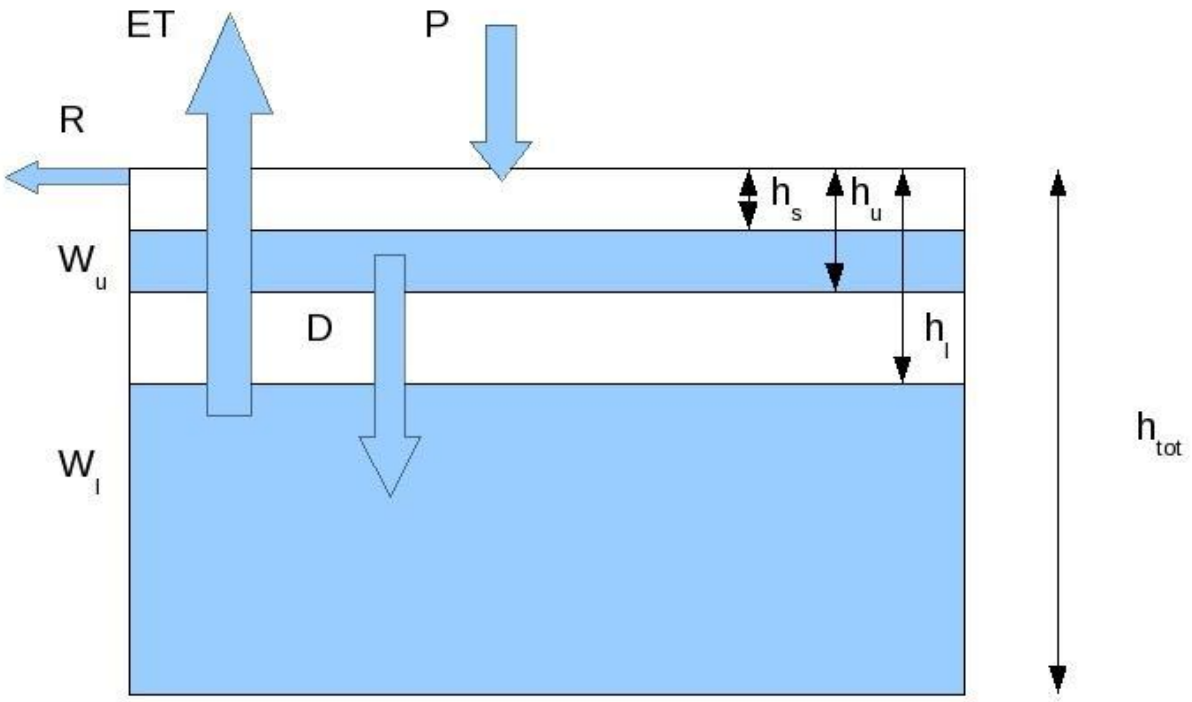

Figure 2.1: Soil discretization in Choisnel model

3. Finally, the long-term processes (yearly time step) include vegetation dynamics, fire, sapling establishment, light competition, and tree mortality are simulated according to the global vegetation model LPJ (Lund-Postdam-Jena) (*Sitch et al.*, 2003).

Hydrologic budget

Hydrology in SECHIBA (*Ducoudré et al.*, 1993; *De Rosnay and Polcher*, 1998) rely on two schemes, Choisnel (*Choisnel et al.*, 1995) and CWRR. Hereafter, only the Choisnel's scheme is detailed since it is the configuration used for the thesis. In the Choisnel's scheme, soil is composed of two layers of variable depths, a superficial and a lower one. The total depth (h_{tot}) is two meters, constant at all land points. Storage capacity (i.e., r_{max} the difference between field capacity and wilting point) is prescribed to 150 mm m^{-3}. The soil in SECHIBA is schematized in

Soil moisture in upper layer (W_u) is most reactive than soil moisture in lower layer (W_l). W_U is determined by moisture convergence :

$$\frac{\partial W_u}{\partial t} = P - ET - D$$

where D is the drainage between the two layers, ET the soil water loss through evapotranspiration from soil and plants and P the total precipitation reaching the soil (snow and rain). Precipitations reach

the soil after filling the interception pool. Interception pool is regularly updated by substracting its evaporation. The lower reservoir is obviously supplied only by drainage.

Nevertheless the model is more complex than a bucket since its depth varies in time. If rainfall occur, soil is filled from top to bottom and when evapotranspiration exceeds rainfall, water is removed from the upper level where it is available. The runoff (R) occurs when both W_u and W_l are saturated, in this case the upper reservoir is removed.

The depth of the upper reservoir (h_u) varies according to two cases. In the first one, the saturation is not reached in the upper reservoir and the depth is reduced by drainage.

$$\frac{\partial h_u}{\partial t} = \frac{-D}{r_{max}}$$

In the second case, the upper reservoir is saturated and its depth increases in case of moisture convergence ($P - ET > 0$).

$$\frac{\partial h_u}{\partial t} = \frac{P - ET - D}{r_{max}}$$

The upper reservoir is created as soon as precipitation is larger than evaporation, while the deep reservoir acts as a bucket when there is no upper reservoir.

The hydrological balance is computed for each plant functional types (PFT), and the various water reservoirs are independent horizontally. Control of evapotranspiration by plants is proportional to soil water stress β and is done through a water uptake function U_s. A wilting point is defined by $W_{wilt} = 5kg\,m^{-3}$, if $W_u + W_l < W_{wilt}$ so $U_s = 0$. Otherwise U_s is related to the exponential structure of the root system and vertical soil moisture profile, and represents the root ability to extract water from the soil at a given humidity. The root density profile can be characterized as follows :

$$R(z) = e^{-cz}$$

where c is the constant dependant from the PFT.

The calculation of U_s for a layer l is :

$$U_s = \frac{\int_0^\infty \beta(E(z - h_{ld})r_{max})R(z)dz}{\int_0^\infty \beta(r_{max})R(z)dz}$$

where z is the vertical coordinate, distance from the top, positive downward. $h_{ld}$is the dry soil height, height below which soil is at saturation and above which soil is dry. $E(z)$ is the Heaviside step function. The integration is performed from the top to a bottomless soil column in order to include the full root system and be independent of the soil depth.

The soil water stres coefficient β varies between 0 and 1, consequently the water uptake function U_s varies within the same range. High stress is thus synonymous with low value and dry soil, while high values close to 1 indicate a low water stress with a saturated soil and a maximum of evapotranspiration. The Choisnel scheme has several advantages. First it is straightforward and thus limits expensive computational cost, but is more sophisticated than a bucket model. The upper layer allows an evaporation very reactive with regards to a rainfall event. Water ground movements are not realistic but are parameterized in order to provide sufficiently relevant response from the model in terms of fluxes.

Energy budget

The energy balance determines the repartition between heat storage $c_s \delta T_s$ (temperature variation), $LW\uparrow$ outgoing infrared radiation, λE latent heat flux, SH sensible heat flux and ground heat flux$G$, from $SW\downarrow$ and $LW\downarrow$ the visible radiation and near-infrared received by the surface respectively. The visible and near-infrared radiation are weighted by the visible albedo α_{sw} (wavelengths below 0.7µm) and near infrared α_{lw} (wavelengths above 0.7 µm). Constant albedo values are prescribed for each PFT's leaves and for bare soil, while the total albedo depends on soil color and moisture (*Wilson and Henderson-Sellers*, 1985), PFT type and LAI.

The land energy balance for the upper surface layer in ORCHIDEE can be expressed as :

$$(1-\alpha_{sw})\,SW\downarrow +(1-\alpha_{lw})\epsilon LW\downarrow -\epsilon LW\uparrow -\lambda ET - SH - G = c_s \delta T_s$$

whereλ is the latent heat of vaporization, ϵ the surface emissivity, c_s the calorific capacity of the soil layer and T_s the surface temperature.

The outgoing infrared radiation ($LW\uparrow$) is computed according to the Stefan-Boltzmann law which states that the total energy radiated by a black body :

$$LW\uparrow = \sigma T_s^4$$

The ground heat flux G is calculated fromto the differential form of Fourier's Law of thermal conduction along the vertical. No horizontal diffusion is allowed, phase changes and ground water movements are not taken into account.

$$\begin{aligned} G &= \kappa \frac{\partial T}{\partial z} \\ \frac{\partial T}{\partial t} &= \frac{\kappa}{C} \cdot \frac{\partial^2 T}{\partial z^2} \end{aligned}$$

where κ is the material's thermal conductivity and C is the specific heat capacity.

Concerning the soil temperature computation seven layers are used, independently from the two layers used in hydrology. The boundary condition in the bottom is a null flux. These layers have constant depth so that the first and last layer have a characteristic time of 30 minutes and two hours respectively.

The turbulent heat fluxes are modulated by the aerodynamic resistance (R_a) :

$$R_a = \frac{1}{C_d U}$$

where C_d is the drag coefficient and U is the windspeed.

SH the sensible heat flux is calculated from the Fick's first law :

$$SH = \frac{\rho}{r_a} c_p \left(T_s - T_a\right)$$

where ρ is the air density, c_p the air calorific capacity and T_a the near surface temperature.

λE latent heat flux is the sum, per grid cell, of snow sublimation, soil evaporation and canopy evapotranspiration (ETP). All those fluxes depend on series of resistances (aerodynamic, canopy, architectural and soil resistances). Stomatal conductance is evaluated by an empirical function that is proportional to the product of photosynthesis and atmospheric relative humidity and is inversely related to CO_2 concentration at the leaf surface (*Ball*, 1987; *Collatz et al.*, 1991; *Farquhar et al.*, 1980).

PFT	climate	foliage	type	LAI_{max}	c	α_{sw}	α_{lw}	h	r_k	k_0
TrBE	Tropical	Broadleaf	Evergreen	8	0.8	0.04	0.2	30	25	12.10^{-5}
TrBR	Tropical	Broadleaf	Raingreen	8	0.8	0.06	0.22	30	25	12.10^{-5}
TeNE	Temperate	Needleleaf	Evergreen	4	1	0.06	0.22	20	25	12.10^{-5}
TeBE	Temperate	Broadleaf	Evergreen	4.5	0.8	0.06	0.22	20	25	12.10^{-5}
TeBS	Temperate	Broadleaf	Summergreen	4.5	0.8	0.06	0.22	20	25	25.10^{-5}
BoNE	Boreal	Needleleaf	Evergreen	4	1	0.06	0.22	15	25	12.10^{-5}
BoBS	Boreal	Broadleaf	Summergreen	4.5	1	0.06	0.22	15	25	25.10^{-5}
BoNS	Boreal	Needleleaf	Summergreen	4	0.8	0.06	0.22	15	25	25.10^{-5}
NC3	-	C3	Grassland	2.5	4	0.1	0.3	0.5	2.5	30.10^{-5}
NC4	-	C4	Grassland	2.5	4	0.1	0.3	0.6	2	30.10^{-5}
AC3	-	C3	Crop	6	4	0.1	0.3	1	2	30.10^{-5}
AC4	-	C4	Crop	3	4	0.1	0.3	1	2	30.10^{-5}

Table 2.1: Plant functionnal type in ORCHIDEE and their main features. $LAI_{max}$is the maximum LAI beyond which there is no allocation of biomasse to leaves. c is the root profile coefficient (m^{-1}). α_{sw} and α_{lw} respectively are the visible and infrared albedo. h is the prescribed height (m). r_k is the structural resistance ($s\,m^{-1}$).k_0 is a constant used for ther stomatic resistance computation.

The vegetation evapotranspiration for a PFTk is calculated as follows :

$$ET = (1 - I) \times \frac{1}{1 + \frac{r_k + r_k^v}{r_a}} U_s \times \frac{\rho}{r_a} \left(q_s\left(T_s\right) - q_a\right)$$

where I is the foliar surface with intercepted water, r_k the structural resistance given in table 2.1, r_k^v the stomatic resistance, U_s the water uptake function described above with the hydrologic budget, $q_s\left(T_s\right)$ the saturation mixing ratio at ground surface temperature and $q_a$the mixing ratio at a reference height. According to *Ball* (1987) parameterization, the stomatal conductance (g_{sto}) has a simple linear relation with the CO_2 concentration (C_s) and the relative humidity (h_s) at the leaf surface, and indirectly dependents on temperature and radiation via the net photosynthesis (A_n).

$$g_{sto} = g_0 + \frac{kA_n h_s}{C_s}$$

The quantity g_0 is the residual stomatal conductance when A_n approaches zero, k is the slope of the relationship between g_{sto} and the Ball index $\frac{A_n h_s}{C_s}$. Albedo and surface roughness are calculated, per grid cell, as a linear combination of PFT and bare soil. Surface roughness depends on tree height and LAI.

Vegetation type

In the ORCHIDEE model, the land surface is described as a mosaic of twelve plant functional types (PFTs) and bare soil. The definition of PFT is based on ecological parameters such as plant physiognomy (tree or grass), leaves (needleleaf or broadleaf), phenology (evergreen, summergreen or raingreen) and photosynthesis type for crops and grasses (C3 or C4) (see tables 2.1 and 2.2 for further details). Relevant biophysical and biogeochemical parameters are prescribed for each PFT (*Krinner et al.*, 2005).

The PFT distribution can be either prescribed from an input inventory (static mode, LPJ deactivated), or entirely simulated by the model depending on climate conditions (dynamic mode, LPJ activated). The fraction of grid space covered by agricultural croplands is always prescribed, so that crop extent is not affected by dynamic vegetation change. The vegetation map is based on a 5 km$\times$ 5 km map derived from

PFT	T_{opt}	T_s	H_s	A_c	$V_{cmax,opt}$
TrBE	37	-	-	730	65
TrBR	37	-	0.6	180	65
TeNE	25	-	-	9130	35
TeBE	32	-	-	730	40
TeBS	26	12	-	180	55
BoNE	25	-	-	910	35
BoBS	25	7	-	180	45
BoNS	25	2	-	180	35
NC3	$27.25 + 0.25\ T_l + 0.025T_l^2$	$-1.375 + 0.1T_l + 0.00375T_l^2$	0.2	120	70
NC4	36	5	0.2	120	70
AC3	30	5	0.3	90	70
AC4	36	10	0.2	90	70

Table 2.2: Plant functionnal type in ORCHIDEE with their senescence and productivity features. T_{opt} Optimum photosynthetic temperature (°C), function of multiannual year T_l for grasses C_3. T_s is the weekly temperature below which the leaves are shed if seasonnal trend is negative. H_s is the weekly moisture stress below which the leaves are shed. A_c critical leaf age for senescence (days). $V_{cmax,opt}$ is the optimal maximum rubisco-limited potential photosynthetic capacity ($\mu mol.m.s$).

the IGBP[1] map with Olson classification (*Loveland et al.*, 2000) and projected onto ORCHIDEE's 12 plant functional types plus desert. Plant assimilation in ORCHIDEE model is based on Farquhar model *Farquhar et al.* (1980) for C3 plants and *Collatz et al.* (1991) for C4 plants. Maintenance respiration is a function of each living biomass pool and temperature, while growth respiration is computed as a fraction of the difference between assimilation inputs and maintenance respiration outputs to plant biomass.

2.2.2 The MORCE project

The objectif for the development of regional Earth system models such the MORCE platform are twofold. First improve the modelling capabilities and our understanding of coupled processes on a regional scale. Secondly support stakeholders who aim to use climate information for regionally-specific impact assessment and adaptation planning. For this purpose the MORCE platform has the following original features :

1. integrating a large number of compartments and coupled processes (physical and biogeochemical processes in the ocean, atmosphere and on the continent),
2. using of a non-hydrostatic atmospheric dynamics allowing simulations to kilometer-scale for which the non-hydrostatic assumption does not stand,
3. a two-way grid nesting capability of both the atmospheric and oceanic components which allows very high resolution of the coupled system in a model subdomain.
4. the platform portability in different regions.

Initially the MORCE-MED project aimed to develop a platform for regional modeling, centered on the Mediterranean. It was afterwards extended to the Indian Ocean, but can be transposed to any

[1] International Geosphere-Biosphere Programm

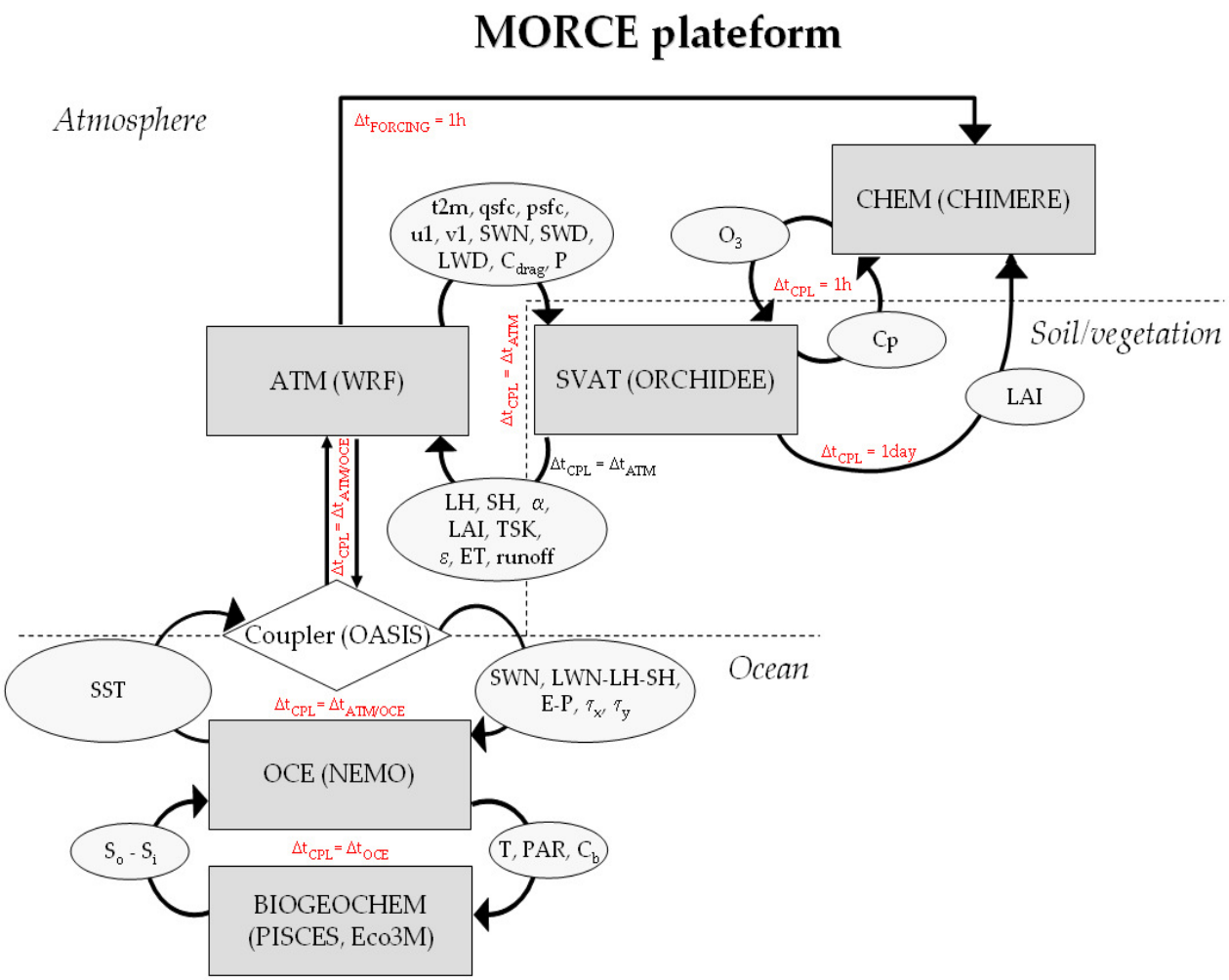

Figure 2.2: MORCE platform flow chart.

desired geographical region on Earth. It is based on the coupling of already-developed regional models of the different compartments of the Earth system (ocean, land surface, atmospheric composition) and interfacing with global models of IPSL. The MORCE platform is detailed in Fig. 2.2.

The MORCE modeling platform is divided into 5 modules dedicated to :

1. atmosphere (ATM)
2. hydrology and vegetation (LSM)
3. ocean (OCE)
4. atmospheric chemistry (CHEM)
5. marine biogeochemistry (BIOGEOCHEM)

The ATM and LSM module are WRF and ORCHIDEE have already been described in subsection 2.1 and 2.1.2). The coupling is detailed in the next section. The ocean model is the NEMO (Nucleus for

European Modelling of the Ocean) system of IPSL, a numerical code for calculating ocean circulation and sea ice. Vertical stretched z-levels are used, except for the bottom layer for which a partial-cell parameterization is used, allowing the last free level of the model to fit the bathymetry. A filtered free surface is used. The solar heat flux can penetrate the ocean surface layer.

CHIMERE is the chemistry module co-developped by IPSL and INERIS. This a chemistry transport modele is driven by meteorological variables and calculates the concentrations of 44 gas-phase and aerosol species for daily forecasts or long term simulations for emission control scenarii. CHIMERE runs over many regions and a range of spatial scales from the regional scale (several thousand kilometers) to the urban scale (100-200 Km) with resolutions from 1-2 km to 100 km.

The marine biogeochemistry module is compounded of PISCES and Eco3M, developed at LPO and IPSL. PISCES is an ecosystem model following the oceanic carbon cycle. It depicts the cycles of matter in suspension and nutrients. Four groups of plankton are represented, two groups of phytoplankton (diatoms and nanophytoplankton) and two groups of zooplankton (microzooplankton and mesozooplankton). The nonliving matter is also represented. The Eco3M is a modeling tool developed specifically for the biogeochemical processes of the Mediterranean ecosystems since it allows to model the planktonic growth submitted to multiple nutrient limitations.

Until now the MORCE platform has been mainly used for the study of ocean and atmosphere coupled processes in the Mediterranean, and on the effect of vegetation on heat waves and atmospheric component (Chapter 4). Further developments are in perpective, to couple :

1. the atmospheric and chemicals model to include the interactions between atmospheric composition, radiative budget and nucleation processes

2. the land surface and the ocean, in order to include the river runoff (a key issue for the Mediterranean sea level variability and the sea surface temperature evolution).

and to integrate in WRF the physical parameterization of the IPSL global circulation model LMDZ (*Hourdin et al.*, 2006) to improve the physics consistency when using the MORCE platform for downscaling the IPSL global Earth Simulator IPSL-CM.

A challenge of RCMs which are forced by an external, large scale field is to detect the changes inside the simulated domain induced by an increased resolution or by the change of the physical configurations which both can lead to incoherences with the large scale field.

2.2.3 WRF/ORCHIDEE coupling

WRF already includes several "classical" interactive land-surface models that compute the heat and moisture flux from soil water content and temperature. However, these LSMs have a low degree of sophistication and do not include carbon cycle and dynamic vegetation. In addition to these LSMs, the MORCE platform includes the ORCHIDEE land surface scheme.

ORCHIDEE has already been implemented in the LMDZ, the atmospheric module of the IPSL global Earth system IPSL-CM (*Polcher et al.*, 1998; *Hourdin et al.*, 2006). Its primary function is to provide reasonable boundary conditions for the atmospheric model. They are designed to operate along similar spatial scale. Integrated within a non-hydrostatic mesoscale model, we can take advantage of downscaling downto horizontal resolution of few kilometers and a high frequency coupling with the atmosphere. In

MORCE, it has also been implemented in the same way as the others land surface model already present in WRF. The surface atmosphere coupling frequency is the WRF time step $\Delta t_{cpl} = \Delta t_{atm}$. The variables between models are exchanged at high frequency compared to a GCM coupling, compatible with the turbulent processes in the atmospheric model. Indeed, in WRF, $\Delta t_{atm} \sim 3 - 6\Delta x$ where Δt_{atm} is the time integration in seconds and Δx is WRF horizontal resolution in kilometers. So for $\Delta x \sim 10$ km, $\Delta t \sim 30 - 60$ s. In addition to wind, air potential enthalpy, pressure and temperature and air humidity at the lowest level, WRF provides the drag coefficient for heat and moisture, as well as the short wave and long wave incoming radiation flux at the surface (Fig. 2.3). Precipitation is decomposed into rain and snowfall rate per seconds. Global atmospheric carbon concentration is held constant during the year but can vary from one year to the other. WRF receives in return the albedo, surface roughness, emissivity and sensible heat flux, latent heat flux, evaporation, and runoff split into river runoff and coastal outlet runoff. The heat flux is calculated using bulk aerodynamic formulas. Latent heat is a weighted average between snow sublimation, soil evaporation, canopy transpiration and interception loss. Their variables depend mainly of aerodynamic, canopy, architectural and soil resistance. Albedo and surface roughness are average values over each type of PFT and bare soil. Surface roughness depends on tree height. Constant albedo values are prescribed for each PFT and for bare soil, the albedo depends on soil color and moisture (*Wilson and Henderson-Sellers*, 1985). As ORCHIDEE has been designed for a coupling with LMDZ and an off-line usage, the coupling has been straightforward. Inspired by the general surface atmosphere interface prospect in *Polcher et al.* (1998), the subroutine intersurf.f90 of ORCHIDEE and module_ surface_driver.F of WRF contains the information needed and so the technical implementation was simple. However in contrast to LMDZ, coupling is in an explicit method owing to the shorter time step and WRF numerical structure. It is particularly suited for tiled model. It implies that energy is conserved and the fluxes calculated from energy balance are given to atmosphere module during the same timestep (*Polcher et al.*, 1998). Because the two models use different methods to determine the precision of real and integer variables, some adaptation of the makefiles is needed before compilation.

The sequence of calculations into a timestep carried out by our coupled model is conceptually outlined as follows :

1. Third order Runge-Kutta time integration.
2. Computation of non time split physics including the surface physics and the call to LSM.
3. Small (acoustic, sound) timestep loop - within the Runge Kutta sub steps.
4. Scalar advance for moist and chemical scalar variable.
5. Time split physics after the Runge-Kutta step (i.e. microphysics currently).

During the step 2, friction velocities and exchange coefficients are calculated by the surface layer scheme. This scheme provide also the the surface fluxes and surface diagnostic fileds over water surface. A physical and numerical unit change is performed just before the call to ORCHIDEE.

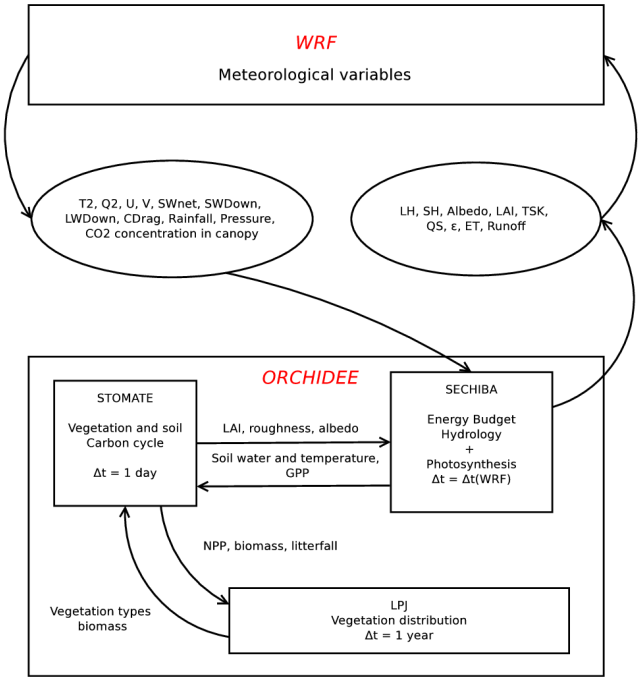

Figure 2.3: The WRF/ORCHIDEE coupling flow chart within the MORCE regional Earth system.

Chapter 3

Role of soil moisture during heat waves

This chapter is a synthesis of two articles : (*Stéfanon et al.*, 2012a) and (*Stéfanon et al.*, 2012c) published in Environnemental Research Letters and submitted to Climate Dynamics respectively.

3.1 Heat waves classification over Europe and the Mediterranean region

Triggered by large-scale atmospheric forcings, Mediterranean regional heat waves are often amplified by surface preconditioning, such as negative soil moisture anomalies and vegetation state. *Vautard et al.* (2007) proposed a mechanism where the cloudiness anomaly is advected from Southern Europe towards the North.

In this section, we want to take a more regional – event based – approach. One single heat wave event normally covers an area smaller than the continental, it is the scale of the typical synoptic anomalies in the area, namely few thousands kilometres. Distinguishing between different events, it may be asked which of the physical mechanisms above are preponderant to trigger or amplify a heat wave. As first step in that direction, therefore, is to establish an objective definition of heatwave event and identify the typical heawaves of Europe. We use a clustering approach to distinguish classes of heat waves events, following their geographical pattern. We also make a preliminary study on what are the specific processes that are associated with the different classes with respect to the synoptic situation and the hydrological precoditioning.

The section is organized as follows. In subsection 3.1.1, we propose a definition of heatwave event and describe the clustering method. In subsection 3.1.2, we apply the clustering method to partition the set of previously defined heatwave events into typical classes. The classes are described and the atmospheric and hydrological conditions during and before the heatwave events are detailed. Subsection 3.1.3 discusses both the methodology and the results. Conclusion are given in subsection 3.1.4.

3.1.1 Methodology

Data Source

We use a gridded version (E-OBS 3.0) of the European Climate Assessment & Data (ECA&D) (*Tank et al.*, 2002) for continental surface temperature (mean, minimum and maximum) and precipitation (*Haylock et al.*, 2008). Hereafter, only maximum temperature and precipitation will be used for our

study. The grid resolution is $0.5^\circ \times 0.5^\circ$ and the data span from 1950 to 2009. Data observations were aggregated from several weather stations and gridded using an interpolation procedure combining spline interpolation and kriging. The interpolation smoothes the peak values inducing a 1.1°C decrease of the median value of maximum temperature, if we consider an extreme event with a ten year return period (*Haylock et al.*, 2008). We select a domain over Europe and the Mediterranean region whose latitudinal and longitudinal boundaries are 30°N—70°N, 15°W—45°E, respectively.

The study period is 1950 to 2009 (60 years) for which daily geopotential data from National Centers for Environmental Prediction reanalysis (*Kalnay and et al*, 1996) were simultaneously available with $2.5^\circ \times 2.5^\circ$ horizontal resolution available every 6 hours. The reanalysis provides a complement for information about middle tropospheric conditions with the 500mb geopotential height. For NCEP data the domain considered is extended to 30°N—70°N, 70°W—45°E.

Data Processing

Heatwave definition

A range of weather-related and bioclimatic indices have been developed for heat wave definition, which relevance regarding the impact on the natural and social system and on human health have been reviewed in a number of reports and articles (*Robinson*, 2001; *WHO*, 2004; *Laaidi et al.*, 2004; *Davis et al.*, 2006). In this work, we use a simple definition based on temperature only: an extreme event is defined when the temperature exceeds a given threshold, and we impose additional constraints on the spatial and temporal extensions to avoid spurious intermittent and local events. Only summer is considered (June to August). In detail, a heatwave region is defined using the three following steps:

1. Temperature threshold: for each grid point, we consider a temperature anomaly with respect to the climatology (1950-2009) to be an extreme when its value exceeds the upper 95^{th} centile of the local probability density function. The probability density function is computed for day D using the temperature data of the the 60 year climatology between D-10 days and D+10 days. For example to compute the 95^{th} centile on 10 August at a given point, we use the local temperature values between the first and 21 August of the 60 years between 1950-2009.

2. Spatial extension: taken a square of side L, there must be at least a fraction α of the surface where the temperature exceeds the upper 95^{th} centile, using weights on the cosine of latitude. In this case, the central point of the square is retained as a heatwave point. This allows eliminating isolated "hot" gridpoints. A sliding scan is performed with the square of side L over the whole domain. In the following, the results are shown for $\alpha = 0.6$ and $L = 3.75^\circ$ in latitude and longitude. The sensitivity to the value of this parameters is investigated in Section 3.1.3.

3. Temporal extension: the above criteria are to be satisfied over at least 4 consecutive days. The temporal criterion is applied counting also adjacent regions. More precisely, when two heatwave squares overlap by more than 40% of their surface, they are retained as one single coherent event. This criterion thus allows to smooth off some of the intermittency in the temperature signal, as well as to account for propagating phenomena.

Classification of heatwave patterns

The above procedure identifies 78 heatwave events of 643 days total duration. The existence and characterization of typical heatwave patterns for the Euro-Mediterranean are sought and a clustering technique is described hereafter for the classification.

Cluster analysis has been classically used in atmospheric sciences as a way to characterize midlatitude weather. For a complete introduction to clustering methods see e.g. (*Tan et al.*, 2006), for an extensive review of their use in atmospheric sciences, see (*Smyth et al.*, 1999) and references therein. The main difficulty is that only rare events are investigated, which by definition reduces the sample size for the clustering analysis. In this work, we have devised a clustering methodology that enhances the dissimilarity of the dataset. The clustering technique consists of three steps.

1. A pre-filtering of the data is performed. For each day belonging to one event, the temperature anomaly values at all grid points which are smaller than the 95^{th} centile is set to zero.

2. All pre-filtered daily maps belonging to one event are averaged producing "event maps".

3. An agglomerative hierarchical clustering algorithm is applied to the event maps. At the initial step, each event map forms a cluster. The two "nearest" clusters are then merged by pair into a new cluster. The distance between two clusters is measured using a metric defined below. This procedure is iterated until a stop criterion, defined hereafter, is met. The stop criterion sets the number of clusters.

All clustering methods require a metric definition d. Here, we use a pseudometric based on the anomaly correlation coefficient r, called also cosine similarity. First, we define a distance d' between any two maps $\mathbf{p}$ and $\mathbf{q}$ as :

$$d'(\mathbf{p},\mathbf{q}) = 1 - r(\mathbf{p},\mathbf{q})$$

with

$$r(\mathbf{p},\mathbf{q}) = \frac{\sum_{i=1}^{N}\sum_{j=1}^{M} p_{ij}, q_{ij}}{(\sum_{i=1}^{N}\sum_{j=1}^{M} p_{ij}^2 \times \sum_{i=1}^{N}\sum_{j=1}^{M} q_{ij}^2)^{\frac{1}{2}}}$$

where $\mathbf{p}$ and $\mathbf{q}$ refer to the maps which are matrices of size M by N along the longitudinal and latitudinal axes respectively, as in (*Cheng and Wallace*, 1993).

The quantities $p_{i,j}$ and $q_{i,j}$ are the values of $\mathbf{p}$ and $\mathbf{q}$ at coordinates (i,j) along the longitudinal and latitudinal axes, respectively. The distance between two clusters C_1 and C_2 is then computed as the distance between their two farthest members, in other terms:

$$d(C_2,C_1) = max(d'(\mathbf{p},\mathbf{q}))\, for\, all\, \mathbf{q} \in C_1,\, \mathbf{p} \in C_2$$

This definition of distance is particularly suited to distinguish between different spatial patterns of the temperature anomalies, while it is less sensible to the amplitude of the temperature anomalies. \$d=1\$ corresponds to orthogonal vectors, whereas $d = 0$ is for parallel vectors with a positive coefficient. Moreover d can be larger than 1 when vectors are anticorrelated.

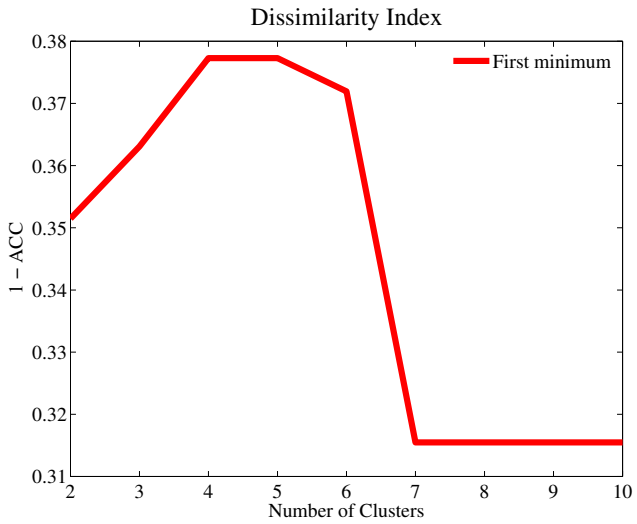

Figure 3.1: Dissimilarity index (minimum inter-cluster distance) as a function of the number of clusters.

The optimal number of cluster is found by plotting a dissimilarity index as a function of the number of clusters (Fig.3.1). In any agglomerative clustering, the minimum distance can only continuously increase when number of clusters decreases. Here however this index is defined as the minimum of the average inter-cluster distance (i.e. the distance of the two closest clusters). It can be seen in Fig.3.1 that for 7 clusters and more, the minimum inter-cluster distance reaches a minimum and remains almost constant. Increasing the number of clusters from 6 to 7 means that one of the clusters is split into two clusters. The distance between these latter two clusters is very small because they remain very similar. In other terms, more partitions do not provide different patterns but merely place random borders within similar patterns. For much higher number of clusters (not shown), the dissimilarity index further decreases and reaches values that are indistinguishable from the dissimilarity of purely random partitions of the dataset.

A cross validation procedure is used to check the stability of our classification. We eliminate 10 years of the dataset to use as a verification period, and perform the clustering on the remaining 50 years. Heat waves from the verification period are then associated to the 6 new clusters, according to the nearest distance. We compare the membership of the verification period episodes to the new 50-years clusters to the membership of the full period clusters. This procedure is repeated six times for six sections of 10 years over the 60 years of record. A stability score is then computed by cluster: it is the ratio of the number of verification period heat waves that are correctly attributed over the total number of heat waves in the cluster.

These results are compared to a Monte Carlo test. The Monte Carlo test is constructed by proceeding as above, except that heat waves from the 10 years verification period are associated to the 50-years clusters in a purely random way, and the procedure is repeated 1000 times. From this, we estimate a PDF of the null hypothesis that the verification period heatwaves cannot be classified in the clusters obtained in the 50-years period. The six clusters are significant to a 99% level.

3.1.2 Heat waves clusters

patterns description

Figure 3.2 shows the six typical heatwave patterns obtained after clustering. The patterns are represented by the average of temperature anomaly and 500-hPa geopotential height of all event maps of each cluster. The main geopotential anomaly structures are all significantly different from zero according a two-sided t-test at the 99% level. The six patterns are labeled by a geographical acronym in the upper-left corner.

The RU (Russia) cluster groups 128 days into 14 events. This class expands in the very north-eastern part of the domain over Russia between 35° and 45°E with a temperature anomaly up to 4°C. It has a shape that is very similar to the one observed during the catastrophic Russian heatwave of summer 2010, although - notably - data from 2010 were not included in the analysis. The WE (Western Europe) cluster is centered mostly over France and has a magnitude of 5°C. It includes 11 events for 82 days. The first half of August 2003 belongs to this cluster. The temperature anomaly pattern of the 2003 heatwave is very similar to the our WE pattern, if compared for instance with *Schär et al.* (2004). The temperature anomaly pattern displays a maximum North of the Alps and extends to the North and to the West with a slightly decreasing magnitude towards the Atlantic coast. The EE (Eastern Europe) cluster is approximately centered over Poland. Its magnitude is 4°C with 23 events for a total of 182 days. Its is relatively more spread out than the other clusters. A visual inspection of the different event maps shows events localized around the Baltic Sea and the Black sea. The IB (Iberian) cluster is located over the Iberian Peninsula, with a second center over Turkey, along the same latitudinal band across the Mediterranean. It includes 75 hot days in 9 heatwaves events and displays the weakest temperature anomaly with maximum 3°C. The NS (North Sea) cluster is the hottest, with a magnitude exceeding 6°C above the mean. It includes 81 hot days in 11 events. The anomaly is centered over the North Sea and spans over Great Britain to the west, the Northern European coast and Eastern Scandinavia. Summer 1976 was very similar to the NS pattern when compared for instance with *Fischer et al.* (2007b). Finally, the SC (Scandinavian) cluster extends over most of the Scandinavian Peninsula with anomalies up to 6°C. It includes 95 days in 10 events. The temporal succession of heatwave events is shown in Fig. 3.3. Notable recent events are present, for example the 2003 and 2006 West European heatwaves, or the North Sea event of 1976. Our methodology gives a heatwave duration of about one week for WE, EE, IB and NS whereas it is 9 for RU and SC events.

From Fig. 3.2, we can see that all clusters have an anticyclonic anomaly in phase with the temperature anomaly. This is consistent with what is shown in the literature by many studies describing the climatology of heat waves. The European summer blocking high is visible in cluster WE as in *Black et al.* (2004) or in *Cassou et al.* (2005). The Ural blocking high is associated with the RU heatwave, as seen in 2010 (*Barriopedro et al.*, 2011). The only notable exception to the phase lock between the anticylone and the temperature anomaly is the IB cluster. This cluster seems to be associated with a pattern similar to that of the EE cluster, with a high pressure over central Europe and a low over the Atlantic Ocean. In the IB cluster the peculiar position of the Atlantic low puts the Iberian Peninsula under southerly wind conditions. A similar condition can be seen over Turkey. It has already been observed that Iberian heatwaves tend to be triggered by warm advection from the Tropical Atlantic Ocean (*Garcia-Herrera et al.*, 2005). The connection with the Eastern Mediterranean is less obvious and could be due to a northward displacement of the subsiding part of the Hadley circulation.

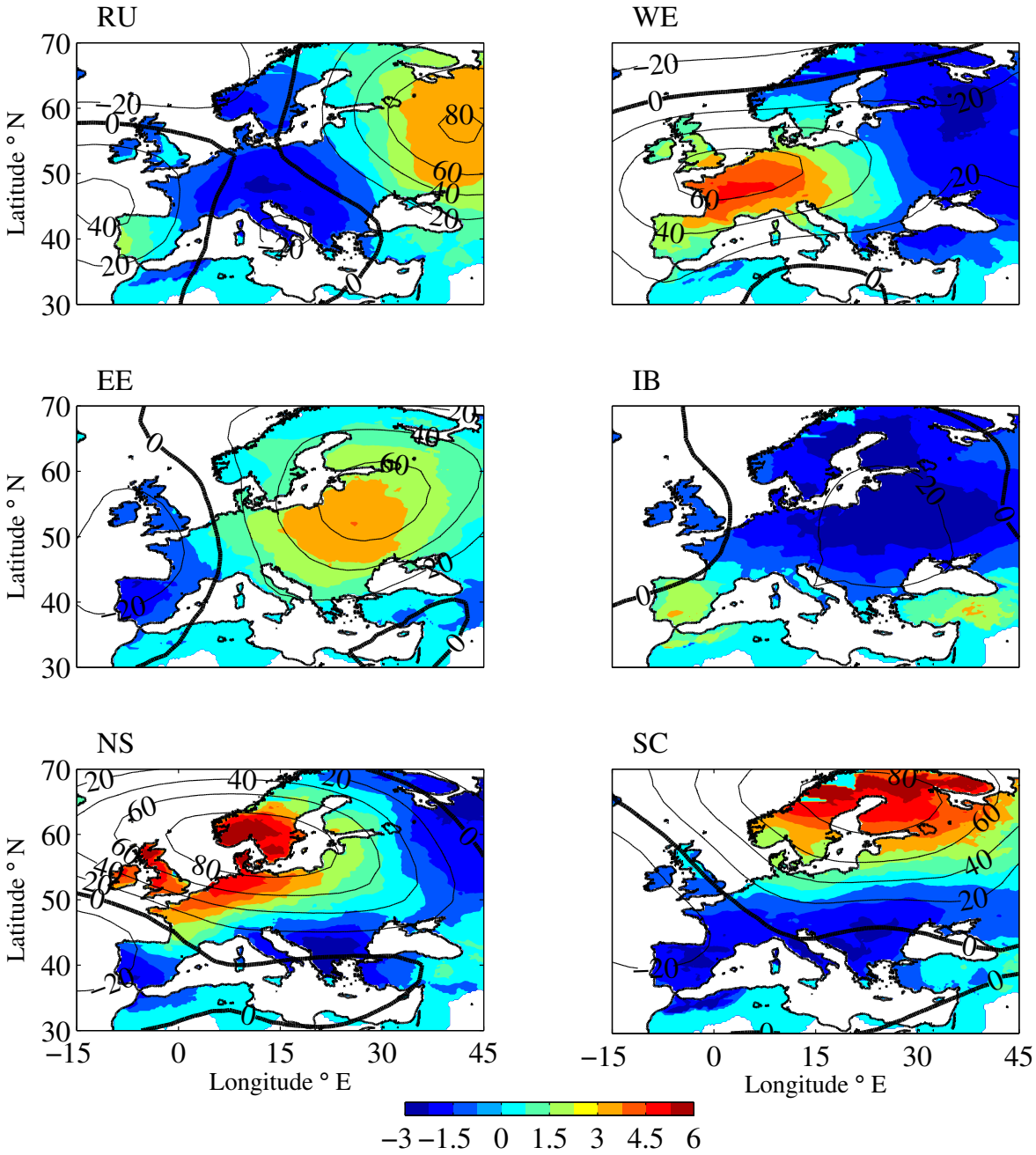

Figure 3.2: Six heatwave patterns obtained by hierarchical clustering algorithm for the Euro-Mediterranean region: (a) "Russian" cluster (RU), (b) "Western Europe" cluster (WE), (c) "Eastern Europe" cluster (EE), (d) "Iberian" cluster (IB), (e) "North Sea" cluster (NS) and (f) "Scandinavian" cluster (SC). Daily maximum temperature anomaly are in colour and expressed in deg K and isolines are the 500-hPa geopotential height anomaly.

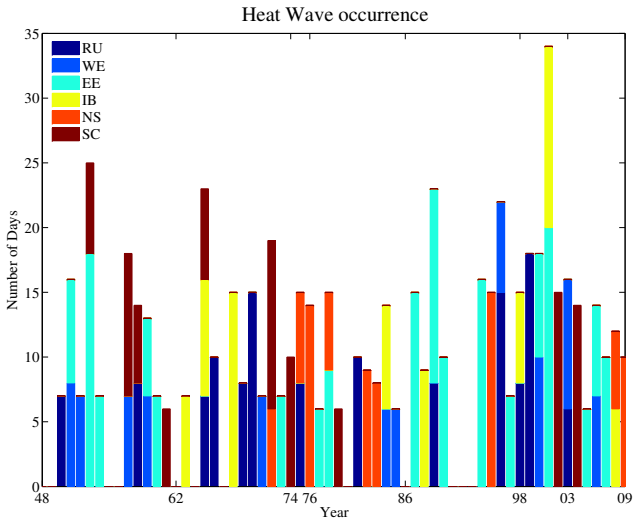

Figure 3.3: Heatwave climatology in the Euro-Mediterranean between 1950 and 2009 with attribution to the 6 heatwave clusters.

Hydrological preconditioning

The importance of the soil moisture preconditioning in the context of heatwaves has been already emphasized by a number of studies (*Huang and Van Den Dool*, 1992; *D'Andrea et al.*, 2006; *Ferranti and Viterbo*, 2006; *Seneviratne et al.*, 2006; *Fischer et al.*, 2007b), and drought conditions have often been shown to precede summer high amplitude temperature anomalies. As suggested by *Vautard et al.* (2007) and *Zampieri et al.* (2009) for the particular case of continental Europe, droughts in Southern Europe seem to precede heatwaves occurring in the most continental part of Europe.

In Fig. 3.4, the sensitivity of the temperature anomaly to the preceding hydrological conditions is thus analyzed for each cluster. Figure 3.4 shows the correlation between the rainfall occurrence anomaly between January and May, and the detrended summer maximum temperature anomaly at the heatwave location (the rainfall occurrence is the percentage of days between January and May for which daily accumulated rainfall exceeds 0.5mm). We choose the frequency of rainy events as a proxy for soil moisture as in *Vautard et al.* (2007) and *Findell et al.* (2011).

Considering that the correlation may not be latitudinally in phase as discussed in *Vautard et al.* (2007), we plot in Fig. 3.4 the correlation as a function of different latitudinal bands. For WE and EE clusters, we can see a significant negative correlation between the rainfall occurrence anomaly and the summer maximum temperature anomaly between 40 and 45°N. This means that in Western and Eastern Europe, a positive temperature anomaly in summer (heatwave) is associated with a precipitation deficit in winter and spring in Southern Europe. This confirms with a different approach and over a larger region the results of *Vautard et al.* (2007) and *Zampieri et al.* (2009) which suggest that droughts in the south cause unusual low cloud cover which is then transported northward, reduce the convective instability and enhance the anticyclonic conditions. However, this process is not as dominant for NS cluster for which the correlation is only marginally significant. In the case of IB, the heatwave is co-localized with the preceding rainfall deficit. The SC and RU clusters do not seem to be pre-conditioned by any rainfall occurrence anomaly.

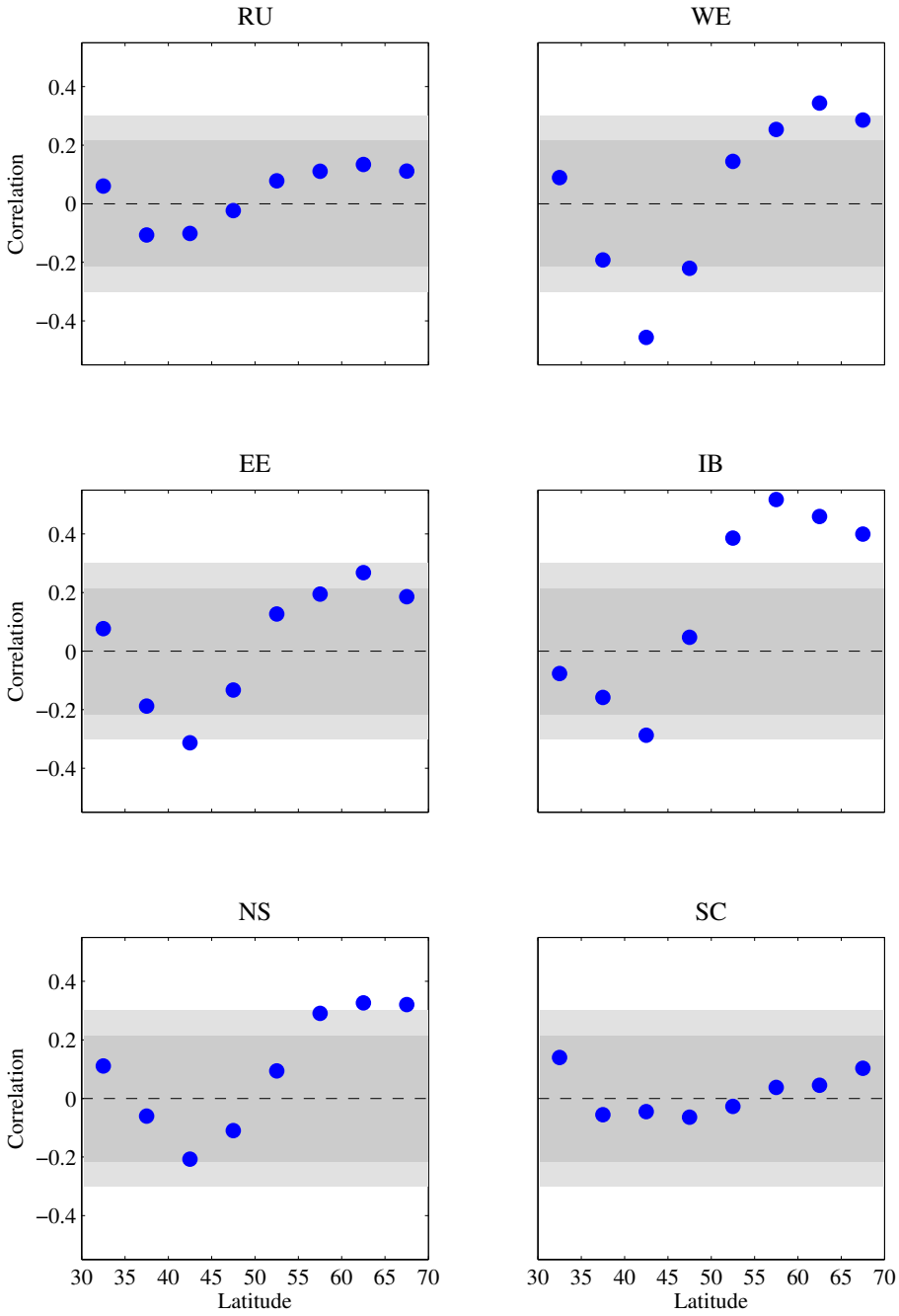

Figure 3.4: Correlation between the rainfall occurrence anomaly between January and May, and the detrended summer maximum temperature anomaly at the heatwave location (the rainfall occurrence is the percentage of days between January and May for which daily accumulated rainfall exceeds 0.5mm). Dark grey shaded area indicates the 95% confidence interval bounds, whereas the light grey shaded area is for the 99% confidence interval bounds.

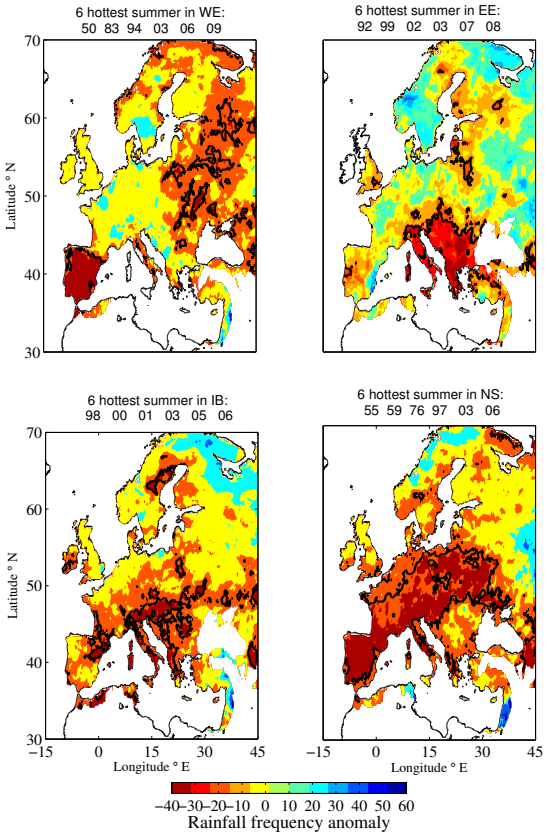

Figure 3.5: Composites of rainfall occurrence frequency anomaly from January to May, for the six hottest summer for WE, EE, IB and NS. Solid line represents the 90% confidence level.

The correlations show a dipolar structure, with high correlation, significant in some clusters, with the northernmost latitudinal bands: these are probably due to a balance effect between northern and southern Europe. When rainfall decreases over Mediterranean Europe, it increases over northern Europe and vice-versa. Such phenomenon has been highlighted in previous studies and is very likely a manifestation of the North Atlantic Oscillation. *Dai et al.* (1997) show evidence of an anti-correlation of the patterns of annual precipitation anomalies, between Scandinavian and continental Europe as well as the Mediterranean region. The existence of such dipole is also illustrated in *Uvo* (2003) during DJFM (winter months). *Uvo* (2003) links the precipitation pattern to the different phases of NAO. In our case, the relation between heat wave and precipitation deficit in Southern Europe has a physically based explanation, as discussed in *Vautard et al.* (2007) and *Zampieri et al.* (2009). Conversely, we think that the positive correlation with precipitation excess in Northern Europe is purely statistical.

For the six hottest summer of cluster sensitive to Mediterranean drought (WE, EE, IB and NS), we show the rainfall structure over the entire domain stratified by clusters in Figure 3.5. The pattern significance is assessed with a bootstrap method where samples of six different years are randomly picked over 1950-2009. We notice a shift in the water deficit along the longitude, fairly consistent with heat wave pattern location. It is especially striking for EE cluster.

3.1.3 Discussion

Classification method

There are three main parameters in our heatwave definition and classification method: the temperature anomaly threshold, the side of the scanning square L and the fraction α of the square area that must exceed the temperature threshold. In order to test the reproducibility of our results, we performed a sensitivity study where L and α have been modified. Modifying the threshold has a large impact on the results, but that amounts to changing the very definition of extreme events. The value of L has been varied between 2 and 7.5° of latitude and longitude. The difference in the total number of hot days selected was never larger than 40. Using a larger size L would not be appropriate because at this scale the number of sea points included in the square (that are excluded from the computation of the temperature threshold) would become very large. The parameter α does not modify the number of hot days for values ranging between 0.4 and 0.8.

The final list of 78 heat waves also compares well with other lists found in the literature. It includes 7 of the 10 hottest summers of *Vautard et al.* (2007), which can be considered a good agreement given the difference of the domain and the definition of heatwave. A comparison with data from by Météo France on the 14 reported heat waves in France between 1950 and 2009 also shows good agreement (see http://comprendre.meteofrance.com/content/2010/5/23587-43.png). 8 of their 10 episodes longer than 4 days are also present in our classification in either cluster WE or NS. The missing ones are absent from our list because they are classified as too short.

A similar study with minimum and mean temperature has also been performed. The hot days selection using mean temperature are very close to the one using maximum temperature: it gives a total of 717 days, with a 83% overlap. The classification applied to minimum temperature is tantamount to a classification of hot nights. This gives a much smaller number of events, and a much smaller total number of hot nights (280). Most of the hot nights also correspond to a hot day (81%).

Heatwave Classes

Varying the value of L does not change substantially the shape and the extent of the cluster patterns of Fig. 3.2. Indeed, the size and shape of the heatwave patterns is controlled by the size of the persistent anticyclone that controls in part the heatwave. As explained in many previous papers [e.g. *Black et al.*, 2004; *Vautard et al.*, 2007], heatwave events are primarily caused by the synoptic conditions. However, the pre-existing hydrological condition can influence the events by amplifying the temperature anomaly (*Fischer et al.*, 2007b). We show in this study that the local or remote pre-conditioning by favorable hydrological conditions is not a universal feature for heatwave, as shown for SC and RU clusters (Fig. 3.4).

In *Koster* (2004), it has been shown that the coupling between soil moisture and precipitation is active mainly in certain regions which they call "hot-spots". Hot Spots are located in transitional hydroclimatic regimes characterized by intermediate mean values and high variability of soil moisture as well as intermediate values and high variability of precipitation. In very humid areas, soil moisture tends to saturate and there is weak dependence between evapotranspiration and soil moisture. In a dry environment, tropospheric conditions are unfavorable to moist deep convection. Between these dry and moist extremes, there is potential for land surface-atmosphere feedbacks.

In the context of heatwaves, it appears from our analysis that continental Europe shows the highest sensitivity to a pre-existing drought. Somewhat disappointing, Europe does not appear in the hot-spot map of *Koster* (2004), although the importance of soil moisture has been clearly highlighted in the many studies cited above. This probably has to do with the specific metric used by *Koster* (2004) and with the fact that their study is based on global models [for more details see the review by *Seneviratne et al.* (2010)].

In the Scandinavian region (SC cluster), the land-vegetation system is rarely in water-limited conditions in summer. Moreover, its climate remains more dynamical than convective, being influenced by the polar front. The NS cluster shows a signal of sensitivity to soil moisture although it remains not significant. This is probably explainable with a sensitivity of the southern fringe of the region, located on the coast of the North Sea. The case of the RU cluster is somewhat different, for one might expect that the temperate forestal areas of central Russia to satisfy the properties of the hot spots. However, it is possible that hydrology in those areas is influenced by more complex processes, like snow cover and snow melt, which make the proxy we used - rainfall anomaly occurrence - less pertinent. This class of heatwaves deserves further study, also in the light of the 2010 event.

3.1.4 Summary and Conclusion

In this section we perform a heat wave classification over the period 1950-2009 on the Euro-Mediterranean region has been carried out by means of a gridded observation dataset. Our definition of heat waves is consistent with official data and literature, including all the major events of the last decade. Despite the difficulty inherent in the limited data available, the classification algorithm partitions the 78 heatwave events into six classes: Russian, West European, East European, Iberian, Scandinavian patterns and one last pattern centered over the North Sea. These are the typical heatwaves of Europe.

High temperatures are co-localized with fair weather and a high-pressure system. This brings an increase of radiative forcing and thus sensible heat flux and temperature rise. Heatwaves in WE and EE clusters are preceded by rainfall deficit in Southern Europe, as in *Vautard et al.* (2007). This is not the case for the northernmost clusters (SC and RU). The Iberian pattern is caused by warm air advection from the south and is preceded by a drought at the same location of the heatwave.

Based on these results, the question is now to evaluate the role of vegetation with soil moisture and climate, upstream and during extreme event. In the two next chapter we attempt to respond to this question by coupling a non-hydrostatic model (the Weather Research and Forecast model - WRF), with the dynamical vegetation global model developped at IPSL (ORCHIDEE). Chapter 2 describes the coupling technique, the nature of the data exchanged between the different modules and concludes with a validation with others LSMs. Chapter 4.1 illustrates with scientific results the application of the coupling for the 2003 summer heat waves.

3.2 The soil-moisture temperature feedbacks during heat waves at mesoscale

Heat waves in the Euro-Mediterranean region have been classified in the previous section. Heat waves in Western and Eastern Europe are preceded by rainfall deficit in Southern Europe (*Vautard et al.*,

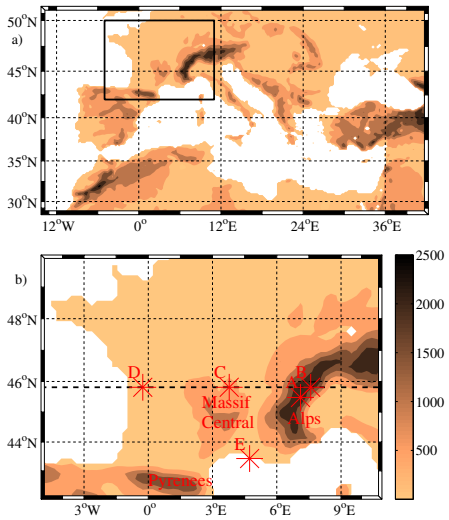

Figure 3.6: Panel a: Domain of the HyMeX/MED-CORDEX simulations covering Europe and the Mediterranean region. The rectangle indicates the domain of investigation of this study detailed in panel b. In panel b, the dashed line and the letters indicate the location of cross sections and point analysis performed in subsection 3.2.4. The olor shading indicates the topography elevation.

2007; *Stéfanon et al.*, 2012a), showing evidence of a possible soil-moisture temperature feedback. Here we focus the analysis over France (Fig. 3.6) which matches with the Western Europe pattern of Fig. 3.2. This region is featured by numerous mountains (Pyrénées, Massif Central, and the French Alps), irregular coastlines, land cover heterogeneity which cause meso-scale circulation in the boundary layer such as valley winds (*Drobinski et al.*, 2001, 2005; *Guénard et al.*, 2005, 2006), inland and sea breezes (*Bastin and Drobinski*, 2005, 2006; *Drobinski et al.*, 2006) which play a key role in water vapor transport (*Bastin and Drobinski*, 2005; *Bastin et al.*, 2007). It is also sensitive to soil moisture-temperature coupling (*Seneviratne et al.*, 2006).

Several process studies have investigated mechanism controlling the link between soil moisture, temperature and precipitation. *Eltahir* (1998); *Zheng and Eltahir* (1998); *Schär et al.* (1999); *Clark et al.* (2004) have suggested that wet soils produce a shallow boundary layer, with a low level of free convection and a high level of moist static energy. At local scale these elements can enhance convective activity. However the sign of the soil-moisture precipitation remains an open question. *Hohenegger et al.* (2009) conducted sensitivity experiments for July 2006 over the Alpine region with a a cloud resolving model run at 2.2 km resolution. They show that a drier soil yield an enhancement of sensible heat flux, and this surface warming produce thermals able to pierce the layer of stable air above the boundary layer owing to the explicit treatment of convection. The shallow convection ultimately causes a negative soil moisture-precipitation feedback. They also found that in regional climate models run at 25 km resolution, different parameterizations of convection could produce either negative or positive soil moisture-precipitation feedbacks.

There are thus large remaining uncertainty on (1) the sign of the precipitation/soil moisture feedbacks and (2) its impact on boundary layer temperature. This section investigates with WRF the impact of soil moisture-temperature feedback on meso-scale on the heat waves occurring between 1989 and 2008. One fundamental motivation is to investigate the role of meso-scale boundary layer dynamics generally

produced by the land-surface heterogeneity (e.g. mountainous or coastal regions) on the sign of the soil moisture-precipitation feedback and thus on the magnitude of the temperature anomaly of the heat wave.

The section is organized as follows. The numerical model, its configuration and set-up, as well as the validation dataset are detailed in subsection 3.2.1. A detailed analysis of the hydrological cycle as simulated in the two simulations and the comparison with data is provided in subsection 3.2.3. Subsection 3.2.4 describes the physical processes involved in the boundary layer structure and the surface energy budget. The discussion and conclusion are given in section 3.2.5.

3.2.1 Experimental design

Atmospheric modelling

For this study we use the Weather Research and Forecasting (WRF) model of the National Center for Atmospheric Research (NCAR) (*Skamarock et al.*, 2008). The regional domain has a 20 km horizontal resolution (249×129 grid points) and covers southern Europe and Mediterranean, the western Russia at its eastern boundary (42°E) and the Gibraltar Strait at its western boundary (13°W). It has 28 sigma-levels in the vertical. Initial and lateral conditions are from the ERA-Interim reanalysis of ECMWF (*Dee et al.*, 2011; *Simons et al.*, 2007) provided every 6 hours with a 0.75° resolution. A complete set of physics parameterizations is used with the WRF Single-Moment 5-class microphysical scheme (*Hong et al.*, 2004), the new Kain-Fritsch convection scheme (*Kain*, 2004), the Yonsei University (YSU) planetary boundary layer (PBL) scheme (*Noh et al.*, 2003) and a parameterization based on the similarity theory (*Monin and Obukhov*, 1954) for the turbulent fluxes. The radiative scheme is based on the Rapid Radiative Transfer Model (RRTM) *Mlawer et al.* (1997) and the *Dudhia* (1989) parameterization for the longwaves and shortwaves radiation, respectively.

The Mediterranean domain is sufficiently small to produce strong control of the simulations by the boundary conditions (*Omrani et al.*, 2012) and avoid unrealistic departures from the driving fields. In addition indiscriminate nudging is applied with a nudging coefficient of $5 \times 10^{-5}\mathrm{s}^{-1}$ for temperature, humidity and velocity components above the planetary boundary layer (*Stauffer and Seaman*, 1990; *Salameh et al.*, 2010).

Numerical simulations

The approach consists in a sensitivity analysis between two 20-year simulations over the Mediterranean basin (Fig. 3.6) performed at 20 km resolution with WRF, coupled with the RUC and SLab LSMs (hereafter referred as RUC and SLab simulations, respectively). In one simulation (RUC), soil moisture can evolve freely by using a sophisticated land-surface model, while in the other (SLab), the soil moisture availability is prescribed and set to climatological wintertime value preventing any soil moisture deficit situation over France. These two simulations allow to assess the sign and magnitude of the soil moisture-temperature feedback and its variability at meso-scale. They are used to identify the dynamical meso-scale processes controlling the feedback loops and their local contribution to the temperature anomaly associated with the heat-wave events occurring over the 1989-2008 period.

Observational data

We use a gridded version (E-OBS 3.0) of the European Climate Assessment & Data (ECA&D) (*Tank et al.*, 2002) for continental surface temperature (mean, minimum and maximum) and precipitation (*Haylock et al.*, 2008). The grid resolution is 0.5°×0.5° and the data span from 1950 to 2009. Data observations were aggregated from several weather stations and gridded using an interpolation procedure combining spline interpolation and kriging. The interpolation smoothes the peak values inducing a 1.1°C decrease of the median value of maximum temperature, if we consider an extreme event with a ten year return period (*Haylock et al.*, 2008).

3.2.2 Representation of heat waves in the RUC and SLab simulations

Figure 3.7 shows cumulative distribution function (upper row) and probability density function (lower row) for summer daily maximum temperature (right column) and its respective temperature anomaly (left column), in ECA&D and WRF. Data are averaged over the domain indicated by a solid black box in Fig. 3.6. Panel b) and d) show evidence of a weak warm bias around 0.5°C between ECA&D and RUC while an important cold bias is near 4°C in SLab. For the standard deviation, RUC is slightly higher than ECA (respectively 3.77 and 3.64°C) whereas SLab is clearly lower (2.81°C). In temperature anomaly (panel a and c) the bias is removed, however the same statement are valid for the temperature standard deviation, with a slight decrease of 10%. Spatial differences between RUC and ECA&D median temperature (not shown) are organized as follows. Along the Mediterranean coast, in the South Western France and in some alpine valley (including the Rhône Valley) the warm bias is higher, around 2°C. In plain area this bias tends to zero whereas in mountainous regions it becomes negative, around -1°C with peak up to -3°C. We perform a similar comparison between SLab and ECA&D. Bias pattern is strongly negative and mostly structured around topography. The cold bias is weakened towards mountainous and coastal regions as in northern France. It is even fully corrected in the Alps, nevertheless in a opposite way it is strengthened, near the Pyrénées and in the Northern Spain, up to -7°C.

Figure 3.7 shows the probability density function and cumulative distribution function of summer daily maximum temperature and the corresponding anomaly with respect to the 20-year climatology from ECA&D data and RUC and SLab simulations. Data are averaged over the domain (see rectangle in Fig. 3.6). It shows evidence of a weak warm bias around 0.5°C between ECA&D and the RUC simulation and a large cold bias of about -4°C in the SLab simulation. For sake of legibility, the probability density function and cumulative distribution function of the temperature anomaly allow an easier comparison of the temperature anomaly variability. The standard deviation of the temperature anomaly is slightly higher than ECA&D in the RUC simulation (3.64 and 3.77°C, respectively) and lower in the SLab simulation (2.81°C). This suggests that soil moisture strongly controls the temperature mean, and to a lower extent the temperature variability which is mainly driven by the atmospheric synoptic conditions. Indeed, the temporal correlation coefficient of the summer daily maximum temperature averaged over the domain of investigation is 0.99 between the RUC simulation and ECA&D data and 0.97 between the SLab simulation and ECA&D data. The synoptic variability which is similar in the two simulations thus drives considerably the time evolution of the near surface temperature. However, looking in details, departures remain on the upper and lower tail of the probability density functions and cumulative density functions evidencing differences in the simulation of temperature extremes (and so heat wave events) when the

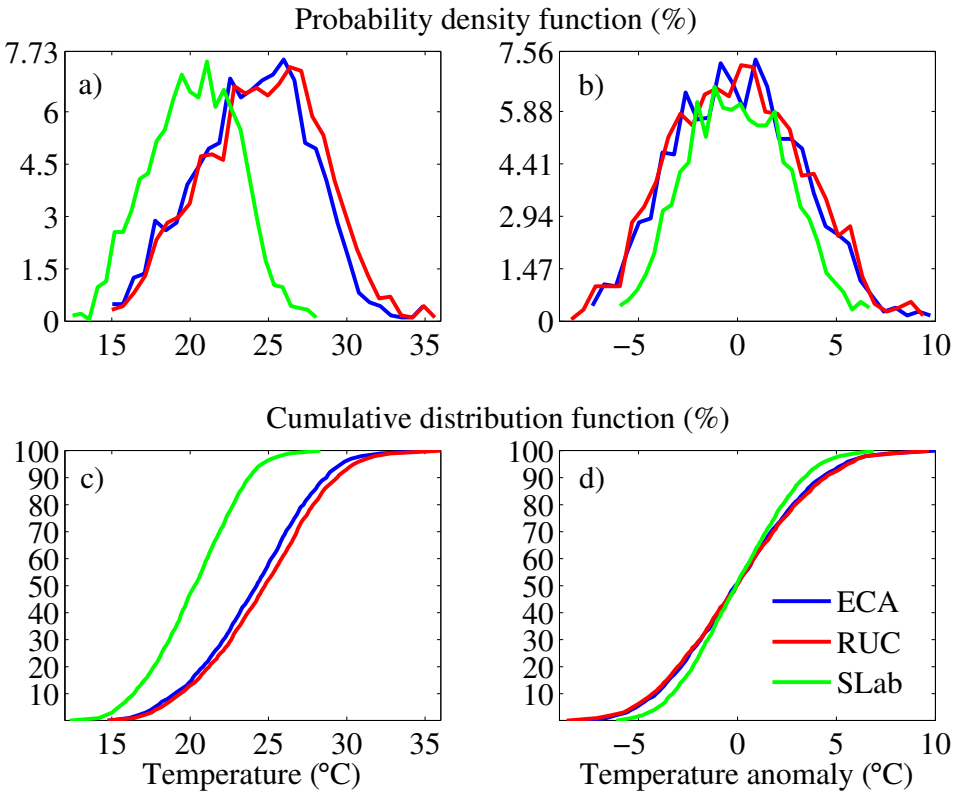

Figure 3.7: Cumulative distribution function (a-b) and probability density function (c-d) of summer daily maximum temperature (a-c) and the summer daily maximum temperature anomaly with respect to the 20-year climatology from ECA&D data and RUC and SLab simulations (summer corresponds to June-July-August, i.e. JJA). Data are averaged over the domain indicated by a rectangle in Fig. 3.6.

RUC or SLab LSMs are used. The probability density functions and cumulative density functions of the temperature anomaly show cold and warm extremes of lower magnitude in the SLab simulation than in the RUC simulation and ECA&D data. This suggests that besides the strong control by the atmospheric synoptic conditions of the heat wave build-up, its magnitude should be attributed to soil-atmosphere interactions.

Spatially, the patterns of the median of the summer daily maximum temperature display meso-scale variability. Along the Mediterranean coast, in South Western France and in the Rhône and Aude valleys, the RUC simulation is warmer by about +2°C with respect to ECA&D data. This bias is close to 0 in plains, whereas the RUC simulation is colder by about -1°C (and up to -3°C) in mountainous regions. Regarding the SLab simulation, besides the strong negative bias of the SLab simulation with respect to ECA&D data (and the RUC simulation), the pattern is similar with however a much lower impact of the SLab LSM in the mountainous regions. pronounced in the SLab simulation. In the two simulations, the temperature anomaly decreases near the Atlantic and Mediterranean coasts.

We now focus on the specific case of heat wave events. The days when heat waves occur are defined as days during which the daily maximum temperature anomaly with respect to the climatology exceeds the 95^{th} quantile. The 95^{th} quantile of the summer temperature anomaly, which allows to remove the

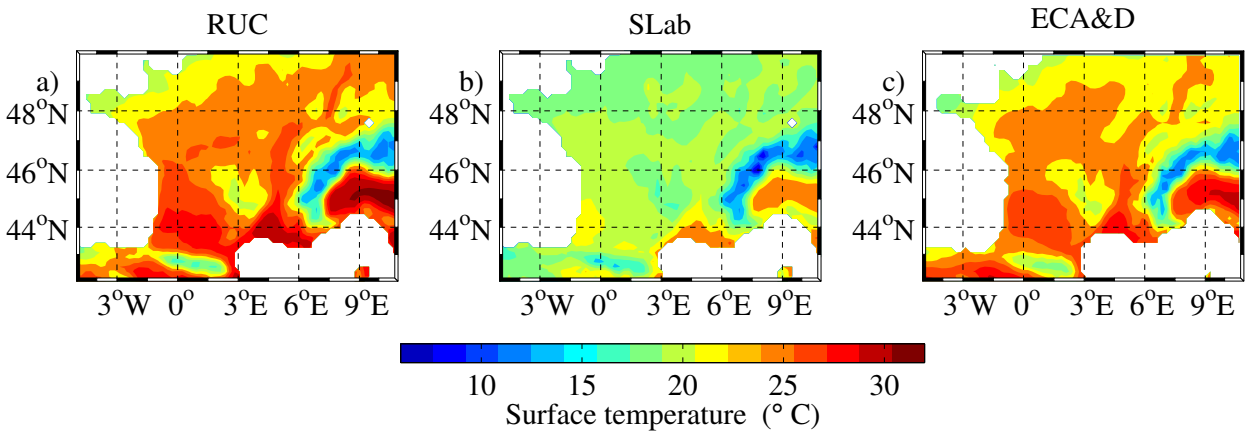

Figure 3.8: Median of the summer daily maximum temperature over the 1989-2008 period from the RUC simulation (a), the SLab simulation (b) and the ECA&D data (c).

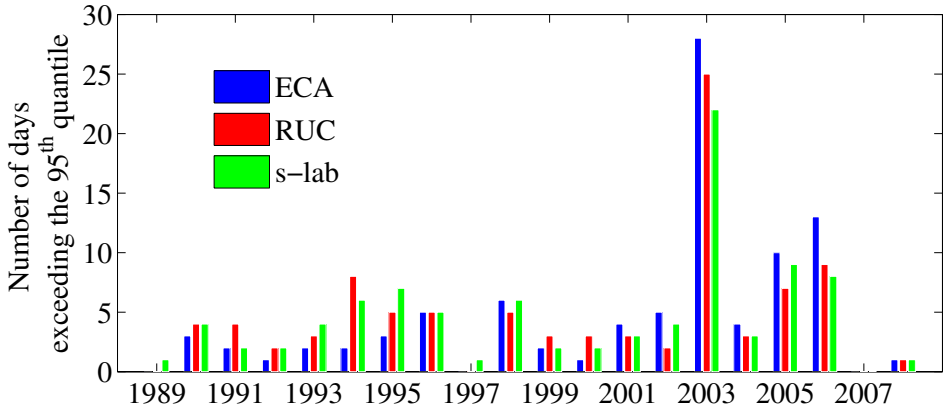

Figure 3.9: Heat wave days (temperature anomaly exceeding the 95^{th} for ECA&D data, RUC and SLab simulations.

seasonal cycle, is calculated for all days of June to August over the 1989-2008 period. The 95^{th} quantile of the summer temperature anomaly are 5.55, 4.16 and 5.39°C for RUC and SLab simulations, and ECA&D data, respectively. We obtain the dates of the heat waves occurring between 1989 and 2008 (Fig. 3.9).

RUC and Slab simulations and ECA&D data share 75% of heat waves days. The number of overlapping heat waves days with ECA&D is 71 for the RUC simulation and 70 for the SLab simulations. However, the heat wave days which are not together in the RUC and SLab simulations and the ECA&D data still correspond to very hot days ($>90^{th}$ quantile). Over the 1989-2008 period, 2003 and 2006 are the warmest summers in terms of number of heat wave days and temperature anomaly magnitude. The specific case of the summer 2003 heat wave is now taken as an example of typical, even though exceptional, Western European heat wave. The summer 2003 heat wave simulated with the RUC and SLab LSMs is associated by a nearly identical 500-hPa geopotential height anomaly (less than 0.4% difference) corresponding to a strong anticyclonic anomaly over northern Europe, similar to the summer blocking situation of *Cassou et al.* (2005); *Stéfanon et al.* (2012a) (not shown). The spatial pattern of the 500-hPa geopotential height

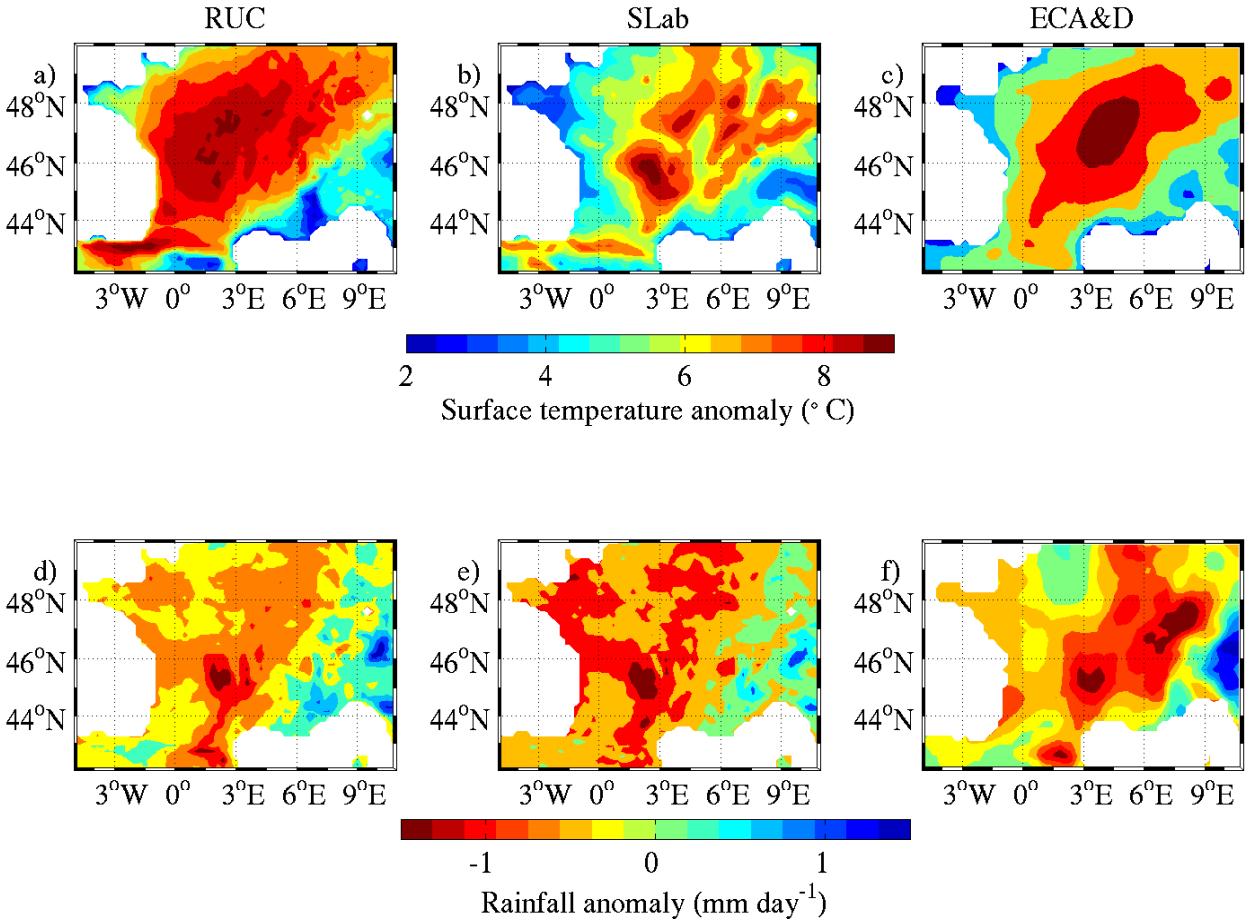

Figure 3.10: Summer temperature (upper row; panels a, b, c) and precipitation (lower row; panels d, e, f) anomalies with respect to the climatology (1989-2008) for the summer 2003 heat wave from the RUC simulation (left column, panels a, d), the SLab simulation (middle column, panels b, e) and the ECA&D data (right column, panels c, f).

anomaly is strongly correlated to that of the temperature anomaly (*Stéfanon et al.*, 2012a). Figure 3.10 shows the temperature anomaly with respect to the climatology. It is centered mostly over North Western France and has a magnitude of about 8-9°C in the RUC simulation and ECA&D data. It is on average 5-6°C in the Slab simulation with a peak over the Massif Central reaching 8°C. The meso-scale spatial variability of the temperature anomaly is more pronounced in the SLab simulation. In the two simulations, the temperature anomaly decreases near the Atlantic and Mediterranean coasts.

Western European heat waves are also often correlated with a persistent precipitation deficit (*Vautard et al.*, 2007; *Stéfanon et al.*, 2012a). The year 2003 was a very dry year, even though interrupted intermittently by local and intense heavy rainfall producing floods (*Christensen and Christensen*, 2003; *Fink et al.*, 2004). Figure 3.10 compares the precipitation deficit of 2003 as reproduced by the RUC and SLab simulations and from the ECA&D data. The overall deficit is accurately simulated, despite discrepancies visible around the mountainous regions. The two simulations display low positive anomalies over the Western Alps (>-0.5 mm day^{-1}) instead of high negative values (<-1.0 mm day^{-1}). The patterns

of RUC and SLab simulations are fairly similar. The RUC simulation displays a more severe rainfall deficit of about -0.07 mm day^{-1} with respect to the SLab simulation. The patterns of the temperature and rainfall anomalies of the summer 2003 heat wave displayed in Fig. 3.10 are very similar to most other heat wave situations occurring in France.

In conclusion, the RUC simulation accurately reproduces the summer daily maximum temperature with respect to the ECA&D data. The SLab simulation includes an LSM in which the soil moisture availability is set to wintertime values preventing the simulation of droughts. The comparison between the SLab simulation and the RUC simulation and ECA&D data thus shows evidence of a cold bias of about -4°C suggesting a strong control of the surface temperature by the soil moisture content. The variability of the temperature anomaly is less affected by soil moisture (-1°C with respect to RUC simulation and ECA&D data) since it is strongly controlled by the synoptic atmospheric circulation. However, this difference can be attributed to soil/atmosphere interaction, the impact of which displays a pronounced spatial meso-scale variability (strong impact over the plains and lower impact over the mountains). Finally, despite the major difference of the treatment of soil moisture in the two LSMs and its consequence on soil/atmosphere interactions, the hottest days referred as heat wave days (temperature anomaly exceeding the 95^{th} quantile), occur nearly simultaneously in the two simulations in good agreement with the ECA&D observations, but with a lower temperature anomaly in the SLab simulations. In the next sections, we conduct a through analysis of the difference between the RUC and SLab simulations to better understand the dynamical processes controlling the soil moisture/temperature feedbacks and their contribution to the temperature anomaly associated with the heat waves.

3.2.3 Sensitivity analysis

The sensitivity analysis is performed on the days classified as heat wave days in both RUC and SLab simulations. It includes 77 days among which the two consecutive heat waves of June and August 2003 (*Schär et al.*, 2004; *Stéfanon et al.*, 2012b). All the following figures in this section are displayed at 1200 UTC.

By construction of the sensitivity experiment, the RUC and Slab simulations do not treat soil moisture in a similar way. In order to compare the two simulations, the soil moisture availability is computed from the RUC simulation and is given by:

$$M = \frac{\gamma}{\triangle Bo}$$

where $\gamma = (C_p P) / (0.622 L_v)$ is the psychrometric constant with P the atmospheric surface pressure, L_v latent heat of water vaporization and C_p the specific heat of air at constant pressure. For $P = 1000$ hPa $\gamma = 0.643$ hPa K $^{-1}$. The quantity $\triangle$ is the slope of tangent to the coexistence curve (Clausius-Clapeyron equation) and Bo is the Bowen ratio, i.e. the ratio of sensible to latent heat fluxes. Figure 3.11 shows the spatial pattern of soil moisture availability for the RUC and SLab simulation. One can first note the very high values prescribed in the SLab model as a function of the land use. Most of the domain (80%) consists of dry croplands and pastures with a soil moisture availability equal to 60%. The remaining 20% are distributed between the deciduous broadleaf forest (8.5%) with values of soil moisture availability reaching 80% and 10 others classes. Among the remaining classes is the urban land use. The city of Paris can be identified as the isolated dot in the North of the domain with a value of soil moisture availability lower than 10%.

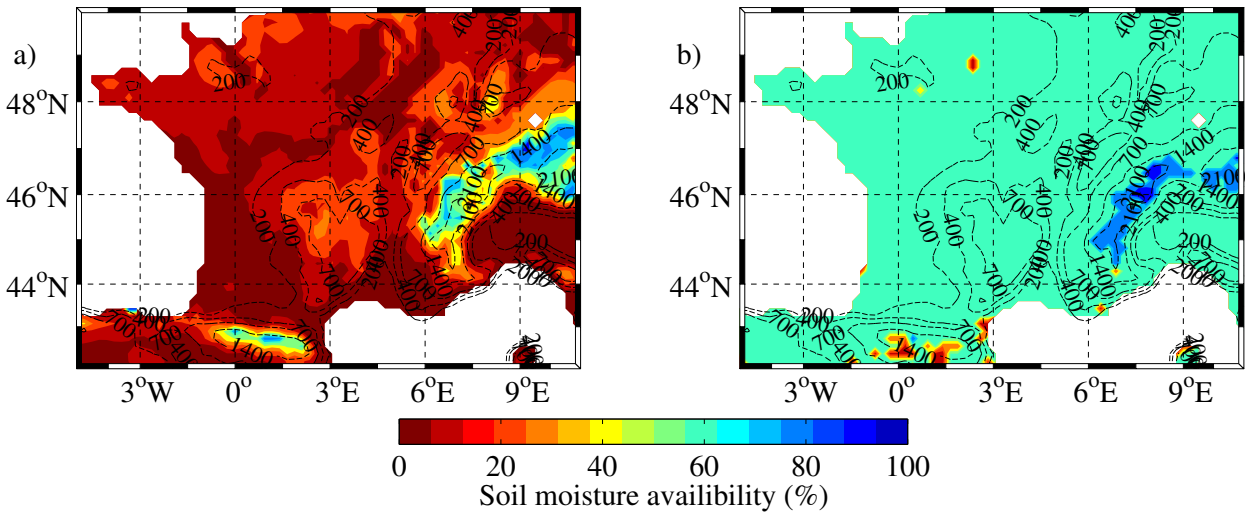

Figure 3.11: Soil moisture availability during the heat waves days computed from the RUC simulation outputs (a) and prescribed in the SLab simulation (b). Dashed lines indicate the topography elevation.

Comparatively, the RUC simulation generates much lower values of soil moisture availability in the plains (5-10%) with a much larger meso-scale spatial variability. This is directly caused by rainfall deficit preceding and during the heat waves generating significant soil moisture deficit (*Vautard et al.*, 2007; *Stéfanon et al.*, 2012a,b). The RUC simulation can thus be considered as a dry run whereas the SLab simulation can be considered as a wet run. However, in the mountains, the difference between the RUC and SLab simulations is smaller (30% over the Massif Central and 60-70% over the Alps and the Pyrénées). The land use is dominated by forests having deep roots attenuating the effect of soil moisture deficit in the uppermost soil layers (*Stéfanon et al.*, 2012b).

Such differences affect the energy budget at the surface. Figure 3.12 displays the Bowen ratio *Bo* for the RUC and SLab simulations. In the RUC simulation, high Bowen ratio values (> 5) are associated with very dry conditions in the flat plains of Southern France (South of 46°N latitude). North of 46°N latitude, the Bowen ratio still displays high values reaching on average 2. Bowen ratio values exceeding 2 refer to areas where evaporation is limited by soil moisture. Bowen ratio decreases with altitude downto to 0.5, which marks a shift towards an evapotranspiration regime limited by the incident solar energy. In the SLab simulation, the Bowen ratio is very low. Except in very local spots, it hardly exceeds 0.5-0.6. Over the Alps, it peaks locally at about 0.8 which is larger than the Bowen ratio from the RUC simulation. However, averaging over the Alpine region, the Bowen ratio is 0.65 in the SLab simulation and 0.97 in the RUC simulation. By construction, the surface conditions in the SLab simulation are always in the surface energy limited regime (*Seneviratne et al.*, 2010).

The *Bo* ratio is an integrated parameter combining sensible and latent heat fluxes used to describe the type of heat transfer (sensible heat and latent heat) over a moist surface. Figure 3.13 details the patterns of latent and sensible heat flux terms. It displays the difference of latent heat flux during the heat waves between the RUC and SLab simulations. The surface latent heat fluxes are much weaker in the RUC simulation, especially in South Western France and along the Mediterranean coast where the difference can reach -300 W m^{-2}. The difference between the two simulations weakens with altitude.

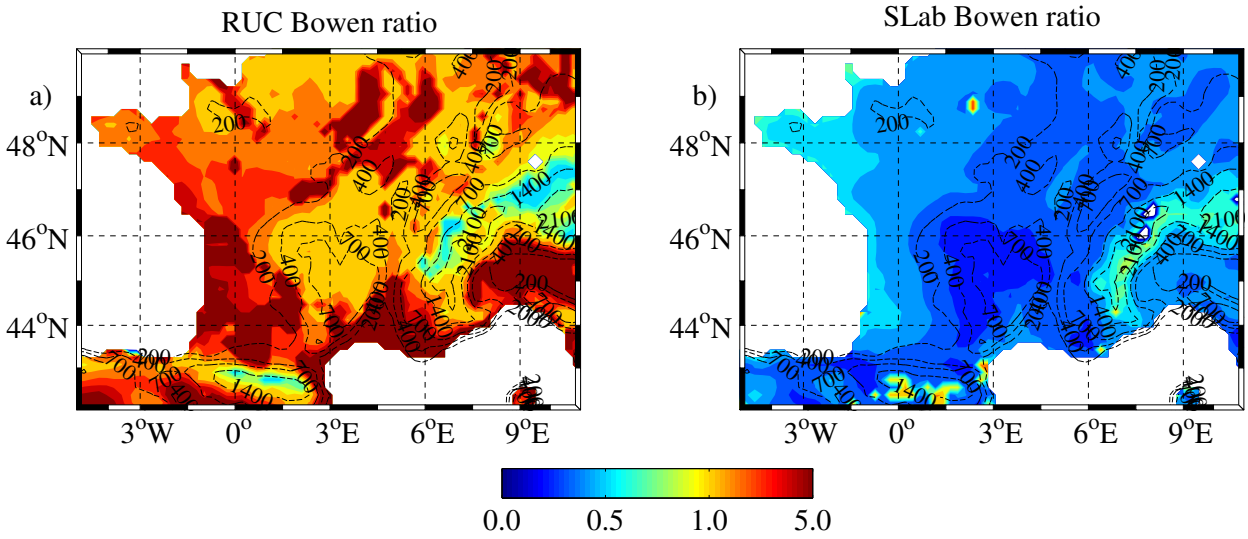

Figure 3.12: Bowen ratio for RUC and SLab averaged over heat waves days in 1989-2008. Dashed lines are height of topography.

Over the Massif Central, the difference decreases downto -100 W m^{-2}. It can even be higher in the RUC simulations at high altitude in the Alps and the Pyrénées with value reaching +100 W m^{-2}. These results are consistent with the difference between the soil moisture availability patterns in Fig. 3.11.

An indirect effect of such differences in the RUC and SLab simulations is the production of a larger amount of clouds over the Alps and the Pyrénées. Figure 3.13c shows the difference of downward solar radiation between the RUC and SLab simulations. The strongest differences are found over the Alps and the Pyrénées with about -100 W m^{-2} difference between the RUC and SLab simulations, reaching locally -250 W m^{-2}. Over moderate elevation mountains (Massif Central and Vosges), there is a slight negative difference of about -30 W m^{-2}. Elsewhere the differences are lower that 10 W m^{-2} in absolute value which is not statistically significant. Figure 3.13d shows the difference of accumulated rainfall between the RUC and SLab simulations during the heat waves. The pattern is very similar to that of the latent heat flux or downward solar radiation differences. The RUC simulation produces more rainfall (about 70 mm over the 77 heat wave days) than the SLab simulation over the most elevated peaks of the Pyrénées and the Alps. The difference can be as high as 300 mm over the 77 heat wave days. The difference tends to zero over the plains and is slightly negative near the Atlantic and Mediterranean coasts. The analysis of the diurnal cycle of rainfall averaged over the domain (not shown) shows that during heat waves, hourly rainfall rate is 1.18 larger in the RUC simulation than in the SLab simulation. The precipitation are mostly convective, the large scale precipitation representing less than 10% of the total amount in both simulations. In the RUC simulation, the precipitation peak occurs between 1500 and 1800 UTC whereas in the SLab simulation precipitations are shorter and their maximum is reached around 1800 UTC. With respect to climatological summer rainfall, the precipitation amount during heat waves is 2.5 lower in the two simulations. It has been shown that regarding precipitation, model results depend on the parameterization of convection. However, it has been shown that KF scheme gives results similar to those produced by cloud resolving model (*Bechtold et al.*, 2001; *Guichard et al.*, 2004; *Hohenegger et al.*, 2009).

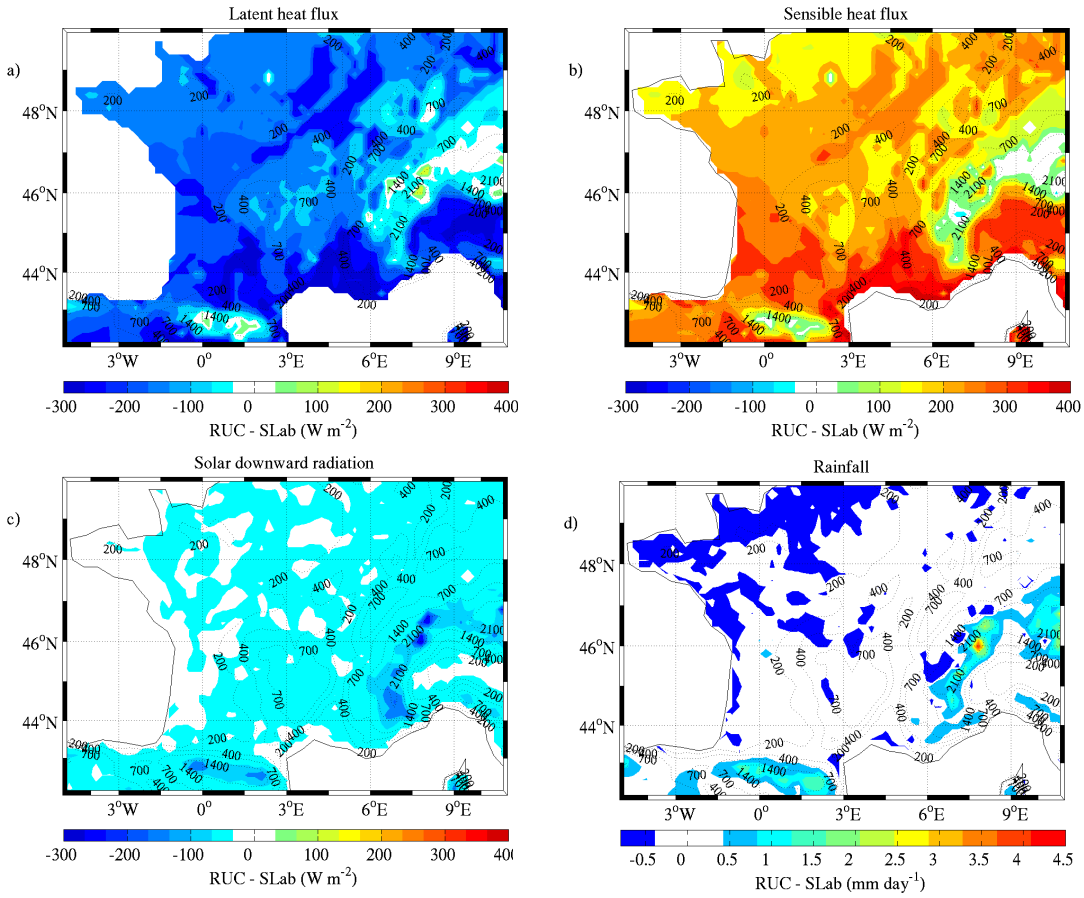

Figure 3.13: Difference of surface latent (a) and sensible (b), downward solar radiation (c) and accumulated rainfall averaged over the heat wave days of the 1989-2008 period between the RUC and SLab simulations. Dashed lines indicate the topography elevation.

Soil moisture availability in the two simulations thus strongly controls latent heat fluxes, as well as cloud formation and precipitation initiation. This feedback loop affects the transfer of sensible heat to the atmosphere and so the near surface temperature. In order to quantify the contribution of soil moisture availability on the heat wave temperature anomaly we compute index I_{SMTF} (SMTF standing for soil moisture-temperature feedback) defined as:

$$I_{SMTF} = 100 \times \frac{\triangle T_{RUC} - \triangle T_{Slab}}{\triangle T_{Slab}}$$

where $\triangle T_{RUC}$ and $\triangle T_{Slab}$ are the heat wave temperature anomalies from the RUC and SLab simulations, respectively. Physically, $\triangle T_{Slab}$ is mainly driven by the synoptic conditions, the effect of soil moisture deficit being absent, whereas $\triangle T_{RUC}$ includes the impact of synoptic conditions and soil moisture effects. I_{SMTF} can be seen as the fraction of the heat wave temperature anomaly that can be attributed to soil moisture-temperature feedbacks. Figure 3.14 displays the spatial pattern of I_{SMTF}. In Western France, I_{SMTF} reaches values around 70% which corresponds to a temperature anomaly warmer by about 3.5°C

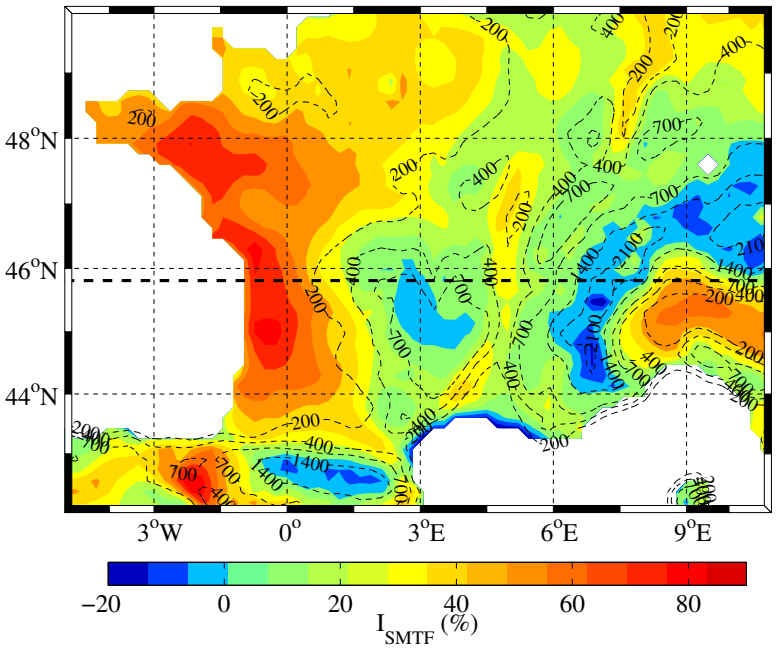

Figure 3.14: Index I_{SMTF} quantifying the contribution of soil moisture availability on the heat wave temperature anomaly. Dashed lines are height of topography. The thick dashed line indicates the cross section at 45.8°N analyzed in section 3.2.4. Thin dashed lines indicate the topography elevation.

in the RUC simulation with respect to the SLab simulation. I_{SMTF} decreases eastwards. Averaging North of the mountains, I_{SMTF} is about 30-40% which is consistent with the results of *Fischer et al.* (2007b). However, the specific case of mountains and Mediterranean coast must be investigated in detail. Indeed, in these regions I_{SMTF} takes negative values and can be as low as -20%, meaning that the SLab simulation which can be considered as a wet run amplifies locally the temperature anomaly of the heat waves. Such pattern is robust and has been found for all simulated heat waves.

There is thus evidence of significant differences at meso-scale of the soil moisture-temperature feedbacks. The following section aims at understanding the underlying meso-scale processes producing diff

3.2.4 Analysis of meso-scale dynamical processes

Locally, near surface temperature is intimately linked to the surface energy budget and the repartition between latent and sensible heat fluxes. This repartition depends on the soil-moisture precipitation feedback, which is mainly controlled by local convective processes as discussed in the previous section. Regionally, the complex nature of the terrain (inland surface heterogeneities, land/sea contrast, elevated orography) induces meso-scale circulations as slope wind, sea breeze and valley wind which can enhance locally vertical motion by wind convergence and also transport moisture from moist areas (e.g. Mediterranean Sea, Atlantic Ocean) to dry convective zones.

Figure 3.15 displays the planetary boundary layer (PBL) depth at 1500 UTC averaged over the heat waves days. It is computed in the boundary layer scheme as the height where a critical Richardson number is reached (*Noh et al.*, 2003). The PBL depth over the sea is similar between the RUC and SLab

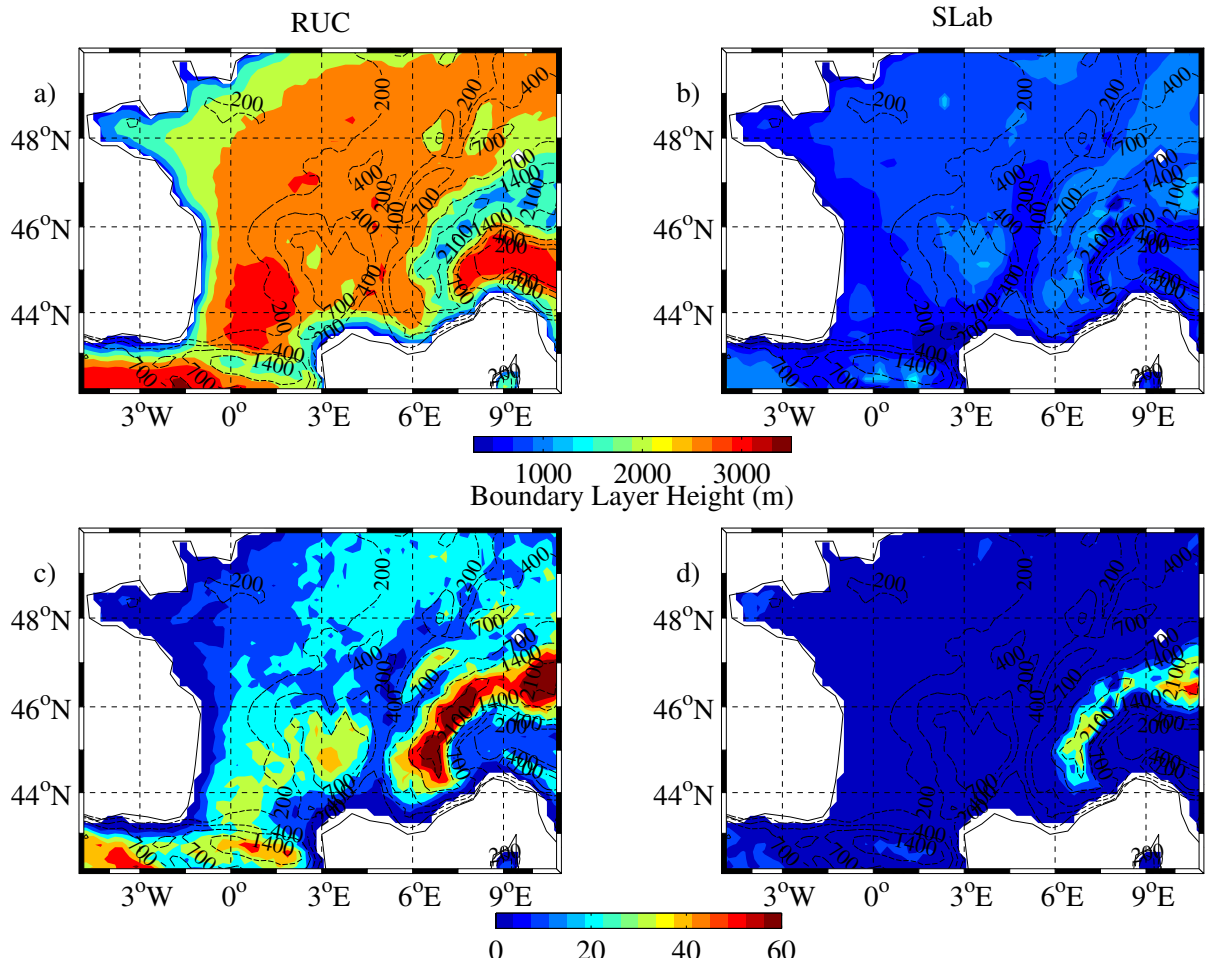

Figure 3.15: Planetary boundary layer depth (a-b) and exceedance rate (%) of the level of free convection at the boundary layer top (c-d) at 1500 UTC, averaged over all heat waves days for the RUC (right column; panels a and c) and SLab (left column; panels b and d) simulations. Dashed lines indicate the topography elevation.

simulations since air-interactions are identically computed in the two simulations with a prescribed sea-surface temperature. In the SLab simulation, the boundary layer depth remains low almost everywhere and hardly reaches 1000 m. It slightly increases over the mountains and very locally can reach 1500 m. At few locations in the Alps, the boundary layer can be deeper in the SLab simulation than in the RUC simulation. However, generally, the boundary layer is much deeper in the RUC simulation. It is on average 2200 m in the plains where surface sensible heat fluxes are also much larger than in the SLab simulation (Fig. 3.13b). Values ranging between 1200 and 1800 m are found in the coastal regions and over the Alps. The highest values are up to 2800 m in South-Western France, the Rhône Valley and the Po valley, also consistent with larger sensible heat flux (i.e. +350 W m^{-2}; see Fig. 3.13b).

The level of free convection (LFC) computed at 1500 UTC is a relevant diagnostics to analyze the mechanisms triggering convective precipitation. Figure 3.15 represents the exceedance rate of the LFC at the PBL top. Except over the Alps where it is on average 35%, the probability that the PBL is higher

than the LFC is zero in the SLab simulation. In the RUC simulation, the highest rate (60%) are found over the Alps and the Pyrénées. Moderate elevation have a lower rate of about 35% as over the Massif Central and over Jura and Vosges, in Eastern France. The rate is 10-20% over the plains. The correlation between the exceedance rate pattern and rainfall occurrence is 0.6 and 0.46 over the Alps and the Massif Central, respectively. Over the plains, there is no significant correlation between the exceedance rate pattern and rainfall occurrence. In the RUC simulation, moist static energy is lower than in the SLab simulation but the larger sensible heat fluxes at the surface cause thermal instability in the boundary layer and enhanced vertical motion. Despite large moist static energy in the SLab simulation which lowers the LCL and favors convection initiation, the stably stratified boundary layer inhibits vertical motion and PBL development so the PBL top hardly reaches the LCL. Indeed, inspection of the convective available potential energy (CAPE) and convection inhibition (CIN) (not shown) indicates that the SLab simulation has more potential for convection than the RUC simulation. CAPE values are large in the SLab simulation, especially in plain area as the Po valley and in South-Western France with 1500 J Kg^{-1}. It decreases with elevation downto 200 J Kg^{-1} over the Alps. Conversely in the RUC simulation, the CAPE is lower. The highest values are found over 1500 m height (450 J Kg^{-1}) and in Western France (300 J Kg^{-1}). In these regions, CAPE values in the SLab simulation are lower than in the RUC simulation. Elsewhere, sunny weather and moist surface of the SLab simulation provide heat and moisture to the atmosphere that contribute to increased moist static energy and potential for convection activity. However, higher CIN and higher stability in the SLab simulation prevent the rising of air parcel, except in high elevation where the CIN is close to zero. In the RUC simulation, CIN remains low everywhere with values lower than 10 J Kg^{-1}, except over coastal areas. For a more thorough analysis of the dynamics over the mountains, Fig. 3.16 displays the cross section at 45.8°N (Fig. 3.6b) of relative humidity and vertical velocity with superimposed isentropes at 1500 UTC averaged over all heat wave days for the RUC and SLab simulations. The cross section goes through all major mountains from west to east. Near saturated air masses with relative humidity exceeding 80% can be seen over the mountains at about 650 hPa (i.e. 3.6 km height) in the RUC simulation. Such pattern is not simulated in the SLab simulation. High relative humidity is confined within the boundary layer in the SLab simulation where it reaches 50% West of the Alps and 70% in the Po valley in Italy. In the RUC simulation, the relative humidity in the boundary layer never exceeds 20-30%.

In the SLab simulation, no convection is triggered above terrain of moderate elevation. The isentropes show a cold and stratified atmospheric boundary layer, preventing any convective motion. Over the Alps, vertical motion is simulated but with speed lower than 5 cm s^{-1}. From the shape of the isentropes, this is not due to unstable boundary layer stratification but to upslope winds (i.e. also referred as anabatic winds). Indeed, during daytime the mountain flank warms up faster than its environment enhancing local baroclinicity of the atmosphere and so anabatic winds. This baroclinicity can be maintained all day long because of the influence of the sea-breeze blowing from the Mediterranean coast (*Bastin and Drobinski*, 2005). This latter process will be investigated in-depth further in the text. Conversely, in the RUC simulation, Fig. 3.16 displays convective motion over mountains with updrafts exceeding 6-8 cm s^{-1} with a maximum of 12 cm s^{-1} on the Eastern flank of the Alps. The boundary layer is much warmer and well mixed in the RUC simulation, favoring the production of thermals reaching 700 hPa. Alternating with updrafts, downdrafts entrain tropospheric air within the boundary layer. In addition to local convection,

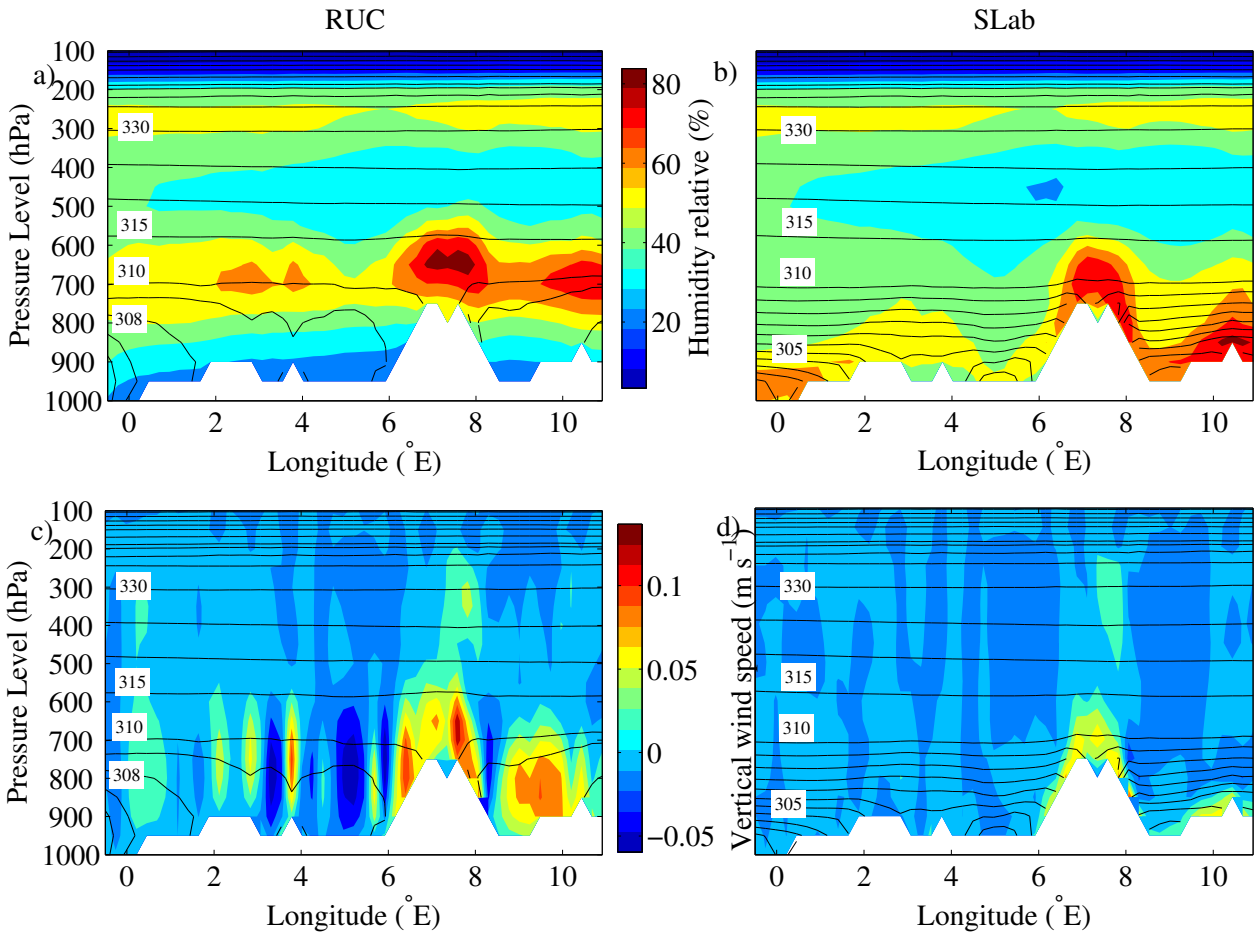

Figure 3.16: Cross section at 45.8°N (Fig. 3.6b) of relative humidity (a, b) and vertical velocity (c, d) in color with superimposed isentropes (isocontours) at 1500 UTC averaged over all heat wave days for the RUC (right column; panels a, c) and SLab (left column; panels b, d) simulations.

anabatic winds reinforce vertical motion (*Bastin and Drobinski*, 2006). Such regional circulation between the Alps and the foreland is also referred as "Alpine pumping" and is known to increase convection and precipitation over the Alps (*Raymond and Wilkening*, 1980; *Weissmann et al.*, 2005).

As shown in Figs. 3.14 and 3.15, the soil moisture/temperature feedback over the mountains and near the Mediterranean coast is less intuitive than over plains in the RUC simulation since the temperature anomaly of the heat wave is attenuated in the dry RUC simulation. For a more in-depth analysis of the underlying processes, we analyze the diurnal cycle of surface energy budget at specific locations in the Alps (A-B), the Massif central (C), in the plain (D) and near the Mediterranean coast at the exit of the Rhône valley (E) (see locations in Fig. 3.6b). Figure 3.17 shows the mean diurnal cycle of the difference of the solar downward radiation, latent and sensible heat fluxes between the RUC and SLab simulations. The difference of temperature anomaly is also represented.

In the mountains (locations A, B and C), Fig. 3.17 shows that the temperature anomaly is much larger in the RUC simulation at night than in the SLab simulation. This difference decreases significantly during the day and reaches a minimum at the warmest period of the day (between 1500 and 1800 UTC).

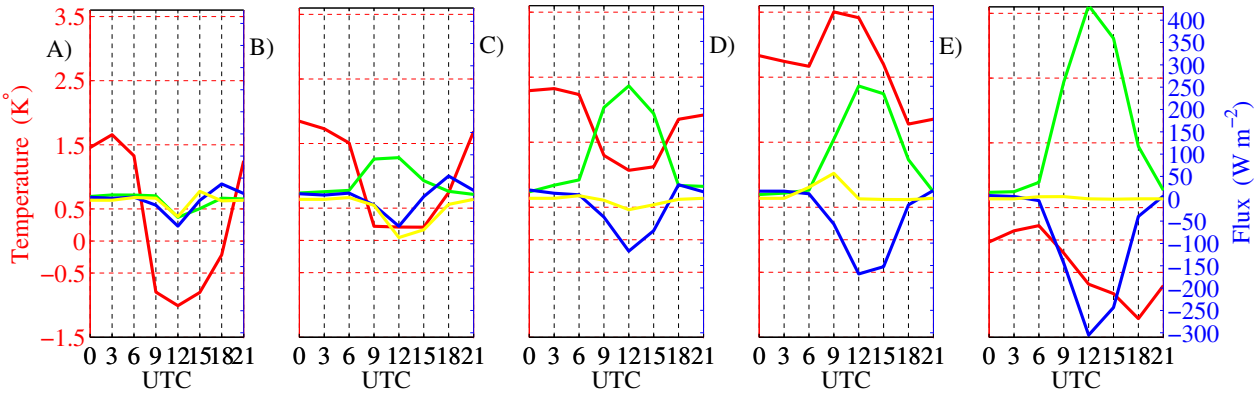

Figure 3.17: Diurnal cycle of the difference of temperature anomaly (red), sensible (green) and latent (blue) heat fluxes and shortwave radiation (yellow) between the RUC and SLab simulations at locations A, B, C, D and E indicated in Fig. 3.6b.

This evolution is similar at all mountain locations. However the difference of temperature anomaly shifts towards negative values with increasing altitude. At location A at 2500 m height, the difference of temperature anomaly between the RUC and SLab simulations can reach -1°C at 1200 UTC. The minimum of temperature anomaly reaches +0.2°C and +1°C at 1200 UTC at locations B and C at 2100 m and 750 m height, respectively. At these locations, latent heat flux becomes larger in the RUC simulation than in the SLab simulation by 50 W m s^{-2} at about 1800 UTC, during the rainfall events. This is associated with an important decrease of solar downward radiation (-86 W m s^{-2} at location B) which starts at 1200 UTC since the clouds form earlier in the RUC simulations. Sites D and E are located at about 50 m height.

The evolution of the difference of temperature anomaly between the RUC and SLab simulations at locations D and E differs form that at mountain sites. At location D, in the plain west of the Atlantic coast, the difference of temperature anomaly difference is the highest and can reach +3.5°C around 1200 UTC when the difference of downward solar radiation between the RUC and SLab simulations is also the highest. The downward solar radiation is more important during the early morning in the RUC simulation, owing to the presence of fog in the SLab simulation. This lack of cloudiness and the deficit in soil moisture (Fig. 3.11) contributes to the build up of daytime heat at 1200 UTC, with an increase of sensible heat flux at the expense of latent heat flux. Contrary to the situation in mountains, the difference of temperature anomaly is minimum at night and increases during the day as expected in the case of positive soil moisture/temperature feedback.

Near the Mediterranean coast, the evolution of the different terms of the energy budget differs from all previous cases. The difference of temperature anomaly remains negative and decreases from 0900 UTC downto -1.2°C at 1800 UTC. It corresponds to the hour of maximum sea breeze in this region (*Bastin et al.*, 2005; *Bastin and Drobinski*, 2006; *Drobinski et al.*, 2006). Figure 3.18 displays the time series of the vertical profiles of the horizontal wind speed and direction averaged over the heat wave days at location E from RUC and SLab simulations.

This figure gives a detailed insight on the alternation between the land and sea breeze. It show that the land breeze blows from the northeast until about 0900 UTC and sifts by 180° at the onset of the

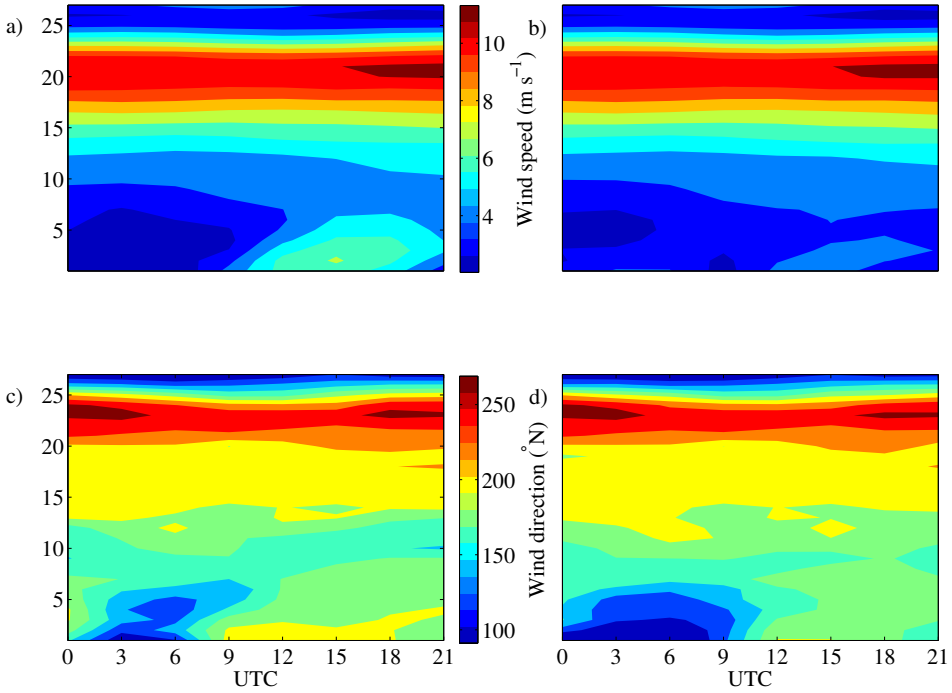

Figure 3.18: Time vs height plot of wind speed (a, b) and wind direction (c, d) from the RUC (a,c) and SLab (b, d) simulations at location E (Fig. 3.6b).

sea-breeze which blows from the southwest. The wind intensity increases at sunrise with the onset of the sea-breeze from about 3-4 m s^{-1} to about 7 m s^{-1} in the RUC simulation and 4.5 m s^{-1} in the SLab simulation. The vertical extent of the sea breeze is about 850 hPa, i.e. about 1500 m. The sea breeze is induced by a temperature gradient between the air temperature above sea and land. In the RUC and SLab simulations, the SST is prescribed from ERA-Interim reanalysis. The larger temperature from the RUC simulation above land due to reduced evaporation and enhanced sensible heat flux with respect to the SLab simulation, strengthens this sea-breeze circulation in all the coastal areas. This is illustrated in Fig. 3.19 which shows the near-surface horizontal wind averaged over the heat wave days from RUC and SLab simulations.

Advection of moist and cool marine air by the sea-breeze cools down the atmospheric boundary layer over land over a horizontal range that can exceeds 150 km inland as shown in Fig. 3.19 (*Drobinski et al.*, 2006; *Drobinski and Dubos*, 2009). This confirms the impact of the sea-breeze on the generation of slope winds over the mountains surrounding the Mediterranean coast, as discussed earlier. Locations D and E are thus both under the influence of the sea-breeze circulation, however the differences of temperature anomaly have no similar evolution (Fig. 3.17). On the Mediterranean coast, soil moisture deficit is not significantly different during heat waves and during climatological summer in the RUC simulation. Boundary layer heating by enhanced surface heat fluxes is thus only slightly stronger during heat waves. Since the SST is prescribed from ERA-Interim reanalysis, the land/sea thermal contrast is not significantly different during heat waves. By construction, it is the same for the SLab simulation. Advection of cool marine air by the sea-breeze is thus stronger in the RUC simulation than in the SLab simulation. The temperature anomaly is thus of lower magnitude in the RUC simulation because of large

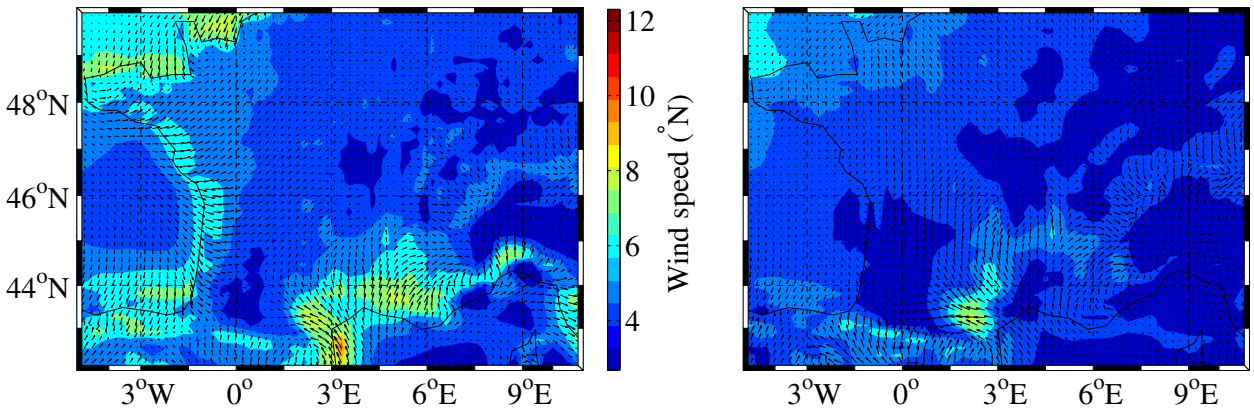

Figure 3.19: Near-surface horizontal wind vectors averaged over all heat wave days at 1800 UTC from the RUC (a) and SLab (b) simulations. The color shading indicates the wind speed in in m s^{-1}.

damping effect by cool air advection with respect to marginal heating by enhanced surface sensible heat fluxes. At location D, the situation is slightly different. The summer 2003 heat wave is associated in this region with significant soil moisture reduction with respect to the climatology. This effect is reproduced with the RUC simulation but not with the SLab simulation. The RUC simulation thus produces much higher surface sensible great fluxes and warming during heat waves, which is not the case in the SLab simulation. As for the Mediterranean area, sea-breeze also tends to damp the warming effect over land but this contribution is not dominant. Soil moisture deficit during heat waves thus contributes positively to the temperature anomaly in Western France (Fig. 3.14). I_{SMTF} reaches 70-80% in the plain and slightly decreases downto 60% at the coast due to the influence of the sea-breeze.

3.2.5 Conclusions

This section investigates the impact of soil moisture-temperature feedback at meso-scale on the heat waves occurring over France between 1989 and 2008 using two simulations with the two different land-surface models. The first land-surface model resolves the hydrology and is able to simulate the summer dryness, whereas the second land-surface model prescribes a constant and high soil moisture availability which prevents the simulation of sol moisture deficit. A sensitivity analysis highlights different soil moisture-temperature responses (i) over low-elevation plains, (ii) over mountains and (iii) over coastal regions.

The sensitivity analysis showed that in the plains, the dominant process is the conversion of solar radiation into heat at the expense of evapotranspiration, which is very low due to the soil-moisture deficit. Soil moisture deficit induces less evapotranspiration, a drier atmosphere and therefore less clouds and precipitations. A positive feedback loop is thus created. This well-known process is found to contribute to 40% of the temperature anomaly in Eastern France to 80% of the temperature anomaly in Western France during the heat wave. The remaining contribution comes from the presence of a persisting synoptic blocking situation over the region of the heat wave.

Over the mountains surrounding the Mediterranean coast (Pyrénées, Massif Central and the Alps), enhanced heat fluxes over dry soil reinforce slope winds, i.e. also called thermal "pumping" which contribute to reinforce by convergence vertical motion over the mountain slope, also partly generated

locally by thermal convection. Despite the reduced moist static energy during heat waves, strong updrafts can lift moist air parcels to their level of free convection enabling deep convection and precipitation. This effect is nearly non existing in case of high soil moisture availability. In this latter case, despite high moist static energy, strong thermal stratification prevents vertical motion. Temperature thus rises because of the favorable synoptic conditions but without counterbalancing cooling effect by precipitation. Over mountains, dry soil is indirectly associated to lower heat wave temperature anomaly.

Finally, in coastal regions, the land/sea thermal contrast is enhanced in case of dry soil, strengthening sea-breeze circulation and moist cool marine air advection. This damps the magnitude of the heat wave temperature anomaly over a narrow land band near the Atlantic coast and even decreases by 20% the temperature anomaly near the Mediterranean coast.

This section thus shows evidence the significant impact of meso-scale dynamics on the soil moisture-temperature feedback. These meso-scale circulations like slope winds and sea-breeze can modulate the well-known local soil-atmosphere feedback by the generation of wind convergence and the advection of moist air from remote regions (e.g. oceans). Wind convergence induced by meso-scale circulations contributes to enhance vertical motion and facilitate convection initiation and precipitation which in turn cool down the atmosphere. Moisture advection can increase moist static energy over convective dry areas also favoring deep convection and precipitation.

We took advantage of 20-years simulations performed at 20 km resolution to extract the robust meso-scale dynamical processes associated with heat waves and not focus on case sensitive processes associated with one particular event. The main drawback of this approach is that despite the fairly "high" resolution, the simulations still rely on convection parameterization. We took care to use convection parameterization that produce results which are consistent with results from cloud resolving models. Nevertheless, uncertainties remain associated with the representation of the hydrological cycle and the land atmosphere coupling in regional climate models. Especially, soil moisture conditions depend considerably on the level of sophistication of the land-surface model. Most land-surface models simulate the exchange of surface water and energy fluxes at the soil-atmosphere interface and do not account for water redistribution by rivers, vegetation phenology and dynamics. Accounting for these processes can modify by few tens of percent the temperature anomaly of a heat wave, impact water exchange between the soil and the atmosphere and modulate the life cycle of droughts and heat waves. Such affects are investigated in chapter 4, which however focus on particular events : the 2003 summer heat waves.

Chapter 4

Impact of vegetation on the 2003 summer heat waves

This chapter is a synthesis of two articles : (*Stéfanon et al.*, 2012b) and *Stéfanon et al.* (2012d) submitted to the Journal of Geophysical Research and in preparation respectively.

4.1 Effects of interactive vegetation phenology

The previous section assessed the impact of soil moisture-temperature feedback on the heat waves, using LSMs which neglect vegetation phenology and dynamics. In this section, we aim to investigate the role of interactive vegetation phenology on the temperature anomaly of the 2003 summer heat wave, and quantify its potential impact with a two-way land atmosphere coupling into a high-resolution grid (15 km). Phenology is explicitly resolved by the LSM, thus LAI has a seasonnal cycle related to atmospheric and soil moisture states. The high-resolution sheds light on the spatial structure of regional vegetation and its link with temperature extremes. The domain simulation is shown in Fig. 4.1 and remains over France, which matches with the Western Europe pattern of section 3.1 and the domain simulation of section 3.2. It is situated in a transitional area compounded of several ecosystems, and between different types of terrain (plain, mountain). Moreover it is on both sides of 46°N parallel, marking the sharp transitional zone between the Mediterranean dry and the European continental climate (*Köppen*, 1936; *Peel et al.*, 2007).

We use the Weather Research and Forecasting atmospheric model coupled with the ORCHIDEE land-surface model as described in section 2.2. A comparison of simulations performed with prescribed and dynamically evolving phenology is carried out.

This section is organized as follows. Subsection 4.1.1 includes a description of summer 2003 in literature. The methodology and simulations carried out are presented in subsection 4.1.2 with a brief validation. The results of the different simulations are compared, and the differences and similarities are exposed in subsection 4.1.4. The processes involved are presented in subsection 3.2.4 showing the connections of temperature, soil moisture, evapotranspiration (ETP) and vegetation. Conclusion is given subsection 4.1.6.

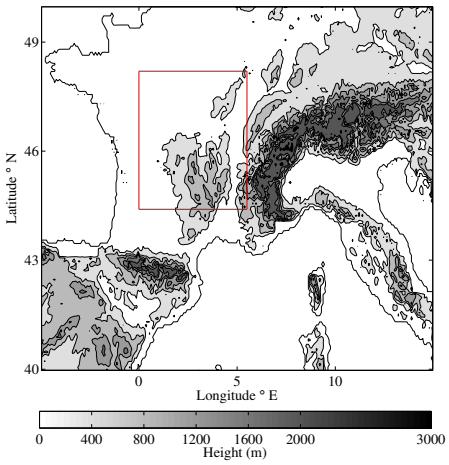

Figure 4.1: The red box indicates the integration domain of the MORCE simulations performed to analyse the effect of atmosphere/vegetation feedbacks on the 2003 summer temperature anomaly. The grey shading indicates the height of the model orography.

4.1.1 The 2003 summer heat wave: a review

2003 was one of the warmest years recorded during the period of world-wide instrumental records (beginning in approximately 1880) (*Levinson and Waple*, 2004). At the continental - European - scale two distinct periods of exceptional heat occurred during the summer season, the first in the second week of June and the second in the first two weeks of August. The latter was by far the warmest since it coincided with the normal peak of summer temperatures. *Schär et al.* (2004) highlighted that these months had respectively a temperature offset of 5.3 and 4.1 standard deviations from the mean summer temperature over 1864–2003 in Switzerland. Figure 4.1.1 shows the 2003 summer anomaly with respect to the climatology (1950–2009) of the daily maximum surface temperature from the European Climate Assessment & Data (ECA&D; (*Tank et al.*, 2002)) averaged over the area 44°N–48°N, 0°E–6°E (see Fig. 4.1). It allows the accurate identification of the beginning and end of the two heat waves. The first heat-wave starts on June, 8 and ends on June, 16. August sequence is the most intense and longest with 12 days exceeding the 99^{th} percentile of the 1950–2009 period. This heat-wave starts on August, 2 and ends on August, 16.

The 500 hPa geopotential height anomaly and daily maximum surface temperature anomaly from the ERA-Interim reanalysis of the European Center for Medium-range Weather Forecast (ECMWF) (*Dee et al.*, 2011; *Simons et al.*, 2007) averaged over the two heat waves periods are shown in Fig. 4.3. Geopotential anomalies exhibits two anticyclonic conditions. The surface temperature anomaly displays maximum values as high as 12°C. In June, the geopotential height anomaly features deep troughs over Eastern Atlantic and Western Russia, and ridges over Europe and central Russia. In August, the synoptic situation can be viewed as the positive phase of the summer North Atlantic Oscillation (NAO) (*Hurrell et al.*, 2003). This episode was associated with an abnormal positive phase of the summer Northern Annular Mode (NAM). This planetary circulation linked European and Canadian warm temperature with Japanese cold weather (*Ogi et al.*, 2005). In terms of weather regimes (*Cassou et al.*, 2005) the patterns of Fig. 4.3 are also named Atlantic low and blocking, respectively. These regimes were shown to be associated with extreme warm days. *Cassou et al.* (2005) showed that these regimes can be favored

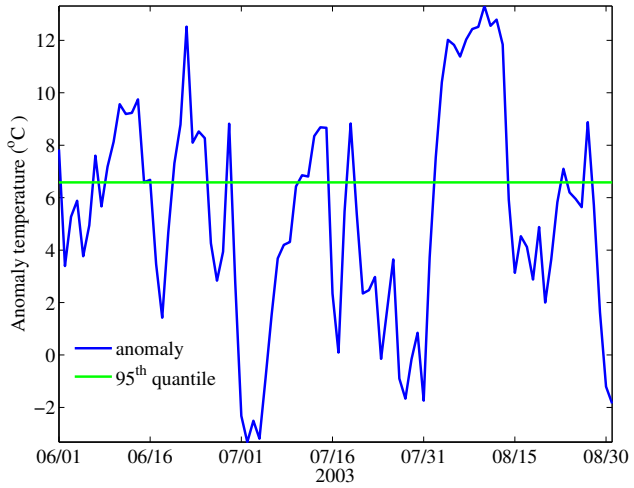

Figure 4.2: Time series of the 2003 temperature anomaly with respect to the climatology of the daily maximum surface temperature from the European Climate Assessment & Data (ECA&D) averaged over the area 44°N–48°N, 0°E–6°E (see Fig.4.1, red box). The temperature anomaly is indicated in blue and the 95th summer quantile is indicated in green, with respect to 1950–2009 climatology.

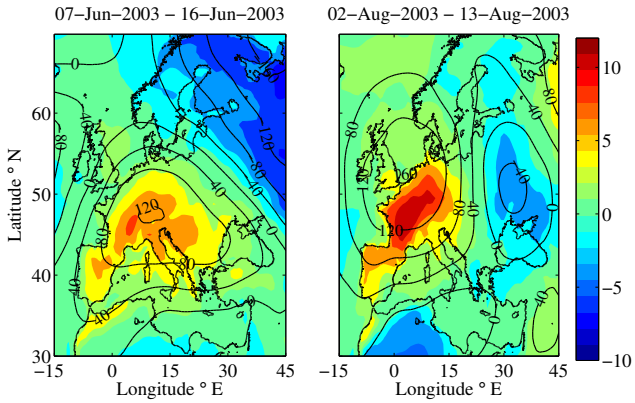

Figure 4.3: Daily maximum temperature anomaly (color shading; in deg K) and 500-hPa geopotential height anomaly (isolines) averaged over the two heat waves periods of June 2003 (a) and August 2003.

by large scale remote forcing such as the Tropical Atlantic SST.

The year 2003 was also a very dry year with a persistent precipitation deficit, interrupted intermittently by local and intense heavy rainfall producing floods (*Christensen and Christensen*, 2003). The precipitation deficit was exceptional in February and March 2003 and lasted until the end of summer 2003 (*Fink et al.*, 2004). Precipitation deficit affected local soil moisture, enhancing sensible heat flux and surface temperature (*Vautard et al.*, 2007; *Fischer et al.*, 2007b). Several model output quantified the contribution of soil moisture deficit to the summer 2003 temperature anomaly to about 40% (*Ferranti and Viterbo*, 2006; *Fischer et al.*, 2007b). Dryness is also assessed by satellite imagery. *van der Velde et al.* (2011) analysed the relationship between soil moisture (from the Advanced microwave Scanning radiometer AMSR-E) and crop yield at regional scale in France. They found that wheat loss was the strongest in 2003 (with respect to the 2002–2007 period), significantly correlated with the soil moisture

anomaly. *Loew et al.* (2009) use products from ENVISAT to investigate soil dynamics and reveals also a negative soil moisture anomaly since March 2003.

Others studies using several remote sensing products have been performed to investigate the heatwave and drought impact on vegetation in 2003. Satellite are better suited to estimate vegetation parameters at global and regional scale. They measure the land surface temperature which is strongly related to air temperature, but also depends of latent heat flux. Thus it depicts a better estimation of vegetation condition. *Ciais et al.* (2005) show the biosphere reaction in 2003 compared to 2000–2002 with the fraction of absorbed photosynthetically active radiation (FAPAR). The decrease in foliar surface is especially strong in the center of France with 30% less radiation. *Reichstein et al.* (2007) confirm this result and find that 2003 was exceptionally low in terms of vegetation activity, compared to the 20 previous years. *Jolly et al.* (2005) highlight also a global shortening of the growing season length in plain area, in 2003 with respect to the period 2000–2004. *Zaitchik et al.* (2006) performs an analysis of normalized difference vegetation index (NDVI), sensible heat flux and temperature from several satellite images. They point out that the temperature anomaly were greater for croplands than for forested lands during the heat waves.

4.1.2 Experimental design

The model used in this study is the MORCE *Model of the Regional Coupled Earth system* platform (*Drobinski et al.*, 2012). It has been designed to investigate the role of coupled processes on the regional climate of particularly vulnerable areas. It has been used in the *Hydrological cycle in the Mediterranean experiment* (HyMex) (*Drobinski et al.*, 2009, 2010) and the *Coordinated Downscaling Experiment* (CORDEX) of the World Climate Research Program (WCRP) (*Giorgi et al.*, 2009; *Ruti et al.*, 2012).

The atmospheric model

The atmospheric model of the MORCE platform is the Weather Research and Forecasting (WRF) model of the National Center for Atmospheric Research (NCAR) (see chapter 2for further details). In this experiment the domain covers part of continental France with a horizontal resolution of 15km (see red box in Fig.4.1). It has 28 sigma-levels in the vertical. Initial and lateral conditions are from the ERA-Interim reanalysis of ECMWF (*Dee et al.*, 2011; *Simons et al.*, 2007) provided every 6 hours with a 0.75° resolution. A complete set of physics parameterizations is used with the WRF Single-Moment 3-class microphysical scheme (*Hong et al.*, 2004), the new Kain-Fritsch convection scheme (*Kain*, 2004), the Yonsei University (YSU) planetary boundary layer (PBL) scheme (*Noh et al.*, 2003) and a parameterization based on the similarity theory (*Monin and Obukhov*, 1954) for the turbulent fluxes. The radiative scheme is based on the Rapid Radiative Transfer Model (RRTM) (*Mlawer et al.*, 1997) and the *Dudhia* (1989) parameterization for the longwave and shortwave radiation, respectively. Simulation domain is sufficiently small to produce strong control of the simulations by the boundary conditions and avoid unrealistic departures from the driving fields (*Omrani et al.*, 2012), thus no nudging is applied here.

The land surface model

In the MORCE plateform, the dynamical global vegetation model ORCHIDEE is implemented in the atmospheric module WRF. ORCHIDEE is based on three different modules (*Krinner et al.*, 2005).

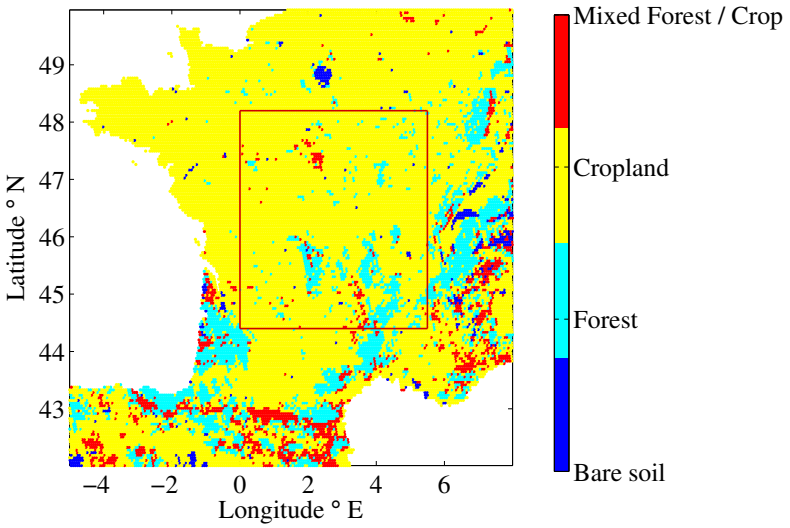

Figure 4.4: Vegetation distribution according to Olson vegetation map at 5' resolution. For the sake of clarity, vegetation types are deliberately grouped into 4 main categories : Bare soil, Forested areas, Cropland, and a mixture from the last two. The red box indicates the domain of the MORCE simulations.

SECHIBA, describes the fast processes such as the soil and energy water budget. The phenology and carbon dynamics of the terrestrial biosphere are simulated by the STOMATE module. Finally, the long-term processes, including vegetation dynamics, fire, sapling establishment, light competition, and tree mortality are simulated according to the global vegetation model LPJ (*Krinner et al.*, 2005) but are not used in the experiments designed herein (i.e. vegetation in our experimental set up is prescribed and set, once for all, at its present day distribution). The Choisnel scheme for hydrology is chosen.

The vegetation distribution is strongly dominated by croplands, present in 88% of the domain, whereas forest and mixed vegetation account for 10 and 2% respectively. Forest are located mainly in the Southern France and on mountain slopes whereas in Northern France they are very scattered (Fig.4.4).

4.1.3 Numerical experiments

Two simulations are performed driven by ERA-INTERIM for the years 2002 and 2003. Both uses ORCHIDEE as LSM with SECHIBA and STOMATE modules activated. It implies an identical computation of stomatal resistance with the same impact of atmospheric carbon. The first, called CTL, was conducted using a prescribed LAI. The effect of vegetation was thus limited to stomatal resistance only. The second simulation called MORCE, uses an explicitly calculated LAI. The prescribed LAI in CTL for 2003 is that of the year 2002 obtained with the MORCE simulation with interactive vegetation. Both simulations begin with the same initial state conditions for the soil state. This is computed by a 5 years spin up integration using the conditions of the year 2002 repeated five times with ORCHIDEE in offline mode. Atmospheric inputs for this spin up are provided by WRF simulation with the NOAH LSM.

The simulation domain covers most of France (Fig. 4.1) and includes the Massif Central bordering the Rhône Valley along its Eastern slope and the Aude valley along its Western slope. The differences between the MORCE and CTL simulations provide an estimate of the impact of vegetation dynamics on

the dynamics of the heat-waves. We analyse the response in terms of anomaly of temperature, surface heat flux, and vegetation parameters (LAI, gross primary production GPP).

Validation of temperature

Comparison of the CTL and MORCE simulations with observation has been carried out for surface temperature. We use the E-OBS 3.0 gridded dataset of the European Climate Assessment & Data (ECA&D) (*Tank et al.*, 2002) for maximum continental surface temperature and precipitation (*Haylock et al.*, 2008). During summer (June-July-August, i.e. JJA), WRF usually displays a warm bias for the mid-latitudes with respect to ECA&D. For instance with the rapid update cycle (RUC) LSM (*Smirnova et al.*, 1997, 2000) the bias is of approximately 3 or 4°C for the daily mean temperature (*Flaounas et al.*, 2012). The use of ORCHIDEE produces a lower bias up to 1.02 and 1.20°C on summer 2003 for MORCE and CTL, respectively. If we consider the daily maximum temperature over the same period, the bias reaches 0.06 and 0.1°C for MORCE and CTL, respectively. In the MORCE simulation, the bias increases from 0.19 to 0.61°C between the June and August heat-wave periods, respectively. Conversely, it decreases in the CTL simulation from 0.75 to 0.22°C. The temperature difference between the two simulations and the ECA&D dataset during these heat waves is displayed in Fig. 4.5. Patterns are very similar between the two simulations and the ECA&D dataset. The non significant bias below 0.66°C is white shaded. The MORCE simulations displays a larger variability than the CTL simulation but it is closer to the ECA&D data over larger areas.

4.1.4 Simulation results

Figure 4.6 displays the differences between MORCE and CTL simulations at 1500 UTC (warmest period of the day) for surface temperature and latent heat flux (equal to the evapotranspiration from plant and bare soil, multiplied by the water specific latent heat vaporization) averaged over the periods of heat waves as defined in section 4.1.1. It shows important temperature differences between the two simulations. In June 2003, the MORCE simulation is colder than the CTL simulation. On average the temperature difference is -0.55°C and can reach -2.5°C in Northern France. In South-Western France, the difference between the two simulations is not significant. The situation in August is reversed with respect to the situation in June. The MORCE simulation is on average 0.39°C warmer and exhibits temperatures up to 2.2°C higher in the Western area with respect to the CTL simulation. Only the high elevation areas in the Massif Central are colder by about 1.3°C with respect to the CTL simulation. The most remarkable feature is the very strong anti-correlation of about -0.7 between the temperature anomaly and the latent heat flux anomaly patterns. In June 2003, the most negative temperature anomaly (about -1 to -1.5°C) corresponds to a positive anomaly of latent heat flux of about +100 W m^{-2} (Figs. 4.6a and b). In August 2003, the positive temperature anomaly (about +1 to +1.5°C) corresponds to a negative anomaly of latent heat flux of about -100 W m^{-2} (Figs. 4.6c and d).

Figure 4.7 displays similar diagnosis as Fig. 4.6 for sensible heat flux and solar net radiation. The sensible heat flux anomaly pattern is of opposite sign to the latent flux anomaly with at most 115 W m^{-2} difference. Regarding the solar flux, it is on average 660 and 690 W m^{-2}, for June and August, respectively. It displays very little difference between the MORCE and CTL runs for August, because of the absence of clouds in the two simulations, except along the mountain slopes where the MORCE

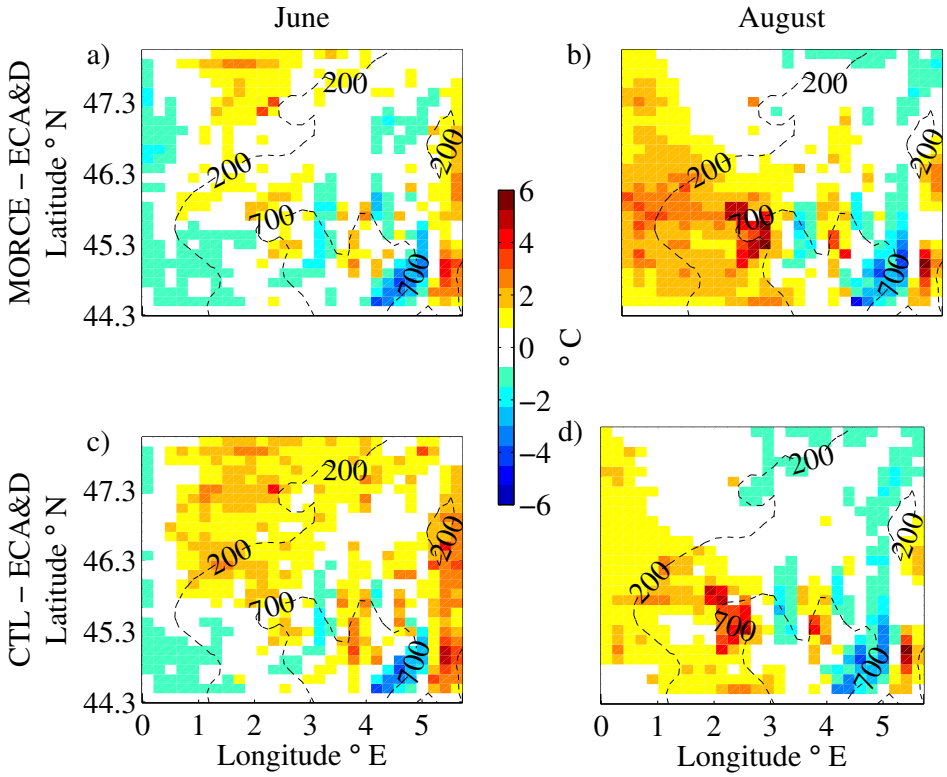

Figure 4.5: Difference in daily maximum surface temperature between the MORCE simulation minus the ECA&D gridded dataset (a-b), and CTL minus ECA&D gridded dataset (c-d). Left (right) panels correspond to June (August) heat wave. Dashed lines are height of topography.

simulations produces slightly less clouds. The difference is locally higher for June with a higher cloud cover in the MORCE simulations, consistently with the higher evapotranspiration. The difference can exceed 90 W m^{-2} in the center of the domain and is on average 10 W m^{-2} over an area in Central France representing 38% of the total domain size. A difference of 10 W m^{-2} in latent and sensible heat flux is found over an area representing 80 and 90% of the total domain, respectively. The spatial correlation between temperature and latent heat flux pattern (Figs. 4.6a and b) is 4.5 higher (in absolute value) than the correlation between temperature and net solar radiation pattern (Fig. 4.6a and Fig. 4.7a).

The difference of albedo between the MORCE and CTL simulations can be analyzed using the reflected (i.e. upward) short wave radiation (Fig. 4.8). The difference between the two simulations is low when averaged over domain, with 5.5 and 2.5 W m^{-2} in June and August, respectively. Thus the foliage development does not impact albedo on cropland area. Nevertheless along mountain slopes, where forest vegetation is dominant, it is up to 50 W m^{-2} and explains most of the difference in net solar radiation during August heat wave (Fig. 4.8).

Cutting the domain in four sub-domains of equal size delimited by the grey lines in Fig. 4.6 and 4.7, shows evidence of different responses to the effect of interactive vegetation (Fig.4.6 and 4.7). If the two Northernmost subdomains have similar behaviour, the two Southernmost subdomains display significantly different behaviours.In June, the MORCE simulation is colder than the CTL simulation

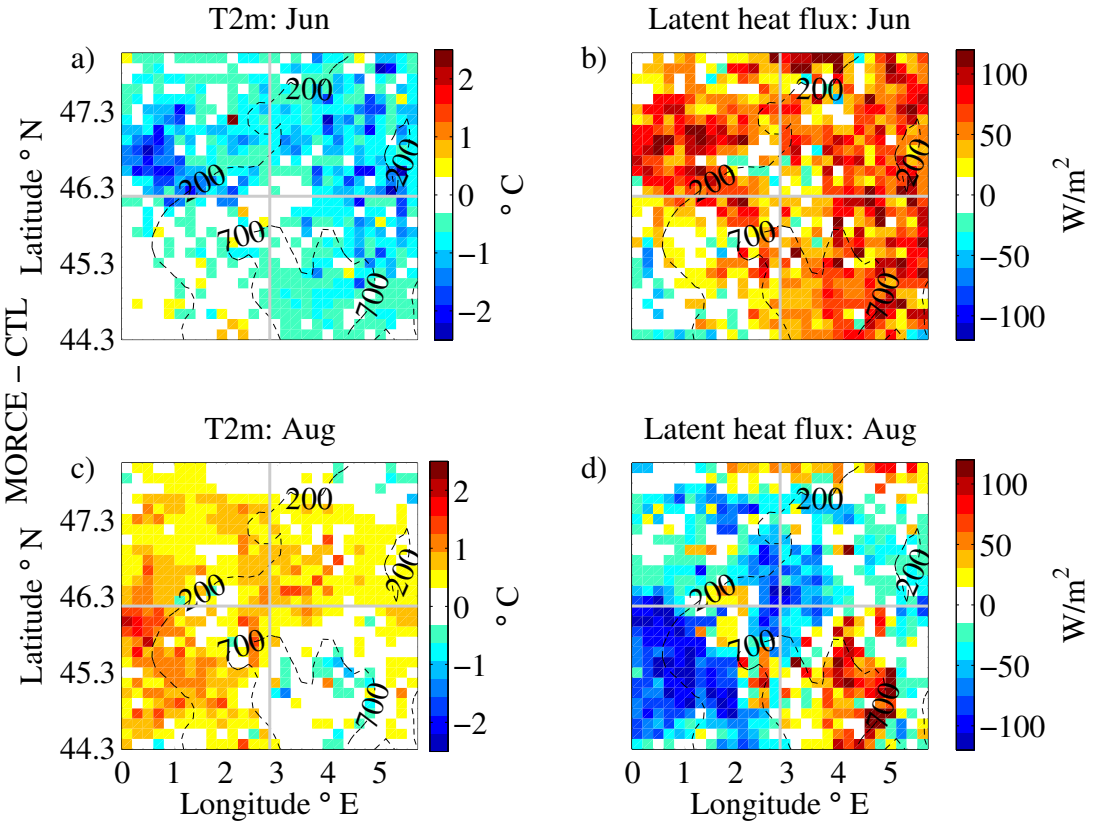

Figure 4.6: Difference between the MORCE and CTL simulations over the domain indicated by a red box in Fig.4.1 for the 2-m temperature (a-c), latent heat flux (b-d) at 1500 UTC averaged over the heat wave period in June 2003 (a-b) and August 2003 (c-d). Dashed lines are height of topography.

over Northern and South-Eastern France over Massif Central. The difference is not significant in South-Western France. In August, the MORCE simulation is warmer than the CTL simulation over Northern and South-Western France, whereas it is slightly colder over South-Eastern France. In the South-Eastern subdomain, the presence of the Massif Central controls part of the hydrological response with lower soil water stress and different vegetation types than over the rest of the domain (Fig. 4.4).

Figure 4.9 shows the time series of the daily average difference between MORCE and CTL simulations for surface temperature and evapotranspiration for the four subdomains.

From April to June, the afternoon evapotranspiration is about 40% higher in MORCE simulations which is equivalent to 1.2 mm day^{-1} additional water released in the atmosphere over the whole domain. In June, the MORCE excess of evapotranspiration with respect to the CTL run decreases until it reverses at the end of July just before the August heat wave. This behavior is found for all subdomains except the South Eastern sector. In the first half of August, during the heat wave, the evapotranspiration deficit in MORCE simulations reaches a peak of 1.89 mm day^{-1} in the South Western subdomain. The response in temperature excess is however similar to that simulated in the Northern subdomains (about +0.5°C). The link between evapotranspiration and boundary layer heating is thus more complex than a simple linear response. However, the temperature and evapotranspiration anomalies (MORCE-CTL) are

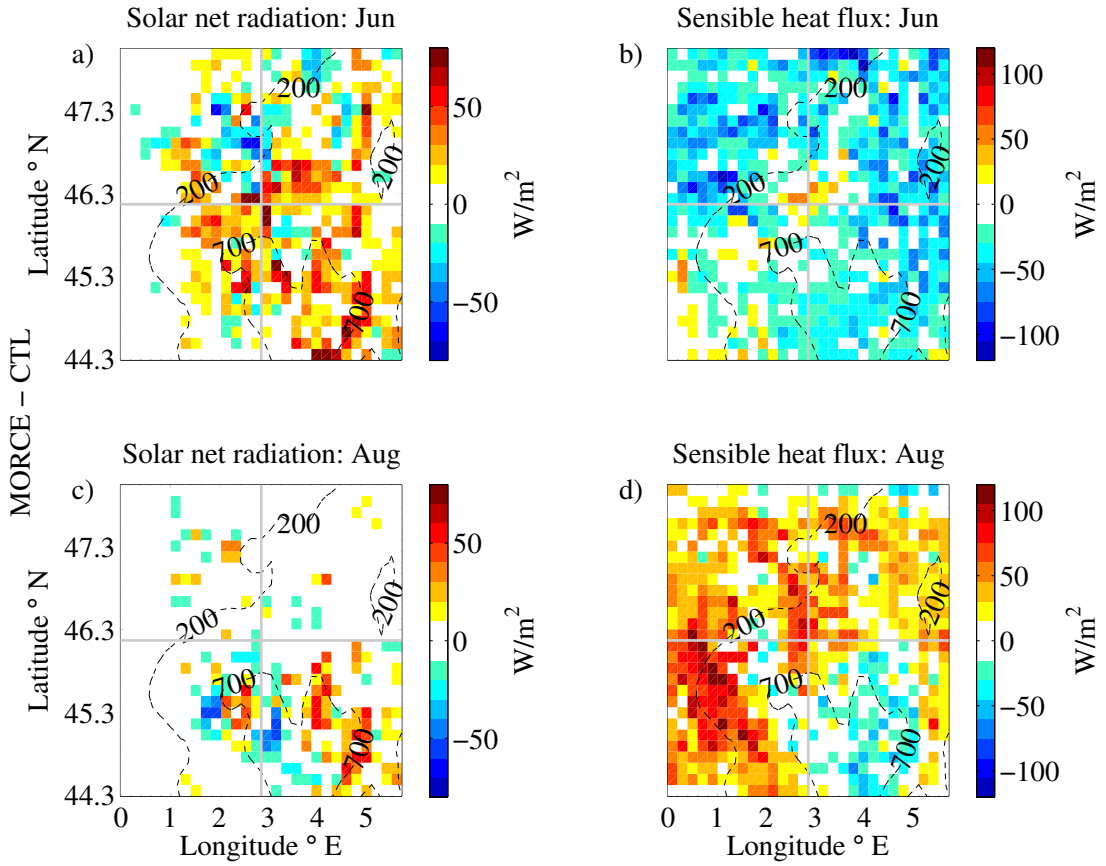

Figure 4.7: Similar as Fig.4.6 for the solar net radiation (a-c), sensible heat flux (b-d), in June 2003 (a-b) and August 2003 (c-d).

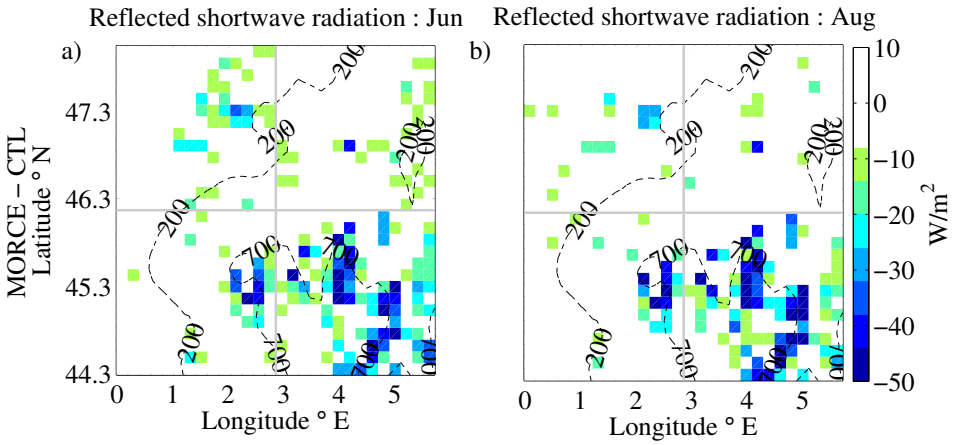

Figure 4.8: Similar as Fig. 4.6 for the reflected shortwave radiation by albedo in June 2003 (a) and August 2003 (c).

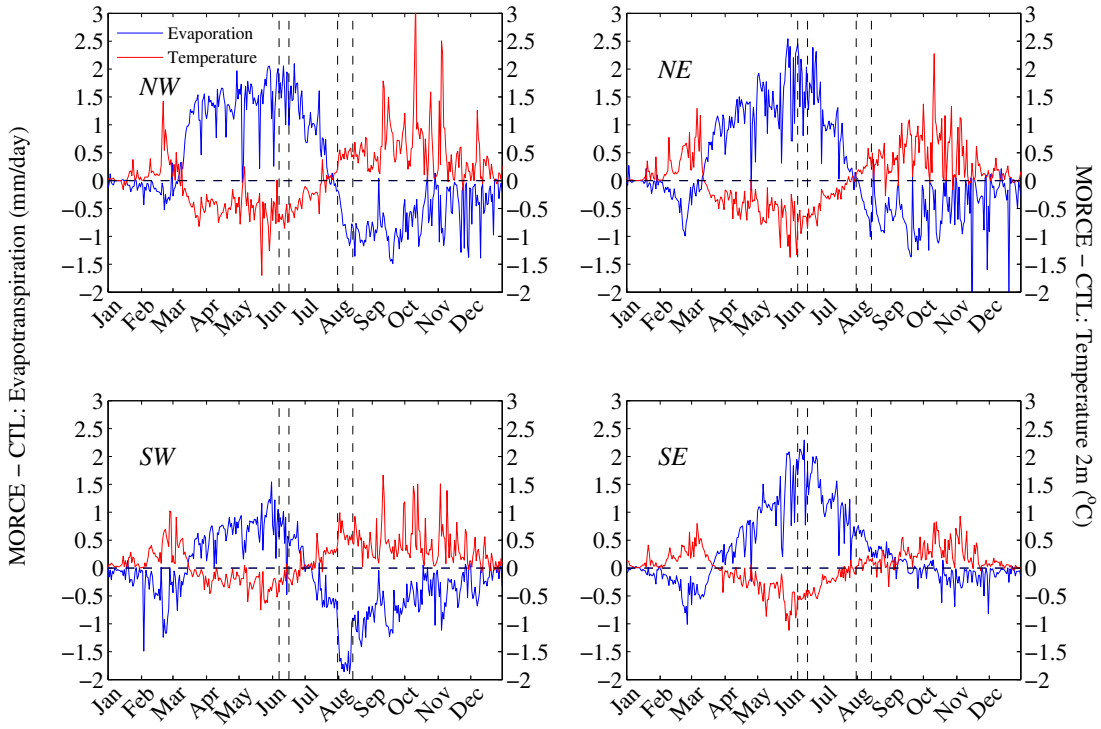

Figure 4.9: Difference between the MORCE and CTL simulations for the evapotranspiration (blue line) and surface temperature (red line) at 1500 UTC in the North Western subdomain (NW), the North Eastern subdomain (NE), the South Western subdomain (SW) and South Eastern subdomain (SE). Vertical dotted lines delimit the heat waves of June and August.

strongly negatively correlated reaching correlation coefficients ranging between -0.72 and -0.82 for the four subdomains.

4.1.5 Process analysis

In order to assess the impact of changing the prescribed vegetation to an interactive one, we give a special attention to three axes. First the soil moisture – precipitation is investigated (subsection 4.1.5) as *Beljaars et al.*, 1996; *Heck et al.*, 2001.Then follows a detailed analysis of plant phenology and its link with the hydrological cycle (subsection 4.1.5). Lastly a comparison of vegetation and atmosphere state with an overview of satellite observation is given (subsection 4.1.5).

The soil moisture – precipitation feedback

The main difference of evapotranspiration between the MORCE and CTL runs, for both high and low frequency variability, is due to agricultural grass PFT (AC3) transpiration up to 88%, as suggested by Figure 4.10. It displays the difference between the MORCE and CTL simulations for the daily average evapotranspiration in the four subdomains and for the various PFTs and bare soil. The residue mainly corresponds to interception loss and other PFT transpiration which are here negligible.

We find that a subsequent amount of water is evaporated in the MORCE simulation compared to

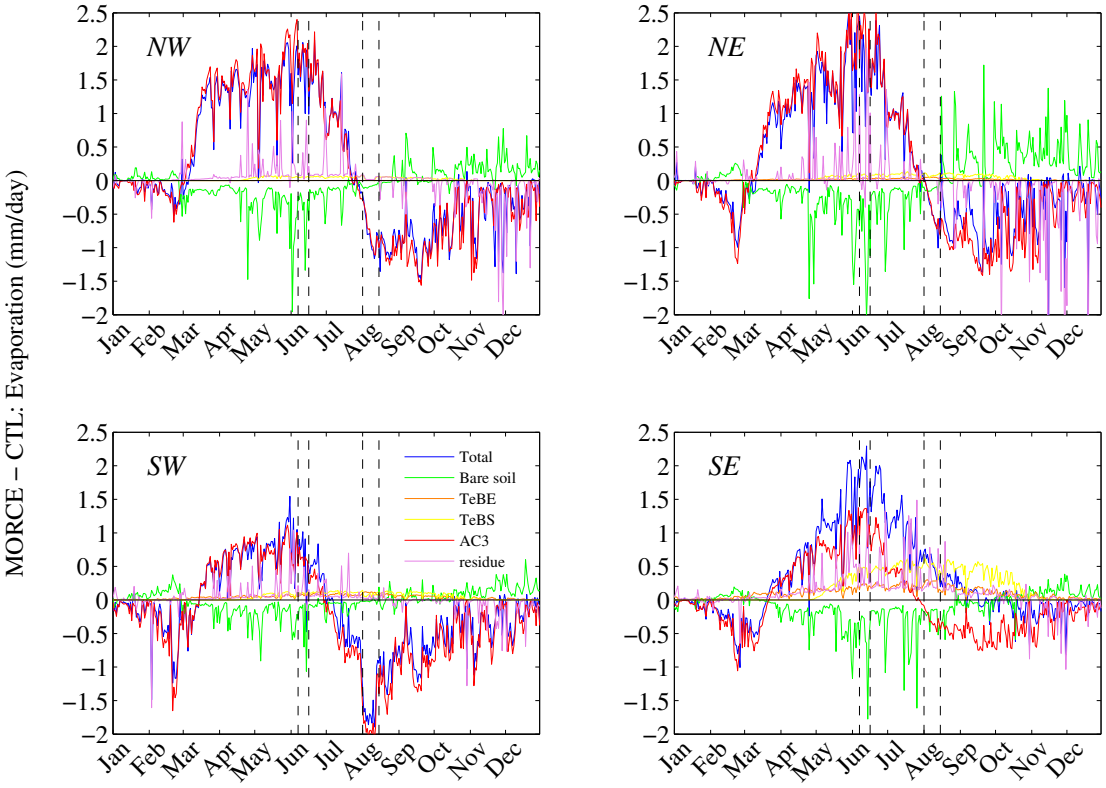

Figure 4.10: Difference between the MORCE and CTL simulations for the evapotranspiration in the North Western subdomain (NW), the North Eastern subdomain (NE), the South Western subdomain (SW) and South Eastern subdomain (SE) for the different PFTs (TBE in orange, TBS in yellow and AC3 in red), bare soil (green), the total (blue) and the residue (purple). Vertical dotted lines delimit the heat waves of June and August.

CTL. The additional water may remain in the atmosphere and induces a convective precipitation – soil moisture feedback. Indeed, a water fraction may be immediately recycled through precipitation, change the surface fluxes partition by moisturing the upper soil layers and eventually cool the near-surface atmosphere. In order to investigate a possible soil moisture-precipitation feedback, Fig. 4.11 displays the difference MORCE-CTL of cumulative evapotranspiration (red) and rainfall (blue) in 2003 for the four subdomain. It clearly shows a larger evapotranspiration than precipitation which has dried the soil since March in the MORCE simulation and induced by vegetation green up. Maximum of $P-ET$ occurs during July. This result suggests that this additional water vapor can only be recycled on the domain up to 15.4% (maximum P/ET). This is in good agreement with previous results. For instance over the Mediterranean coast, *Trenberth* (1999) has estimated to 12% the annual mean recycling, meaning that 12% of annual precipitation comes from evapotranspiration within the Mediterranean area.

We analyse further rainfall differences during summer (JJA). Convective and large scale rainfall are very similar in MORCE and CTL runs. The departure between cumulated rainfall and rainfall event (rainfall >0.5mm) during summer is low (close to zero) across the domain. Thus even if there are important differences of surface heat flux, they do not imply the direct onset of few convective rainfall. Although changes in evapotranspiration do not impact strongly local precipitation, it may induce rainfall

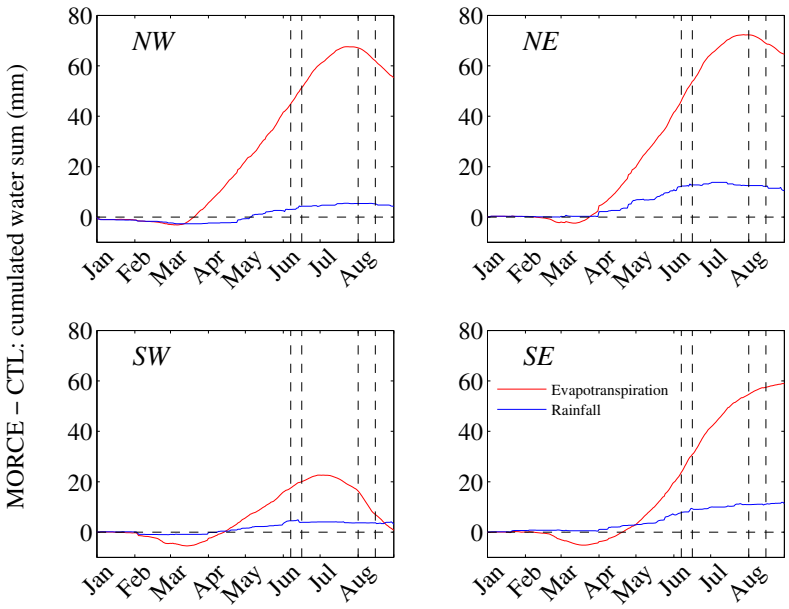

Figure 4.11: Evolution of the cumulative evapotranspiration (red) and rainfall (blue) in 2003 in the North Western subdomain (NW), the North Eastern subdomain (NE), the South Western subdomain (SW) and South Eastern subdomain (SE). Vertical dotted lines delimit the heat waves of June and August.

variations at larger scale outside the domain. In conclusion the evapotranspiration increase causes a slight positive feedback between the vegetation and the rainfall. However the rainfall enhancement only partially compensates the evapotranspiration increase, and therefore it increases the moisture divergence and the drying.

The role of phenology dynamics

The LAI and the gross primary production (GPP) are diagnostics of the vegetation condition at a given time. The LAI is a partial indicator of the ability of the vegetation to evaporate the water from the root zone soil. GPP is an indicator of the instantaneous activity of the plant, positively correlated with stomata opening and evapotranspiration.

Figure 4.12 displays similar analysis as Fig 4.6 but for LAI and GPP. In June, LAI is larger in the MORCE simulation +1.97 m^2m^{-2} on average over the whole domain). In detail, there are large areas of LAI excess in the MORCE simulation compared to the CTL simulation, especially in Northern and South-Eastern France. In these regions, surface temperature is lower in the MORCE simulation which is consistent with a more abundant vegetation and more latent heat flux (Fig. 4.6). Indeed, the correlation between the LAI anomaly pattern and the latent heat flux pattern is very high. As LAI and GPP are partly correlated, Figure 4.12b displays a GPP anomaly pattern similar to the LAI anomaly pattern of Fig. 4.12a, although there are small differences. However we would expect higher GPP and LAI values, especially in the center of the domain which receives more solar radiation in the MORCE simulation during this period (Fig. 4.7b).

In August, GPP is lower in the MORCE simulation by -1.1 gC day $m^{-1}m^{-2}$ with respect to the

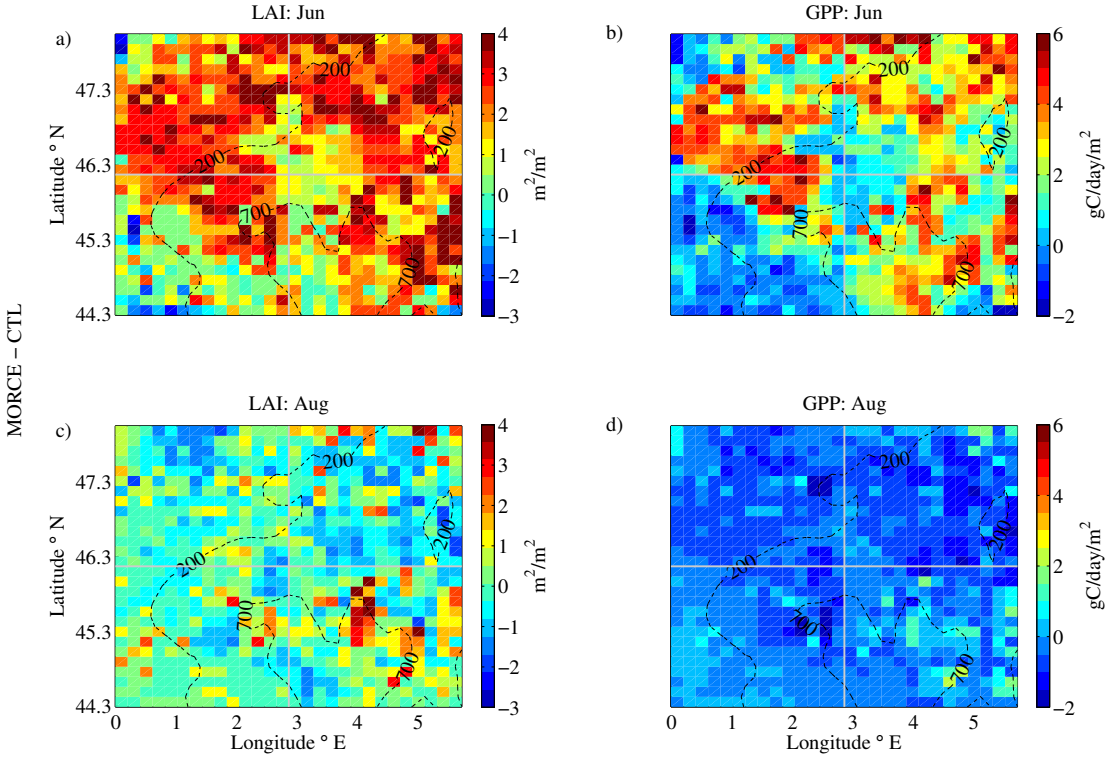

Figure 4.12: Similar as Fig.4.6 for the leaf area index (LAI) (a-c), the gross primary production (GPP) (b-d) in June 2003 (a-b) and August 2003 (c-d).

CTL simulation which corresponds to a decrease of 55% between June and August. The decrease is almost spatially uniform except in the South-Eastern region on the slopes of the Rhône Valley. A similar pattern is found for LAI, but with more contrast between the regions of higher and lower LAI reduction. Nevertheless the correlation between the LAI anomaly pattern and the latent heat flux pattern is there again high (0.45), but lower than in June (0.55). In contrast the correlation between GPP and latent heat flux is divided by 3 during the same period. This highlights the link between the vegetation and its foliar surface on the local surface energy budget and the hydrological cycle. In the South Western subdomain, the latent heat flux decreases strongly, while LAI and GPP remain nearly constant. However, in this case, the pattern of temperature anomaly corresponds to the pattern of soil water content anomaly, although the difference between the simulations is low (-3.75 kg m^{-2}) compared to the response of others subdomains (not shown). It can not explain differences in latent heat flux up to 100 W m^{-2}. One possible explanation is as the soil water content in this subdomain are low (178 kg m^{-2}), unattainable for the crops, the fall of the latent heat flux is due to a threshold effect of water stress. In the South Western domain the vegetation is mostly AC3 PFT (Fig. 4.4). During August in this subdomain, soil moisture stress for AC3 PFT is critical. It is equal to 0.09 in the MORCE simulation (it is 0.35 in the CTL simulation). Thus only few differences in soil water content leads to large water stress impact for the crops and confirms the presence of a threshold effect.

For a more thorough analysis, we now evaluate the evolution of the LAI anomaly (MORCE-CTL) by PFTs as well as the moisture stress anomaly for the four subdomains (Fig. 4.13). Budburst dates are

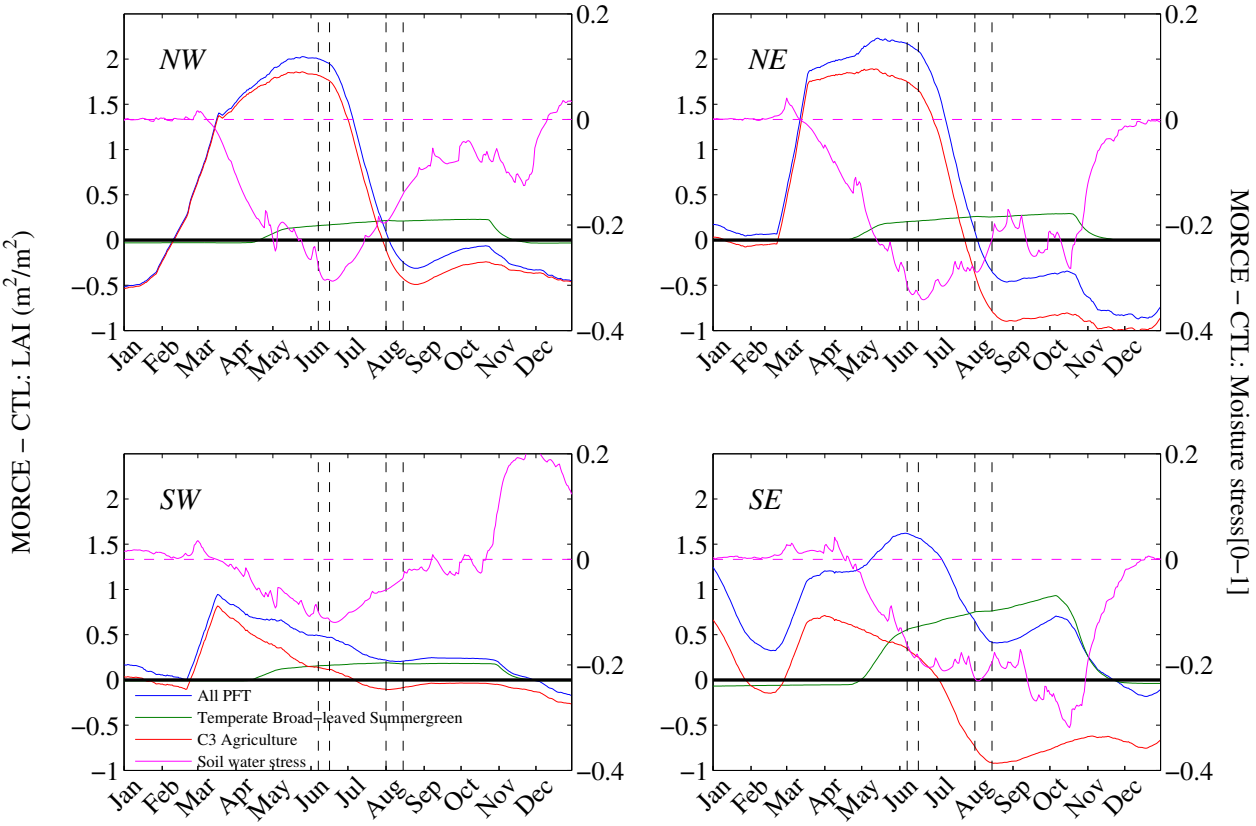

Figure 4.13: Evolution of the main PFT LAI anomaly (total in blue, TBE and TBS in green and AC3 in red) and water stress index anomaly (purple) in 2003 in the North Western subdomain (NW), the North Eastern subdomain (NE), the South Western subdomain (SW) and South Eastern subdomain (SE). Vertical dotted lines delimit the heat waves of June and August. Left vertical axis is LAI, the right vertical axis uses a different scale for the water stress.

synchronous in the MORCE and CTL simulations. The seasonal cycle is exacerbated in the MORCE simulation with 40% additional LAI during the growth phase. This is largely due to the agricultural vegetation (AC3). The temperate broadleaved summergreen (TBS) LAI has partially offset the early loss of crops in MORCE during the summer to the tune of +0.3 m^2m^{-2}. In the South Eastern subdomain the crops loss is fully compensated since the TBS LAI is more abundant and the offset is enhanced with almost +0.8 m^2m^{-2} additional LAI. TBS leaf onset and leaf shedding are simultaneous in the two simulations. The exceptional development of TBS in the MORCE simulation (3 times as large as in the CTL simulation) is owing to the sunny conditions and warm weather but also to TBS roots which are 8 times longer than that of AC3 which allow a better withstand to drought. The LAI begins to decline in June in the two simulations. In the MORCE simulation, the LAI declines 15 days earlier than in the CTL simulation. This decline is also much faster in the MORCE simulation. The LAI anomaly changes sign (i.e. the total vegetation becomes less abundant in the MORCE simulation than in the CTL simulation) just before August. Between the date of maximum LAI and 1 September 2003, the LAI drops from 5.4 to 1.5 m^2m^{-2} i.e. -71% in the MORCE simulation versus -49% in the CTL simulation (from 3.45 to 1.75 m^2m^{-2}).

If ORCHIDEE uses 13 PFTs in our simulation domain, more than 95% of the vegetation is represented by only three PFTs. Here, LAI variations are mainly caused by C3 crops. From April to June, agricultural C3 grass (AC3) represents 90% of the foliage surface against 65% during the heatwave, plus 20% and 10% for temperate broadleaved summergreen and evergreen (TBS and TBE), respectively. AC3 PFT evolution strongly depends on moisture availability and temperature. TBS is only function of springtime warmth for onset, computed as an accumulation of non-chilling days. Requirements for senescence are a negative temperature trend and a monthly temperature fall below a given threshold (*Krinner et al.*, 2005). TBE and evergreen vegetation are not affected by any of these parameters.

Figures 4.12 and 4.14 show evidence that the AC3 is the dominant PFT, accounting for 74% of total changes in LAI between MORCE and CTL. The others PFTs (Fig. 4.14c and d), TBS and TBE forest species are found in large part on the mountain slopes. During August the LAI anomaly between MORCE and CTL runs is mostly negative and in large part attributed to AC3 PFT. The positive LAI anomalies associated with forest PFTs (TBS and TBE) persist between the June and August heat waves. The positive anomaly even intensified in the South Eastern subdomain. Between June and August, LAI decreases by -1.83 m^2m^{-2} on average, corresponding to -1,88 m^2m^{-2} for AC3 PFT, counterbalanced by +0.073 m^2m^{-2} and +0.0011 m^2m^{-2} for TBS end TBE PFTs, respectively. The AC3 PFT is the main cause of the overall LAI decline during the summer.

Since more vegetation requires more soil water, the negative correlation between the water stress anomaly and the LAI anomaly is consistent. Indeed, soil moisture stress increases from March to August in the MORCE simulation with respect to the CTL simulation. During June, it is maximum for AC3 PFT with 0.13 in the MORCE simulation and 0.32 in the CTL simulation. For the forest PFTs (TBS and TBE), the soil moisture stress remains low and equal to 0.6 approximately. In August, the soil moisture stress for AC3 PFT is critical and equal to 0.08 in the MORCE simulation. Moisture stress is weaker and equal to 0.22 in the CTL simulation. For TBS and TBE PFTs, the soil moisture stress is slightly weaker in August (0.55 and 0.48 in the MORCE and CTL simulations, respectively). These are however high levels of water stress. The soil water stress anomalies (MORCE-CTL) differ for the various PFTs: it is -0.20 for AC3 and -0.14 for forest species in June. The difference between the MORCE and CTL simulations increases at the beginning of the growing season, when the MORCE simulation produces leaves massively, and even earlier and more quickly for AC3. After the June heat-wave, the vegetation dies in the MORCE simulations. The difference of soil moisture stress decreases. It indicates that the vegetation does not pump water anymore whereas in the CTL simulation, this process is not interrupted. Senescence in the CTL simulation is thus most likely caused by leaf age whereas in the MORCE simulation, senescence occurs earlier by about two weeks and is induced by water stress which reaches a critical threshold.

Thus the moisture supply from soil to the atmosphere decreases during the summer, and drought effect is enhanced especially for C3 crops, due to a root profile less deep than others PFT as broad leaved-tree (Fig. 4.15) .

Figure 4.16 shows that trees, in both MORCE and CTL, have an evapotranspiration around 5.8 mm day^{-1}, whatever the soil moisture is between 180 mm and 300 mm (which is more than 50% of the maximum water available for plants in our model). Crops on the other had have similar evapotranspiration rates (slightly lower) when soil moisture exceeds 220 mm but the rates start to decrease with soil moisture below this "critical" value. In 2002 the domain remain permanently in an energy limited evapotranspiration regime, while in 2003 cropland areas switch to soil moisture limited after the heatwave. This change

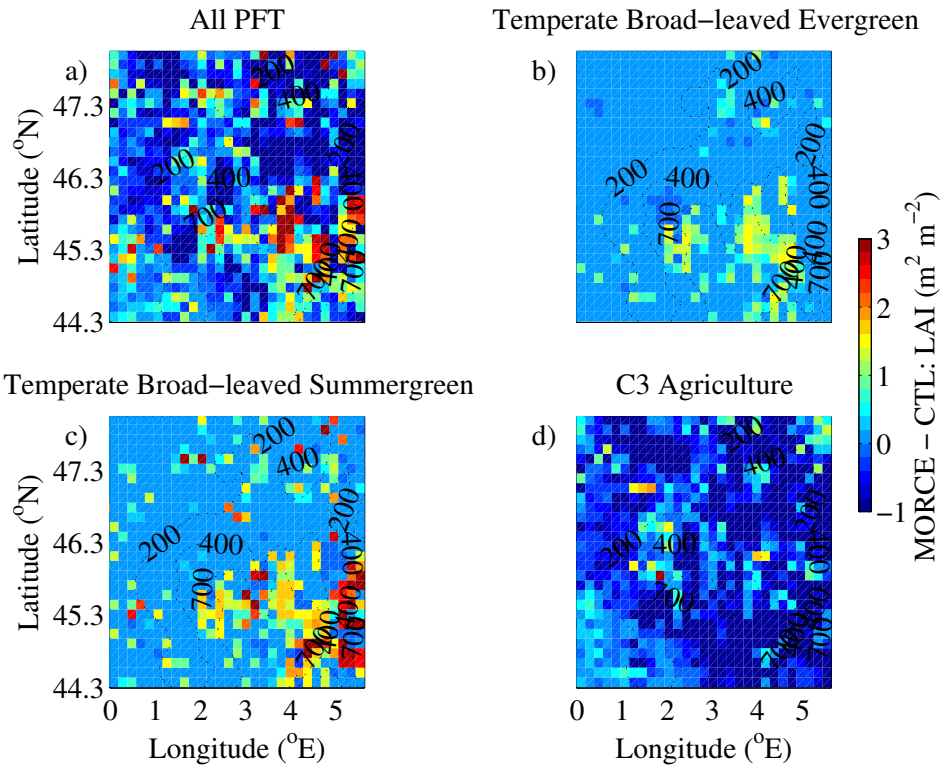

Figure 4.14: Difference between the MORCE and CTL simulations for the agricultural C_3 grass LAI (a-b) and the forest PFTs LAI (c-d). a-c) for June and b-d) August 2003.

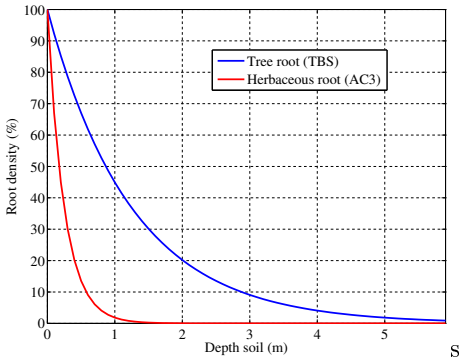

Figure 4.15: Root profile for tree and herbaceous.

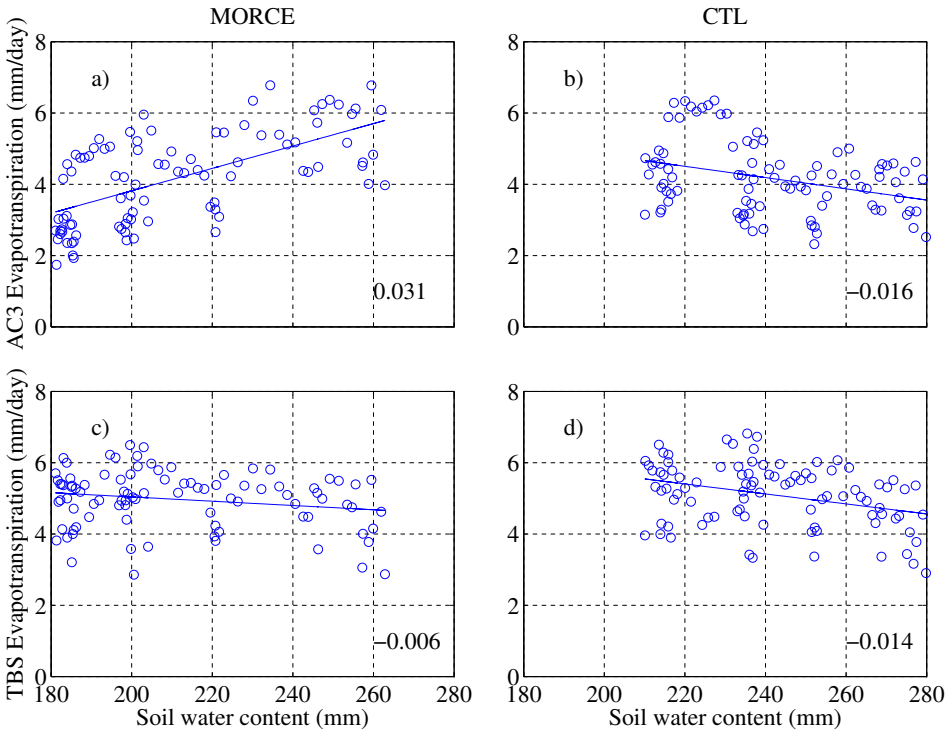

Figure 4.16: Soil water content and evapotranspiration averaged over domain for MORCE and CTL runs during summer (JJA). a-b) for the agricultural C_3 grass and c-d) the forest PFTs. Linear regressions are added in respective colors, and the slope values are indicated in the bottom right corner.

is not observed for forested ecosystem, because water stress is not important enough, as suggested by the high transpiration rate. The difference of response over cropland and forested areas can explain that evapotranspiration is higher in South Eastern subdomain for the MORCE simulation during August. As already stated by *Teuling et al.* (2010), grasses (with a similar behavior than crops) can evaporate more than trees during heat waves as long as moisture is not limited. On long term the conservative water use of trees mitigates drought effect whereas the crops collapse.

Evapotranspiration evolution through summer is consistent with expectation, as the shallow-rooted vegetation typical agricultural land does not have access to deeper reservoirs of water. It dries more quickly than deeper-rooted forest vegetation during a drought, leading to a rapid increase in sensible heat flux and temperature (*Shukla et al.*, 1990). The repartition between cropland and forested area leads to the temperature anomaly pattern between MORCE and CTL during the heat waves (Fig. 4.6).

As a summary, Fig. 4.17 displays a comparison of Bowen ratio, Net Primary Production (NPP) and LAI times series between the MORCE and CTL simulations. For legibility, the curves are smoothed with a 21-day running mean. LAI and NPP indicate a doubling of the vegetation in the MORCE simulation, with LAI peak occuring two weeks earlier. This vegetation surplus induces a higher latent flux and therefore a lower Bowen ratio, until the crops collapse due to the drought. Afterward the loss of vegetation and the moisture depletion enhances the Bowen ratio in MORCE with higher temperature during the August heat-wave. Consequently the dominance change of the Bowen ratio is related to phenology and soil moisture.

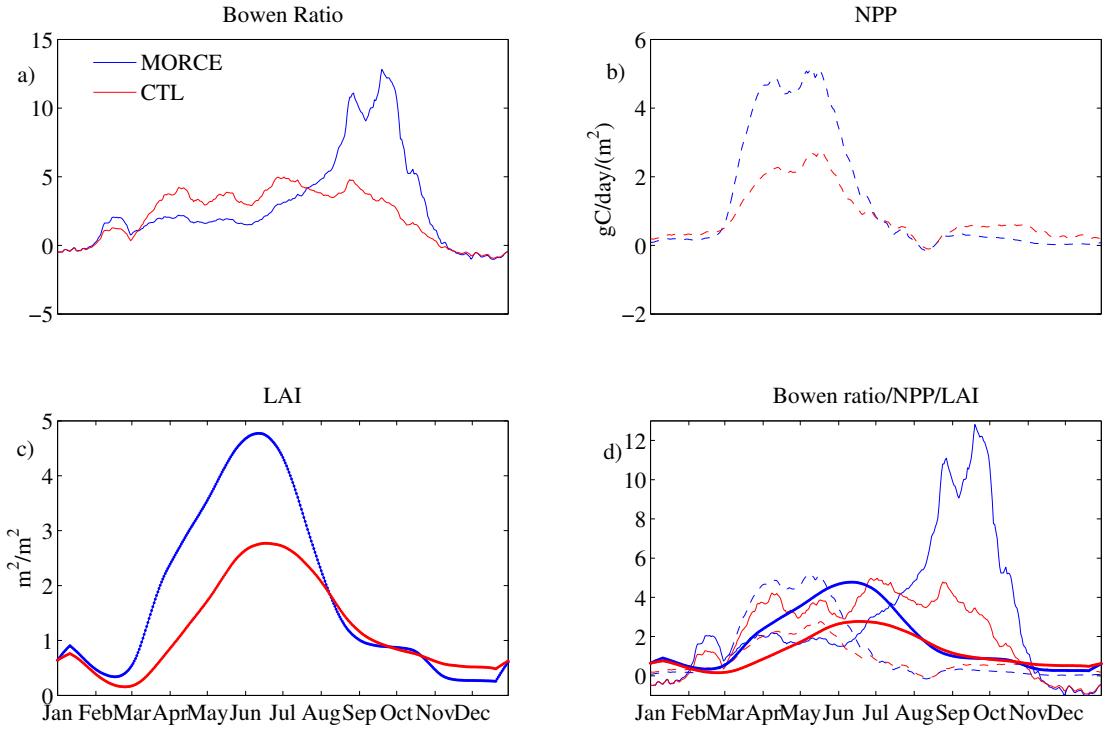

Figure 4.17: Bowen ratio (thin line), Net Primary Production (NPP) (dashed line) and LAI (thick line) times series from January to December 2003, for MORCE (blue) and CTL (red) simulations. The curves have been smoothed using a 21-day running mean.

Comparison with previous studies

Several studies with satellite imagery have been performed to check the state of the vegetation during 2003. Their conclusions are consistent with the results of this paper. The shortening of the growing season in the MORCE simulation and the difference between crop and forested area (subsection 4.1.5) are in good agreement with *Zaitchik et al.* (2006). An analysis of NDVI time series, points out two distinct temporal trends to the vegetation. Positive values during the springtime warmth are associated with an early green up whereas in June, fall begins which will become more severe later in summer, in particular for areas classified as pastures or active crops. Similarly *Teuling et al.* (2010) showed that the heat waves response was ecosystem specific and the most significant for croplands. Moreover the analysis of the photosynthetic activity of the Swiss Alps forest during 2003 summer heat wave have suggested an enhancement of vegetation growth in altitude (higher than 1400 m) and an opposite trend at lower altitude (*Jolly et al.*, 2005) which qualitatively validates our sensitivity study (Fig. 4.12). An explanation is the lengthening of the free-snow season at high elevation and an increase of the evaporative demand at lower elevation. In our study, if we reach the same conclusions we assert that the kind of ecosystem is also a main factor for this elevation effect. However if cold weather, chilling days and snow cover influence LAI evolution in our LSM, as it was pointed out earlier, the beginning of the growing season is identical between the MORCE and CTL simulations. LAI is only enhanced by solar radiation and higher temperature more appropriate and closer to the optimum photosynthetic. Otherwise senescence occurs

earlier in MORCE for agricultural grass, due to the water stress.

4.1.6 Conclusion

This section highlights the effect of dynamical vegetation on the two heat waves that hit Europe during summer 2003. The first heat wave occurred in the second week of June whereas the better known event which had dramatic consequences occurred during the first 15 days of August.

By conducting two high resolution simulations over France, one with prescribed vegetation phenology set to the 2002 behavior and one letting the phenology respond to climate extremes, we found that the vegetation contributes to damp the temperature anomaly in June 2003, while it amplifies the temperature anomaly in August 2003. The two summer 2003 heat waves were preceded by several months of cloudiness and precipitation deficit. Solar radiation was unusually high which was beneficial for vegetation growth. The evolution of the leaf-area index in the two simulations reveals an early development of agricultural vegetation in the simulation with freely evolving vegetation. This unusual excess of vegetation lasts until end of July when the vegetation start dying. This behaviour has two consequences:

1. in June, the excess of agricultural vegetation, caused by high springtime insolation, contributes to increase evapotranspiration and thus more surface cooling, and damping of the temperature anomaly during the heat wave. This effect is not as visible in mountainous regions where the presence of forest and the absence of agriculture do not lead to a modulation of the local water cycle.

2. in August, the death of agricultural vegetation and the critical soil moisture stress contribute to suppress any evapotranspiration and to enhance sensible heat flux, thus amplifying the temperature anomaly during the heat wave.

As also shown in previous studies, water recycling contributes at most to 10 to 20%, thus proving the significant contribution of the effect of the vegetation dynamics on the local to regional water cycle. For the two heat waves, the temperature anomaly that can be attributed to the effect of dynamical vegetation can reach ± 1.5°C for an average total anomaly of about 8°C (Fig. 4.3), which represents a 20% contribution. This is not negligible and is half of the contribution of soil water deficit during the August heat wave which is often seen as a key driving process for heat wave occurrence (*Fischer et al.*, 2007b). We are also aware that agricultural PFT, the main ecosystem in our domain, is one of the most difficult vegetation type to model. Although this PFT parameterization requires improvement to get a more realistic simulation (*Gervois et al.*, 2004; *Smith et al.*, 2010), this coupling already emphasizes that vegetation atmosphere interactions are a major component of the spatial pattern of an extreme event.

One aspect that has not been addressed is the role of the atmospheric chemistry (e.g. ozone) which also has a direct effect on plant stomatal structure (*Anav et al.*, 2011). Indeed, summer heat waves are associated with high insolation and low cloudiness. In nearby urban areas, these conditions are also favorable to strong pollution levels, with especially high ozone concentration. Future work will investigate the additional effect of the severe pollution episode of August 2003 on the temperature anomaly during the summer heat wave.

4.2 Effects of anthropogenic land cover change

Events similar to the 2003 mega heat wave will be likely more frequent, intense and longer by the end of the 21st century owing to enhanced atmospheric greenhouse-gas concentrations (*Beniston*, 2004; *Schär et al.*, 2004). Although the biogeophysical effect of land cover change seems able to partially or totally compensate the biogeochemical impact of increased greenhouse-gas (*Findell et al.*, 2007; *Jackson et al.*, 2008; *Pitman*, 2009). So far studies conducted in the Mediterranean have contradictory results (cooling or warming) (*Heck et al.*, 2001; *Gaertner et al.*, 2001; *Anav et al.*, 2010a). With the help of the modelling platform MORCE, the impact of a potential vegetation on the 2003 summer heat waves is compared with the impact of the existing vegetation. The differences in vegetation cover is related to conditions that would exist in the absence of human disturbances, which leads to a substitution of crops, the main PFT, by forest and natural grass.

4.2.1 Numerical experiments

The simulated domain and the numerical setup is similar to the one described in section 4.1.3. Two simulations are carried out for the anomalous year 2003, one with a potential vegetation distribution where human influence is suppressed (POT) to a simulation with a current vegetation distribution (CUR). This latter corresponds to the MORCE simulation in section 4.1.

The map of potential vegetation used for the simulation is obtained by taking a map issued by spatial observations of the AVHRR-mission 1992-1993 (*Loveland et al.*, 2000). The initial grid resolution of 1 km has been aggregated to 0.5° to save numerical resources (*De Noblet-Ducoudré*, 2012). Then, the global map of 17 vegetation classes is reclassified into the 13 PFT classes which are used by ORCHIDEE. Among these PFTs, the surface fractions occupied by agricultural land uses are deleted and redistributed equally on all the remaining PFTs (Fig. 4.18). The map of current vegetation which serves for comparison is issue of the same spatial observation mission and is aggregated to 5km and reclassified as described in section 4.1.2. See also Figure for more details.

Figure 4.19a) shows the surface per grid cell which is occupied by the agricultural PFTs in CUR simulation. The black solid lines indicate the relief with the Central Massif in the southern part of the domain. In addition to that, Figure 4.19b) shows the LCC as the percentage of surface per grid cell which has been altered between both simulations from one PFT to another one. Except the south-eastern part of the domain with 75.5%, the rest of the domain has around 90% of its surface modified from one land cover to another one. As the construction of the vegetation maps uses different resolutions (see Figure 2.2), the final vegetation maps are interpolated (for the POT simulation) or aggregated (for the CUR simulation). Thus, the LCC exceeds the fraction of agricultural PFTs in CUR simulation, but shows also changes due to the differences in the map creation process. The main changes from CUR to POT simulation consist in replacing agricultural PFTs (account for 69.1% of the total surface) by forested PFTs (mean difference POT-CUR of almost 34%) and natural C_3 grasses (mean difference of almost 30%). Less important fraction changes concern the PFTs of bare soil (-6.03%) and of evergreen needleleaf trees (10.65%).

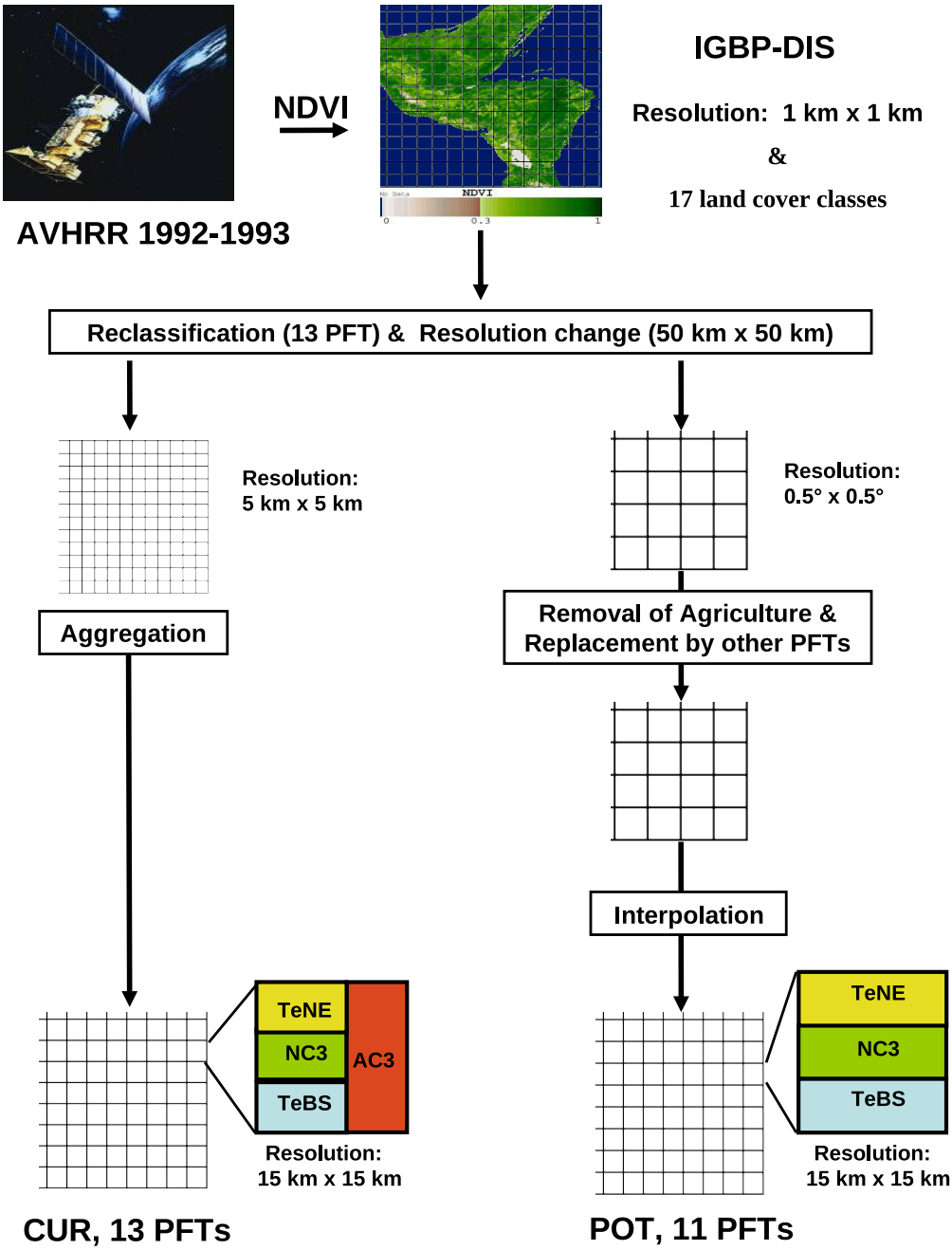

Figure 4.18: Scheme illustrating the construction of the current and potential vegetation maps used for CUR and POT simulations. AVHRR is the Advanced very high resolution radiometer and IGBP-DIS the International Geosphere-Biosphere Program Data and Information Systems.

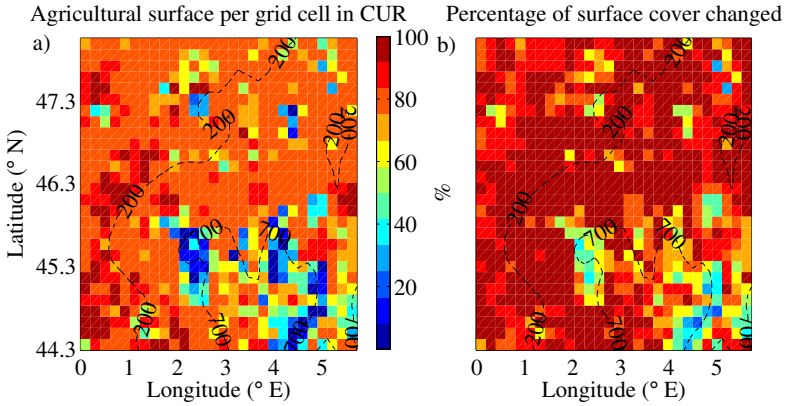

Figure 4.19: Percentage of surface per grid with a) agricultural land cover in CUR simulation and b) a different land cover in POT simulation. Dashed lines indicate the relief.

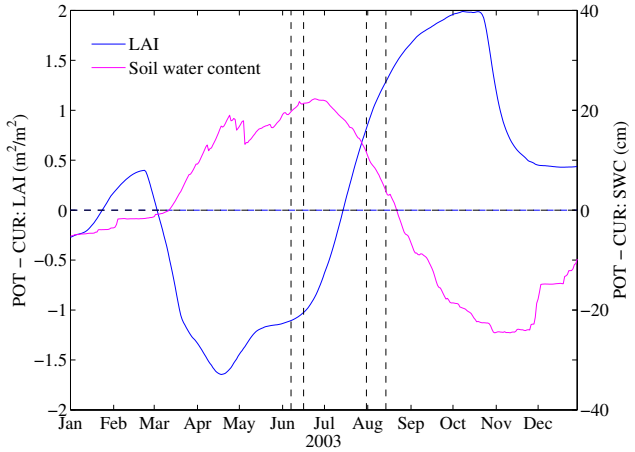

Figure 4.20: Evolution of LAI anomaly (blue) and soil water content anomaly in soil layers (purple). The vertical dashed lines indicate the periods of the heat waves.

4.2.2 Simulation results

This chapter presents main results for different prognostic variables. The following sections treat the LCC induced changes for the temperatures, the performance of the vegetation (its phenology), the surface energy budget and the precipitation. In most cases, only data of 2003 is used for calculations and visualizations as the 2 models might not yet be perfectly balanced with the atmospheric conditions in 2002. The validation of the CUR simulation against observations of the European Climate Assessment Data is previously shown in subsection 4.1.3.

Figure 4.20 shows in 2003 the difference between POT and CUR for the LAI averaged over the different PFTs and soil water content (shown as the height of the water column in soil). It provides an estimate of the development of the canopy of tree and agricultural grass PFTs in POT and CUR simulations respectively. The abrupt changes for tree PFTs seen on Figure 4.20 in the beginning and in the end of the year are caused by the senescence of the summergreen trees which do not contribute further to the calculation of the average. Tree PFTs have in general larger LAI values than grasses with the exception

of the agricultural C_3 grasses PFT which can reach a LAI of 6. When comparing the development in both years, one will find an early leaf onset for all PFTs (especially the grass PFTs) in 2003 due to the clear sky conditions as described by *Zaitchik et al.* (2006). In June 2003, the grass vegetation has almost reached its maximal development state and is thus less impacted in its growth by the first heat wave than the tree species whose growth is then slowed down. However, the grass PFTs also suffer from the first heat wave which becomes manifest in major leaf losses at the beginning of July with a delay of half a month for the grass PFT in POT. This dramatic welting leads to LAI of 0.3 (CUR) and 0.7 (POT) at the end of the year, 1 m^2m^{-2} smaller than at the beginning of 2002. The second heat wave in August throws back the LAI development for tree PFTs in both simulations which therefore only reach a maximal LAI that is 0.5 m^2m^{-2} smaller than the year before. At the end of the year, tree PFTs according to their LAI (0.5 m^2m^{-2} smaller than at the beginning of 2002 or 2003) seem less damaged by the anomalous year than grass PFTs (1 m^2m^{-2} smaller than at the beginning of 2002 or 2003). By taking the surface covered by each PFT into account, the total LAI per grid cell shows to be more important in the CUR simulation from the leaf onset of the Agricultural PFT in March to July with maximal values reaching almost 4 m^2m^{-2}. Afterwards the POT simulation has a larger LAI which attains a maximum of 3 m^2m^{-2}. The total LAI cycle is delayed in POT simulation compared to the CUR one by about one and a half month which is mainly due to the late leaf onset of the dominant broadleaf summergreen forest in POT in comparison to the Agricultural C_3 grass in CUR. The total LAI in POT is dominated by forest and grassland (the TeBS, NC3 and TeNE PFTs) and the one in CUR by Agricultural C_3 grass.

Both simulations show a similar evolution of the soil water content throughout the year (Fig. 4.20). However, the CUR simulation depletes water ressources faster during the growth period of the AC3 PFT. After the second heat wave, the restock is faster as well because the demand in evapotranspiration is reduced (plants reduce their LAI). Another measure of water stress for PFTs is the weekly Soil Moisture Index (SMI), which ranges from 0 for no water availability to 1 for saturation. Due to the soil water depletion in spring the most stressed PFTs in CUR simulation have to face a SMI of 0.4 at the beginning of June while the most stressed PFTs in POT simulation have a SMI of 0.6 (not shown). Differences are greatest for grass PFTs. From the middle of March until the first September tree PFTs are more stressed in the CUR simulation and grass species until the first November. The water stress limits transpiration of the PFTs and impacts on photosynthetic activity and respiration, thus also on the biomass production.

The temperature evolution in CUR represents well the annual cycle and the anomalies compared to the climatological mean during the summer months. A comparison of the evolution in both simulations (see Figure 4.21) shows the POT simulation to be hotter from the leaf-onset of the AC3 to the beginning of July when CUR simulation has the larger surface temperatures. This holds true for daily minimal (0500-0800 UTC) and maximal (1400-1700 UTC) temperature periods. However the evolution of the temperature is slightly delayed for the daily minimal temperatures. The differences do not exceed but rarely 1K. In June surface temperature are in average 0.54 K hotter in the POT simulation and in August they are 0.21 K cooler. The distributions of daily maximal temperatures are different for both periods. This shift in the average is accompagnied by a decreased variability of the temperature differences in August. These results are consistent with other studies, as for example *Dümenil Gates and Ließ* (2001) who used a GCM to simulate afforestation and deforestation impacts on global and regional climate in the Mediterranean region with an horizontal resolution of about 2.8 in longitude and latitude (about 250 km in the zonal and 300 km in the meridional directions for the Mediterranean region). They obtained

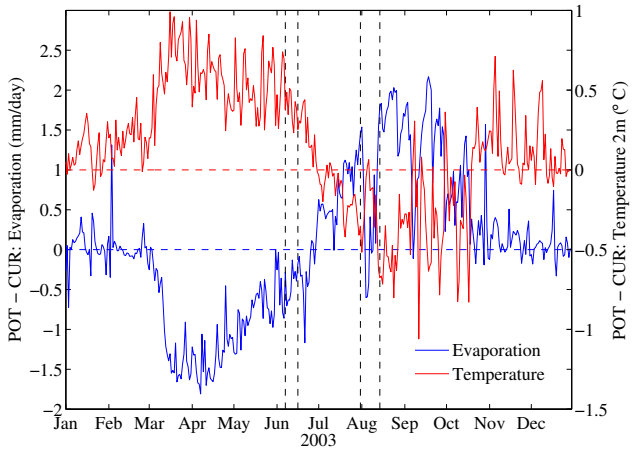

Figure 4.21: Difference between the POT and CUR simulations for the evapotranspiration (blue line) and surface temperature (red line) at 1500 UTC. Vertical dotted lines delimit the heat waves of June and August.

maximal differences for the 2m temperature of 1K as well. Another study of *Anav et al.* (2010b) showed surface temperature differences to reach 1.2 K in an simulated afforestation in north-western Europe. They employed a RCM and a potential vegetation map which represents the absence of human influence on the vegetation distribution. An observational study on different FLUXNET sites in Europe showed forest sites in Central France to be up to 3.5 K cooler during August 2003 than the closest grassland sites (*Teuling et al.*, 2010). Contradictory results have been obtained by *Heck et al.* (2001) who used a vegetation map representing the conditions 2000 years ago to simulate with a RCM the years 1987 to 1992. They found as well a sign switch in their compared simulations between May and August. However, the maximal difference in 2m surface temperatures during May in Spain and southern France amounts to a cooling of 2 K in the potential vegetation simulation and is hotter in August.

The evapotranspiration in the POT simulation is dominated by the PFTs of TeBS and NC3. After a first period during which evapotranspiration is increasingly more important in CUR simulation (see Fig. 4.21) due to the large LAI of the fast growing AC3-PFT and the smaller stomatal resistance for dominating grass PFTs in CUR simulation, the difference is reduced mainly by the development of the canopy of the TeBS in POT simulation. A third period can be distinguished when the agricultural plants canopy starts to diminish after the first heat wave in June. A few days later evapotranspiration starts to be more important in the POT simulation. The new maximal difference between both simulations is reached after the end of the second heat wave in August.

Similar modeling studies which compared the impact of different vegetation (distributions) on climate variability found these kind of sign switch as well. In the study of *Heck et al.* (2001) for instance, the evapotranspiration in the Mediterranean region during a "normal" year was more important in a simulation with a forest dominated, potential vegetation map until the beginning of July when it gets limited by the lack of soil moisture and the simulation with current vegetation distribution has larger evapotranspiration rates. They did not observe such a sign switch in other regions in Europe and explain it with a faster drying out of soils in POT simulation which cannot be observed in our simulation. TEULING et al. [2010] in their comparison of the impact of the heat waves on fluxnet sites with forest

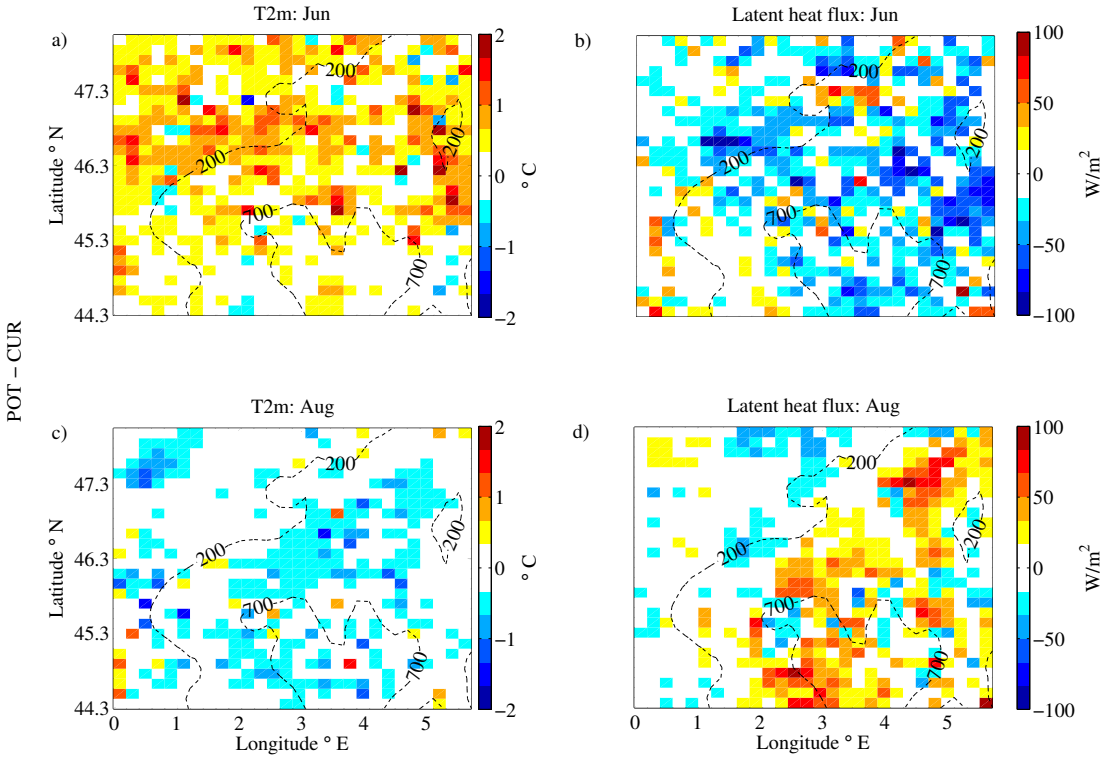

Figure 4.22: Difference between the POT and CUR simulations for the 2-m temperature (a-c), latent heat flux (b-d) at 1500 UTC averaged over the heat wave period in June 2003 (a-b) and August 2003 (c-d). Dashed lines are height of topography.

or grassland dominated vegetation found a sign switch as well which had the same direction as in our study. In persistent heat conditions the forest sites with their conservative evapotranspiration showed to be more resistant against in heat waves by preserving the soil water resources.

As shown on Figure 4.22, the latent heat fluxes during the first heat wave in June are more important in the CUR simulation due to its larger transpiration. In August, a sign switch can be observed, favouring now latent heat fluxes in the POT simulation. The sensible heat fluxes which are more important for the POT simulation in June switch sign as well and become larger for the CUR simulation in August (not shown). The differences in both heat fluxes are anticorrelated spatially and significantly different from zero but differences in latent heat fluxes exceed those in sensible heat fluxes. In addition to that, spatial variability decreases from June to August. Concerning the temperature the most important difference in June is located in the northern part of the domain, where the LCC is the larger. These difference corresponds to warmer temperature in POT up to 2°C. In August the sign switch induce cooler temperature in POT (2°C locally) and the location of temperature changes seems less organized around the LCC pattern. Nevertheless the monotonic anticorrelation (-0.32) in August is larger than the correlation in June (0.24) according to a spearman correlation for the temperature difference, significant at the 5% level.

Fig. 4.23 shows that POT is not moisture limited since forests PFTs present high evapotranspiration rate regardless the soil moisture content whereas the crops in CUR have restricted their evapotranspira-

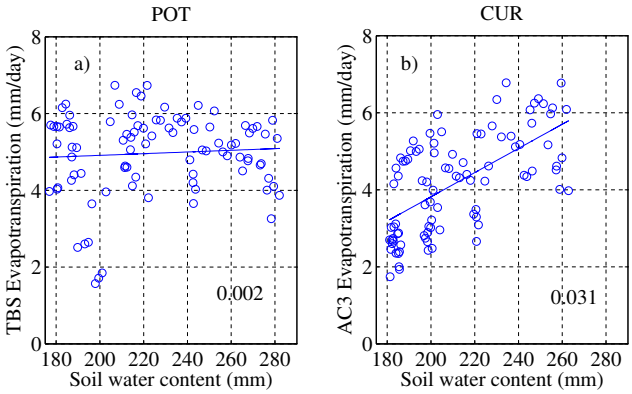

Figure 4.23: Soil water content and evapotranspiration averaged over domain for POT and CUR runs during summer (JJA). a) for the forest PFTs and b) the agricultural C_3 grass. Linear regressions are added, and the slopes values are indicated in the bottom right corner.

tion. It confirms that the second heat wave is mitigated by the conservative water use of trees whereas the crops collapse, in accordance with the previous discussion with Figure 4.16.

According to the general equation for the surface energy budget if the soil temperature is in equilibrium, the net radiation R_{net} can be decomposed into non reflected fractions of incoming shortwave ($SW\downarrow$) and longwave radiation ($LW\downarrow$) :

$$\begin{aligned} R_{net} &= \lambda E + SH + G \\ (1-\alpha)\,SW\downarrow - \epsilon\sigma T^4 - (1-\epsilon)\,LW\downarrow &= \lambda E + SH + G \end{aligned}$$

where SH refers to the sensible heat flux, λE to the latent heat flux, G to the ground flux, T to the soil surface temperature, ϵ to the soil emissivity and σ to the Stefan–Boltzmann constant. In the following the ground flux G will be neglected as its contribution is minimal compared to the other two heat fluxes. The fraction of the at the surface available energy which is transformed into turbulent heat fluxes can thus be obtained according to equation :

$$F = \frac{\lambda E + SH}{(1-\alpha)\,SW\downarrow + LW\downarrow} = \frac{\lambda E + SH}{SW_{net} + LW\downarrow}$$

This fraction F allows not only to estimate the fraction of available energy which is transformed into turbulent heat fluxes but also the remaining part which heats up the surface and contributes to the outgoing longwave radiation ($LW\uparrow$). Previous studies have shown that F ranges between 20 and 25%, and thus 75-80% of energy is used to heat the earth's surface and to determine the surface temperature (*De Noblet-Ducoudré*, 2012). The Figure 4.24 summarizes important features of the surface fluxes. Hence, Figure 4.24 a) demonstrates that net radiation is more important in the POT simulation during the establishment of the TeBS canopy according to the less important albedo values (not shown) which allow to absorb more of the incoming energy. The difference (POT-CUR) in mean total albedo amounts to maximal values of -3% (POT-CUR) at the end of October. In addition to that it can be observed that a sign switch of the difference between both simulations first takes place for the latent heat flux. Some days later, the sensible heat flux becomes less important in the POT simulation. This change is due to the

sign switch of the difference (POT-CUR) in the evapotranspirative flux which impacts on the partitioning of the available energy between the turbulent heat fluxes. The increase fraction of sensible heat fluxes contributes to the warming of the lower troposphere and thus to the sign switch in surface temperature observed for the beginning of July (Figure 4.21). Figure 4.24b) shows the Bowen ratio (QH/QL) for both simulations. The first difference between the simulations occurs at the time when the total LAI in the CUR simulation exceeds that of POT simulation. With the delayed leaf onset in POT simulation in April the Bowen ratio starts to diminish until the end of the year. The Bowen ratio in the CUR simulation starts to increase after the first heat wave in June when the total LAI and the related latent heat fluxes reduce. This is also the moment when the Bowen ratio in the CUR simulation becomes more important than the one in POT simulation.

The Figure 4.24c) then shows F for both simulations and their difference. In summer about 17% of the energy which is available at the surface is transformed to turbulent heat fluxes which is somewhat less than the reported values from the LUCID experiment *De Noblet-Ducoudré* (2012). Following the annual radiative cycle the two simulations start to differ from the first heat wave on, when the F becomes continuously more important in POT simulation. This illustrates that a larger part of the available energy is available to heat the surface and to increase $LW\uparrow$ in CUR simulation until September when the SMI in POT reaches is minimal values and thus latent cooling is limited in POT simulation as well. The last illustration (Fig. 4.24d) compares the difference in longwave radiation for the downward $LW\downarrow$ and the net radiation $LW\downarrow - LW\uparrow$ averaged over the whole domain. The values of LW_{net} being mostly negative, a negative (positive) difference indicates a larger (smaller) LW_{net} in POT simulation. While the differences in $LW\downarrow$ do not show a specific evolution this is indeed the case for LW_{net}. Outside the phenological cycle (from January to March and from October to the end of the year) LW_{net} has the same behaviour as $LW\downarrow$, but from the leaf onset of agricultural C_3 grass in CUR simulation to the beginning of July it dominates in POT simulation due to a lack of latent cooling before a sign switch occurs at the beginning of July (Fig. 4.24 a). Thus primarly, the changes in cloud cover which would be visible through a distinct sign in the $LW\downarrow$ difference do not seem to play a major role and secondly the POT simulation is more limited in its ability to cool the surface until the beginning of July when the vegetation in the CUR simulation starts to fade.

Pitman (2009) compared in their study differrent model outputs according to a deforestation scenario over Europe. They found decreases of 10 to 20 W/m2, mixed changes as well as increases of 5-10 W m^{-2} in latent heat fluxes. *Anav et al.* (2010b) as well found only weak changes for (spatial averaged) summer turbulent heat fluxes caused by a deforestation and afforestation scenarios. Less consistent results have been found in the study of *Heck et al.* (2001) where a decreased longwave emission of the potential vegetation causes a slight increase (4 W m^{-2} in June) for R_{net} in comparison with a current vegetation distribution and decreased cloud cover takes over the difference in albedo when reducing the $SW\downarrow$ radiation by 2 W m^{-2} in June in the simulation with potential vegetation. Increased latent cooling contributes further to a smaller Bowen ratio in the Mediterranean region. The most striking results have been found by *Teuling et al.* (2010) who measured an up to 90-132 W m^{-2} stronger R_{net} over forested sites when comparing to the closest grassland site.

Previous studies on different regions (*Crétat et al.*, 2012) have shown the difficulties of the model WRF to correctly reproduce precipitation patterns. Especially if a convection parameterisation scheme is applied (as in the case of these simulations) the total rain amount tends to be overestimated (*Done*

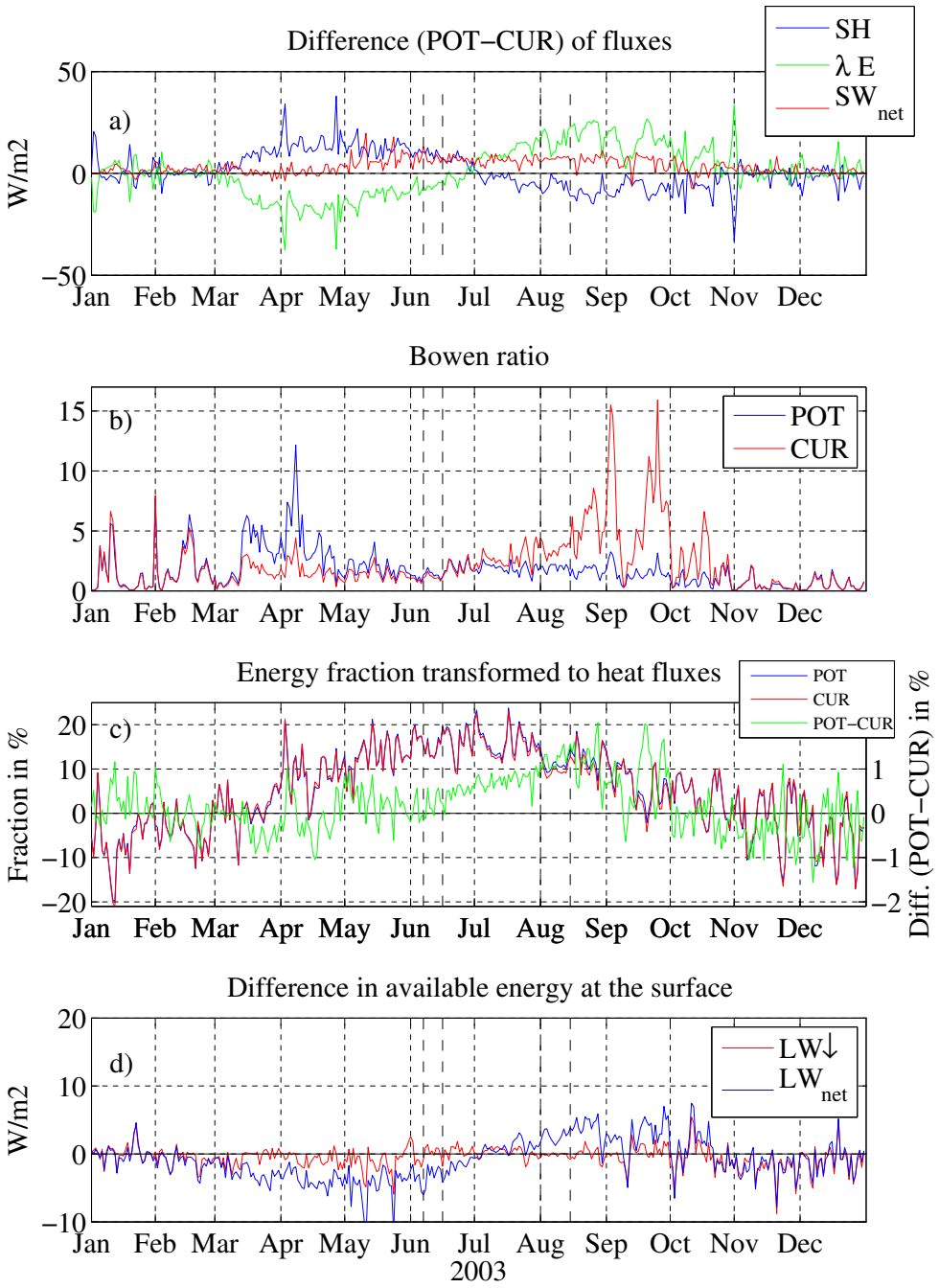

Figure 4.24: Time series of a) difference (POT-CUR) of spatial mean heat fluxes and of SW_{net} for the whole domain, b) Bowen ratio for both simulations, c) F for both simulations and difference (POT-CUR) between them and d) Differences in longwave radiation LW at the surface. The vertical, dashed lines indicate the periods of the heat waves.

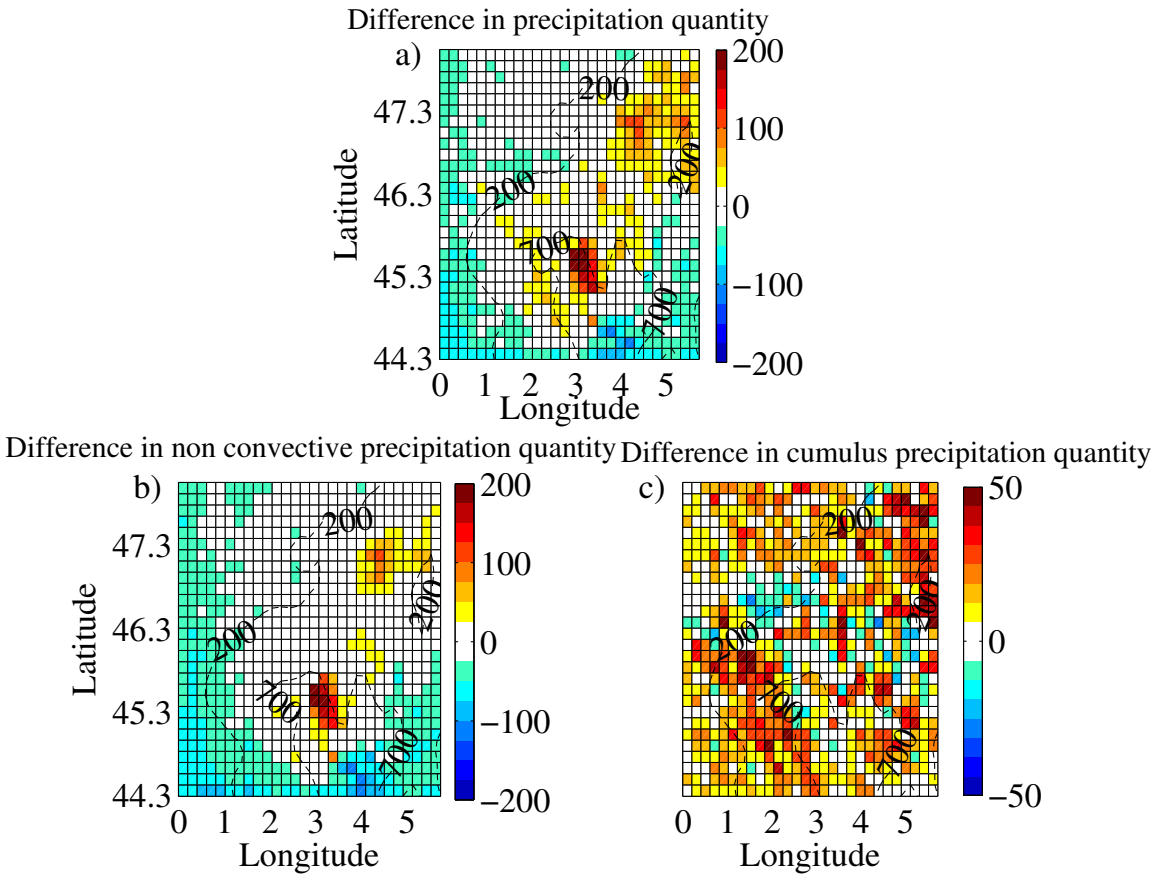

Figure 4.25: Total accumulated difference (POT-CUR in mm) for the year 2003 in a) total precipitation amount and for b) non-convective and c) convective precipitation. The dashed lines indicate the relief.

et al., 2004) and can lead to bias in the model results. Therefore different threshold values for the elimination of low-intensity precipitation were applied to the analysis of the frequency of precipitation occurrences. All days with precipitation occurrence were counted for 2003 at each grid cell. According to published statistics[1] which rely on Météo France data, it rains in average on 42 % of the days in France. Thus, the threshold value for precipitation intensity is determined such as both precipitation types have an accumulated occurrence probability of 42 % per day in the CUR simulation, which matches a deletion of all precipitation less intense than 0.062 mm h^{-1}.

The Figure 4.25a) shows the accumulated difference in precipitation which amounts to 0.1907 mm yr^{-1} in spatial average favouring POT simulation. A general tendency from less precipitation in POT simulation in the south-western corner to more precipitation in the north-eastern one can be detected. This mean difference is very weak considering the absolute precipitation amount of about 830 mm during 2003 in CUR. Nonetheless, an important change in the characteristics of the different precipitation types can be observed and differences amount locally to up to 200 mm in 3 months (from January to March) which is 24% of the total annual precipitation. Moreover, there is a slight change towards more convective precipitation in POT simulation.

[1] http : //www.alertes-meteo.com/divers-pheno/pluie tableaux.htm

The differences in these regions are mainly due to non-convective precipitation in autumn and winter which are the seasons with most of the nonconvective precipitation as well. The differences in convective precipitation are less important in absolute quantities and do not show a specific spatial pattern (not shown) which could be related to the relief or the location of main LCC. They account less to the total precipitation amount but show nevertheless a sign switch between the first and the second half of the year.

Even if the spatial pattern for difference in convective precipitation is not as marked as for the non-convective precipitation we observe that the convective precipitation is rather amplified by the vegetation distribution in POT simulation (Fig. 4.25c), the non-convective precipitation (Fig. 4.25c), favours CUR simulation besides two specific regions. Local effects cause the slight increase in average precipitation in POT simulation despite the negative difference elsewhere. Generally the non-convective precipitation events in POT simulation always exceed those in CUR simulation in intensity and length (up to several hours).

In 1994, a simulation study was published in the course of the HAPEX-MOBILHY campaign, which showed that the replacement of bare soil by forests on a domain (400 km $\times$ 400 km) in south western France could increase the frontal rainfall by 30% half of which were issued by rapid re-evaporation of intercepted rainfall on the leaves and the other half by moisture convergence (*Blyth et al.*, 1994). More up-to-date research often finds changes in precipitation induced by LCC to be randomly distributed and less important especially during the winter months when baroclinic disturbances dominate over Europe (*Dümenil Gates and Ließ*, 2001; *Pitman*, 2009). *Heck et al.* (2001) found a sign switch for the precipitation signal as well. While in May accumulated precipitation in the simulation with potential vegetation exceeds that in the control simulation in large parts of our simulation domain, the opposite is the case during August when accumulated precipitation in the control simulation is 5 to 10 mm larger. The impact they observed was visible mainly for the convective precipitation.

4.2.3 Discussion and conclusion

In this part we compare the impact of a potential vegetation distribution where human influence is suppressed and no agriculture exists to a simulation with the current vegetation distribution for the anomalous year 2003. Further we want to identify the main processes which contribute to these differences. Therefore we performed a simulation with a potential vegetation map and compared the results to the MORCE simulation. In this way about 90% of the surface experiences a land cover change (LCC) respective to the CUR simulation with exception of the mountainous region in the south part of the domain which experiences a less pronounced LCC. As the LCC corresponds to conversion of agricultural land use to natural grasses and forests it can be compared to a reforestation of about 45% of the domains surface (the remaining surface is covered by grassland). The first heat wave occurred during June and the second during August. While vegetation in June was able to compensate the increased incoming energy by latent heat fluxes, it became water limited in July and reacted to the second heat wave above all with increased sensible heat fluxes which increased temperatures close to the surface.

By replacing the agricultural vegetation by a mixture of forests and natural grasses, the capacity of photosynthetic activity is reduced due to increased stomatal resistance of trees and decreased leaf area index (LAI). The exceptional meteorological conditions in 2003 enhance development of vegetation in both simulations and result in great photosynthetic activity and transpiration for which the simulated

agricultural plants have larger capacities. Therefore they can evacuate the heat excess with latent heat fluxes to the atmosphere while the forest dominated vegetation in POT is heating up more severely during the first heat wave. However, plants start to get limited in soil moisture in July and grasses in general as well as agricultural plants especially (due to their high water consumption in spring and early summer) are most affected and start welting. In this circumstances the simulation without human impact on land cover plays out its advantage of greater heat resilience on the long term. As the strong control of transpiration conserved soil water resources and due to the larger rooting depth of trees, the impact of the second heat wave in August on vegetation, temperature and the repartition of turbulent heat fluxes emphasizes the better performance of the potential vegetation which leads to a dampening effect of in average 0.21 K for the daily maximal temperatures.

This striking result of a sign switch for the difference (POT-CUR) in several parameters (evapotranspiration, turbulent heat fluxes, surface temperature and convective precipitation) was found in other comparable studies, too. In section 4.1 I compare two coupled simulations with different configurations of the surface model ORCHIDEE for the same domain as in this study: the CTRL simulation uses a prescribed LAI according to the evolution in 2002 for which the effect of vegetation was limited to stomatal resistance and the MORCE simulation uses a free evolution of the LAI and corresponds to the simulation CUR of this study. The specific behaviour of the vegetation in 2003 could be highlighted and it was shown that the free evolution of the LAI results in premature development of the canopy which contributes to a dampening of 0.55 K for the heat anomalies in June and to a heating of 0.4 K in August due to early welting of agricultural plants. This early senescence is caused by the increased depletion of soil water resources in comparison to the prescribed LAI simulation . My study has to be seen in the continuation of this approach since it evaluates not only the response of the vegetation to the climatic conditions and potential feedbacks, but looks further on how human impact in the form of LCC contributed to amplify or dampen these mechanisms and feedbacks. Therefore the vegetation feedback during the heat waves is similar but in the case of section 4.1 it is due to slide of the phenological cycle while it is the mean phenology for each vegetation cover which differs in my simulation.

The article of *Teuling et al.* (2010) took a different approach in order to determine the resilience of different vegetation covers to heat waves. They used data on fluxes from sites of the observational network FLUXNET1 in central western Europe and distinguished between grass/cropland and forest sites. Temperature measurements for the sites have been taken from the European Climate Analysis and Dataset *Tank et al.* (2002). During persistent heat wave conditions ($>$ 5 days) they showed that the evolution of evapotranspiration differed for the two vegetation types according to different stages and estimated them for the summer 2003: A first stage, when evapotranspiration is unlimited until the beginning of July, a second when it gets limited by available soil moisture until the beginning of August and a third when it becomes negligible for the rest of the summer. In addition to that, they used satellite data (MODIS and Aqua) to calculate land surface temperature anomalies for pixels with dominant ($>$67%) forest or grass vegetation and found that during July the anomalies were similar while in August air temperatures over grassland were up to 3.5 K hotter than over forest. They suppose grassland in August to be in a second or third drying stage. These results are consistent with the sign switch observed in latent and sensible heat fluxes and surface temperatures in our simulations. However the amplitude in *Teuling et al.* (2010) exceeds our simulation as they observed on a very small scale (30" for satellite data) with homogeneous land cover. Even if they addressed a similar research question to

us, the results are rather a complementary confirmation of our simulations. While their study provides precise instantaneous impressions of the conditions during the heat waves, they lack information on the other parameters and can thus make only suppositions concerning the underlying processes.

One study with a modelling approach which analysed a potential vegetation cover over Europe, too, found contrasting results. *Heck et al.* (2001); *Gaertner et al.* (2001) used the RCM EM (Europa-Modell) based on hydrostatical equations and a horizontal resolution of 56km to simulate an ensemble of 6 simulations of the months April to August from 1987 to 1992. Further they employed a landsurface scheme of intermediate complexity and ECMWF reanalysis fields and NCEP reanalysis data (for soil moisture) to initialize their simulation. They compared a simulation with the current vegetation cover and prescribed LAI (obtained by satellite observation) to a potential one for which the surface fractions are derived from ecophysiological constraints of the current climate. Additionally they fixed the roughness length in order to focus on feedbacks based on evapotranspiration. The mean LAI of their CTRL simulation (thus based on observation) is smaller than in our CUR and in their POT simulation. It is the difference in the description of the LAI which finally leads to contrasting results. Even if the authors also observe a sign switch, the simulation with potential vegetation cover is colder (by 2K for temperature at 2m) in May and warmer in August (1K) for maximal differences in Spain. Only in central and northern Europe the CTRL remains warmer throughout the simulated 5 months. The larger LAI in POT leads in the same manner as CUR in my simulation to larger evapotranspiration rates and convective precipitation in May. Afterwards the CTRL simulation takes over. They showed that vegetation distribution "influences convective precipitation by controlling the structure and depth of the boundary layer, in response to a modified partitioning of the turbulent heat flux" while radiative effects seem to be less important for the hydrological cycle. A part from the differences in LAI, the coarser horizontal resolution (56km) and the hydrostatic assumption may contribute to the contradictory results. However, the identified mechanisms which contribute to the sign reversal and the characteristic pattern for the Mediterranean region are consistent with our results.

Another contrasting outcome compared to the results presented by other authors is the significant difference that can be recorded for the precipitation on local scales in our study. Theses differences can amount up to 24% of the average annual precipitation over the domain. This is especially remarkable as precipitation in winter months is mostly dominated by large-scale patterns and to a much lesser extent by the surface characteristics which is why other studies reported to observe no or no significant changes (*Dümenil Gates and Ließ*, 2001; *Heck et al.*, 2001; *Pitman*, 2009). It might be possible that the modified surface roughness on the dominant wind direction changes the surface wind module and enhances together with orographic effects advected precipitation in the Central Massif region. However, the exact mechanisms involved are not clear yet and need further investigations.

Chapter 5

Conclusions and perspectives

5.1 Conclusions

This thesis aimed at highlighting and improving the understanding of the coupled processes between soil, vegetation and atmosphere during the heat waves in the Euro-Mediterranean region. This issue was tackled by means of regional coupled models, suited for the study of mesocale processes and in the conclusion here we synthesize the main breakthroughs.

Climate modelling has long been approached using coupled global climate models (CGCM) that were designed to study the broader scales of atmospheric circulations (around 100 km grid resolution). The coupling between the various compartments of the Earth system plays an active role in climate variability (*Koster*, 2004; *Seneviratne et al.*, 2006), especially in mid-latitudes. Therefore the investigation of the Mediterranean climate requires the development of suited tools to quantify the regional response of the Earth system to a large-scale forcing. For this purpose I contributed to the development of the MORCE platform by coupling the WRF regional climate model and the ORCHIDEE dynamical global vegetation model. WRF uses a non-hydrostatic atmospheric dynamics which makes it possible to process downscaled simulations with horizontal resolution of few kilometer scale, and ORCHIDEE computes the hydrological and energy budget as a classical land surface scheme but additionally takes into account the dynamics of vegetation and leaf phenology. The most important point is that coupling those models enables the vegetation feedback on atmosphere, which is not currently done in most RCM.

Extending summer heat wave predictability on to a seasonal scale is today a challenge for meteorological forecasting. To achieve a substantial enhancement numerous processes could be improved or highlighted, but it seems that driest winter/spring seasons play a key role in heat during the summer. Studies suggest that dry air formed above the Mediterranean land spreads northward throughout Europe by occasional southerly wind, leading to an increase in the summer temperature or heat waves temperature when coordinated with specific weather regimes (*Vautard et al.*, 2007; *Zampieri et al.*, 2009; *Quesada et al.*, 2012). The chapter 3 of this thesis has shown that heat waves in the Euro-Mediterranean region are identified and classified according to a specific spatial pattern and location. I have been able to prove that only specific heat wave classes are sensitive to remote or local preconditionning of droughts. Mediterranean and central Europe are regional hot spots where the coupling between soil wetness, precipitation and temperature is active. After stuying its intraseasonal aspect, I pointed out the immediate effect of soil moisture depletion during heat wave periods by carrying out a sensitivity experiment centered on

France between 1989 and 2008. The WRF model receive different surface boundary conditions from two different land surface schemes. The first resolves water movement and is able to simulate the summer dryness whereas the second prescribes high moisture availibility for evapotranspiration. With or without drought conditions, heat waves are produced independently from soil wetness. As a consequence they are mainly triggered by persisting synoptic blocking conditions over the region. Moisture deficit contributes to an averaged positive bias of 4.4°C and leads to an increase in temperature variability up by 1.4°C on the 95th centile of the local temperature probability density function. Different soil moisture-temperature responses over low-elevation areas, over mountains and over coastal regions are highlighted.

In the plain regions, the temperature enhancement relies on a mechanism of positive soil moisture temperature feedback, where the conversion of solar radiation into heat at the expense of evapotranspiration leads to higher temperatures. This well-known process has been found to contribute to 40% of the temperature anomaly over low-elevation plains. In mountainous regions, enhanced heat fluxes over dry soil reinforce thermal "pumping" of moist from the surrounding plains. Such meso-scale circulations contribute to reinforce by convergence the vertical velocity over the mountain slope, which are partly generated by thermal convection. This favors the deep convection and increased cloudiness and rainfall over the moutains, reducing the temperature anomaly. Finally in the coastal regions the land/sea contrast is increased in case of dry soil, favoring the sea-breeze circulation and moist cool marine air advection. This decreases the temperature anomaly down by 20% along a narrow Mediterranean land band. Soil dryness can thus produce cooling effect in situation of heat waves over mountainous and some coastal regions.

The chapter 4 takes advantage of the MORCE platform and WRF/ORCHIDEE coupling for investigating two-way interactions of vegetation and climate on regional scales. Several simulations were carried out. Two integrations over 2002-2003 constitute the first set, one has a freely evolving phenology whereas the other a prescribed phenology corresponding to the year 2002. Under favorable meteorological conditions the agricultural vegetation grows early and quickly in the coupled simulation. Excess vegetation rapidly deplets the soil moisture content, which in turn leads to crop senescence through water limitation and brings about a switch in evapotranspiration regime from energy to soil moisture limited. This situation is not observed with the uncoupled simulation. In 2003 apart from the soil moisture-temperature feedback, a vegetation feedback (through the interactive phenology) contributes to damp the temperature anomaly of June heat wave and amplify the temperature anomalies in August. The spatial pattern of the heat wave response was ecosystem-dependent and most significant for croplands. While forested areas allow for a conservative use of water, croplands are reduced under drought and heat wave conditions. The differences observed between crop and forested areas are in line with the satellite observations reported by *Zaitchik et al.* (2006). Temperature changes can locally reach 2.5°C, corresponding to a modulation of 20% for an average climatic temperature anomaly. As regards to previous results (*Fischer et al.*, 2007b) which estimated the drought contribution to 40% of the temperature anomaly, heatwave modelling has to take into account an interactive phenology. This coupling already emphasizes that vegetation-atmosphere interactions are a major component of the spatial pattern of an extreme event.

Events similar to the 2003 mega heat wave will be likely more frequent, intense and longer by the end of the 21st century owing to enhanced atmospheric greenhouse-gas concentrations (*Beniston*, 2004; *Schär et al.*, 2004). Although the biogeophysical effect of land cover change seems able to partially or totally compensate the biogeochemical impact of increased greenhouse-gas (*Findell et al.*, 2007; *Jackson et al.*,

2008; *Pitman*, 2009). So far studies conducted in the Mediterranean have contradictory results (cooling or warming) (*Heck et al.*, 2001; *Gaertner et al.*, 2001; *Anav et al.*, 2010a). With the help of the modelling platform MORCE, the impact of a potential vegetation on the 2003 summer heat waves is compared with the impact of the existing vegetation. The differences in vegetation cover is related to the conversion of agricultural land use to natural grassland and forest. By replacing the agricultural vegetation by a mixture of forests and pastures, the mean capacity of photosynthetic activity is reduced due to increased stomatal resistance and smaller LAI, which results in reduced transpiration. The hydrological cycle effects take over those modifying the radiative budget and the simulation without agricultural land cover plays out its advantage of greater heat resilience on the long term damping the daily maximal temperatures on average during the second heat wave which happened in August.

5.2 Perspectives

This thesis is divided into two parts addressing distinct issues. Part one of the paper focused on the influence of drought, water cycle and mesoscale processes on heat waves. The second part investigated the impact of interactive vegetation (i.e. phenology) and land cover change on heat waves. Hereafter I propose several broad categories of perspectives which draw on scientific and technical advances from this thesis. Several developments within the MORCE platform are considered to improve the simulation of regional climate by providing a better description of the land surface.

In depth investigation of heat waves clusters

The classification I have presented in section 3.1.2 associates heat waves with different physical mechanisms. Some of these I have identified in Western Europe, such as the drought and heat advection from the Mediterranean throughout the Europe (*Vautard et al.*, 2007; *Zampieri et al.*, 2009; *Stéfanon et al.*, 2012a). The Eastern Europe heat waves are sensitive to the Mediterranean drought, with a very striking rainfall anomaly structure south of heat waves cluster and located south of the Carpates; a range of mountains forming an arc roughly 1,500 km long across Central and Eastern Europe from west to east and where the highest peaks exceed 2,600 m. Consequently one might wonder whether the dryness of air mass can be increased by orographic effect as south foehn. In those cases modelling experiment could lead to a better understanding of such events, and could rely on HyMeX/Med-Cordex simulations for the ERA-Interim period (1989-2008).

Other preconditionning processes remain to be clarified as for example in Northern Europe. The proxy used in my works (frequency of rainy events) may not be relevant for high latitudes. In boreal areas the memory properties are more likely represented by the snow cover, considering snow melt or snow mass could be more efficient.

Hydrological extremes and water management

Within the MORCE platform some of the ORCHIDEE functionalities have not been implemented yet. River routing and multi-layer soil (based on CWRR[1] hydrology) are already available in the stand-alone model. Developing a routing scheme significantly improves the simulated land water storage (*Ngo-Duc*

[1] Center for Water Resources Research

et al., 2007) while CWRR hydrology compared to Choisnel scheme provides a better mean annual cycle and inter-annual variability (*d'Orgeval et al.*, 2008). Their integration within MORCE could provide an improvement of the continental water cycle representation

The main focus of the analysis would be to reveal how the coupling with the atmosphere modifies the simulated amplitude of the extremes such as droughts and floods, and identifies the weaknesses where model development is most urgently needed in order to achieve a realistic representation of hydrological extremes. Soil moisture, vegetation state and river discharge will be used as indicators and compared with reanalysis of land-surface properties and river runoffs obtained by satellite observations.

Water management is facing major challenges given that the Mediterranean region undergoes fast socio-economic changes and is influenced by environmental changes. Water scarcity, environmental issue, global warming and increasing populationn the altogether question the future sustainibility in water resources (*Iglesias et al.*, 2007). It could be subjected to investigation through the integration of irrigation and routing scheme, in order to measure the impact of anthropogenic pressures on the hydrological systems and the continental water budget of the Mediterranean region.

Biosphere-atmosphere interactions

The dynamical global vegetation model ORCHIDEE has been developed for global scale application in the IPSL global Earth system model. Consequently it has been designed to represent biogeochemical and biophysical processes of the major ecosystems on a global scale. The coarse resolution simplifies a multitude of ecosystems into a few generic PFTs. For instance the representation of the world's croplands in ORCHIDEE relies on two PFTs C_3 and C_4 corresponding to two disctinct carbon assimilation mode. However agronomists and ecologists developed growth models calibrated for one crop or tree family, obviously better suited for representing these plants than PFTs (*Dufrêne et al.*, 2005). On a regional or local scale, there is no such a need for a generalist approach and the potential use of growth models is more relevant. The managed lands, crops cover and grasslands which represent 35% and 30-40% in the Mediterranean area respectively, are highly sensitive to water stress (*Katerji et al.*, 2008) and this feature is particularly difficult to model (*Gervois et al.*, 2004; *Smith et al.*, 2010). Improving the current PFTs parameterization by implementing applied plant growth models could provide a more realistic vegetation feedback and more fully assess the mesoscale variability of droughts and heat waves.

One aspect that has not been addressed is the role of the atmospheric chemistry (e.g. ozone) which has also a direct effect on plant stomatal structure (*Anav et al.*, 2011). Indeed, summer heat waves are associated with high insolation and low cloudiness. In nearby urban areas, these conditions are also favorable to strong pollution levels, with especially high ozone concentration. Future work could investigate the additional effect of the severe pollution episode of August 2003 on the temperature anomaly during the summer heat wave.

Land cover change strategies in the context of global change

The impacts of land cover change on the heat waves of the summer of 2003 have been investigated in section 4.2. Significant modifications in the local temperatures and hydrological cycles have been observed. In addition to these results, a significant difference for the winter precipitation on local scales was found, presenting a contrasting outcome compared to the results presented by other authors. Theses differences

can reach 24% of the average annual precipitation. This is especially remarkable as precipitations in winter months are mostly dominated by large-scale patterns and to a much lesser extent by the surface characteristics which is why other studies reported to observe no or no significant changes (*Dümenil Gates and Ließ*, 2001; *Heck et al.*, 2001; *Pitman*, 2009). It might be possible that the changes in surface roughness associated with orographic effects, modify the surface wind module and enhance advected precipitation in the orographic region. However, the exact mechanisms involved are not clear yet and need further investigation. Moreover, it would be interesting to compare the way humans suffer from heat waves in different environments. Human heat indices are used to initiate public health responses and propose to take into account different parameters which affect human well-being as temperature, relative humidity and wind speed for example.

Bibliography

Adcroft, A. J., C. N. Hill, and J. C. Marshall, A new treatment of the coriolis terms in c-grid models at both high and low resolutions, *Mon. Wea. Rev*, *127*, 1928–1936, 1999.

Anav, A., P. M. Ruti, V. Artale, and R. Valentini, Modelling the effects of land-cover changes on surface climate in the mediterranean region, *Clim. Res.*, *41*, 91–104, 2010a.

Anav, A., F. D'Andrea, N. Viovy, and N. Vuichard, A validation of heat and carbon fluxes from high-resolution land surface and regional models, *J. Geophys. Res.*, *115*, G04,016, doi:10.1029/2009JG001178, 2010b.

Anav, A., L. Menut, D. Khvorostyanov, and N. Viovy, Impact of tropospheric ozone on the euro-mediterranean vegetation, *Global Change Biology*, *17*, 2342–2359, 2011.

Arakawa, A., and V. R. Lamb, *Computational design of the basic numerical processes of the UCLA general circulation model*, pp. 174–267, Academic Press, 1977.

Baldi, M., G. Dalu, G. Maracchi, M. Pasqui, and F. Cesarone, Heat waves in the mediterranean: a local feature or a larger-scale effect?, *Int. J. Climatol.*, *26*, 1477–1487, doi:10.1002/joc.1389, 2006.

Ball, J. T., A model predicting stomatal conductance and its contribution to the control of photosynthesis under different environmental conditions, *Prog. Photosynthesis Res. Proc. Int. Congress 7th, Providence. 10-15 Aug 1986. Vol4. Kluwer, Boston.*, pp. 221–224, 1987.

Barriopedro, D., E. M. Fischer, J. Luterbacher, R. M. Trigo, and R. Garcia-Herrera, The hot summer of 2010: Redrawing the temperature record map of europe, *Science*, *332*, 220–224, 2011.

Bastin, S., and P. Drobinski, Temperature and wind velocity oscillations along a gentle slope during sea-breeze events, *Boundary-Layer Meteorology*, *114*, 573–594, 2005.

Bastin, S., and P. Drobinski, Sea-breeze-induced mass transport over complex terrain in south-eastern france: A case-study, *Quart. J. Roy. Meteorol. Soc.*, *132*, 405–423, 2006.

Bastin, S., P. Drobinski, A. Dabas, P. Delville, O. Reitebuch, and C. Werner, Impact of the rhône and durance valleys on sea-breeze circulation in the marseille area, *Atmos. Res.*, *74*, 303–328, 2005.

Bastin, S., C. Champollion, O. Bock, P. Drobinski, and F. Masson, Diurnal cycle of water vapor as documented by a dense gps network in a coastal area during escompte-iop2, *J. Appl. Meteorol. Climatol.*, *46*, 167–182, 2007.

Bechtold, P., E. Bazile, F. Guichard, P. Mascart, and E. Richard, A mass-flux convection scheme for regional and global models, *Quart. J. Roy. Meteorol. Soc.*, *127*, 869–886, 2001.

Beljaars, A., P. Viterbo, M. Miller, and A. Betts, The anomalous rainfall over the united states during july 1993: Sensitivity to land surface parameterization and soil moisture anomalies, *Mon. Wea. Rev.*, *124*, 362–383, 1996.

Beniston, M., The 2003 heat wave in europe: a shape of things to come ? an analysis based on swiss climatological data and model simulations, *Geophys. Res. Lett.*, *31*, L02,202, doi:10.1029/2003GL018857, 2004.

Besancenot, J. P., Vagues de chaleur et mortalité dans les grandes agglomérations urbaines, *Environ Risques Santé*, *1*, 229–240, 2002.

Betts, A. K., J. H. Ball, A. C. M. Beljaars, M. J. Miller, and P. A. Viterbo, The land surface-atmosphere interaction: A review based on observational and global modeling perspectives, *J. Geophys. Res.*, *101*, 7209–7225, 1996.

Black, E., and R. Sutton, The influence of oceanic conditions on the hot european summer of 2003, *Clim. Dynam.*, *28*, 53–66, 2007.

Black, E., M. Blackburn, G. Harrison, B. Hoskins, and J. Methven, Factors contributing to the summer 2003 european heatwave, *Weather*, *59*, 218–223, 2004.

Bleck, R., and S. G. Benjamin, Regional weather prediction with a model combining terrain-following and isentropic coordinates. i: Model description, *Mon. Wea. Rev.*, *121*, 1770–1785, 1993.

Blyth, E. M., A. J. Dolman, and J. Noilhan, The effect of forest on mesoscale rainfall: an example from HAPEX-MOBILHY, *Journal of applied meteorology*, *33*(4), 445–454, 1994.

Bonan, G. B., Effects of land use on the climate of the united states, *Climatic Change*, *37*, 449–486, 1997.

Bonan, G. B., S. Levis, S. Sitch, M. Vertenstein, and K. W. Oleson, A dynamic global vegetation model for use with climate models: Concept and description of simulated vegetation dynamics,, *Global Change Biol.*, *9*, 1543–1566, 2003.

Bounoua, L., S. O. Collatz, G Jand Los, P. J. Sellers, D. A. Dazlich, C. J. Tucher, and D. A. Randall, Sensitivity of climate to changes in ndvi, *J. Climate*, *13*, 2277–2292, 2000.

Budyko, M. I., *Climate and Life*, 608 pp., Academic Press, 1974.

Cassou, C., Intraseasonal interaction between the madden–julian oscillation and the north atlantic oscillation, *Nature*, *455*, 523–527, 2008.

Cassou, C., L. Terray, and A. S. Phillips, Tropical atlantic influence on european heatwaves, *J. Climate*, *18*, 2805–2811, 2005.

Chagnon, F. J. F., R. L. Bras, and J. Wang, Climatic shift in patterns of shallow clouds over the amazon, *Geophys. Res. Lett.*, *31*, 1183–1199, 2004.

Chalita, S., and H. Treut, The albedo of temperate and boreal forest and the northern hemisphere climate: a sensitivity experiment using the lmd gcm, *Climate Dynamics*, *10*, 231–240, 1994.

Chen, F., and J. Dudhia, Coupling an advanced land surface–hydrology model with the penn state–ncar mm5 modeling system. part i: Model implementation and sensitivity, *Mon. Weather Rev.*, *129*, 569–585, 2001.

Cheng, X., and J. M. Wallace, Cluster analysis of the northern hemisphere wintertime 500-hpa height field: spatial patterns, *J. Atmos. Sci.*, *50*, 2674–2696, 1993.

Choisnel, E., S. V. Jourdain, and C. J. Jacquart, Climatological evaluation of some fluxes of the surface energy and soil water balances over france, *Annales Geophysicae*, *13*, 666–674, 1995.

Christensen, J. H., and O. B. Christensen, Severe summertime flooding in europe, *Nature*, *421*, 805–806, 2003.

Ciais, P., M. Reichstein, N. Viovy, A. Granier, J. Ogée, V. Allard, M. Aubinet, N. Buchmann, C. Bernhofer, A. Carrara, F. Chevallier, N. De Noblet, A. D. Friend, P. Friedlingstein, T. Grunwald, B. Heinesch, P. Keronen, A. Knohl, G. Krinner, D. Loustau, G. Manca, G. Matteucci, F. Miglietta, J. M. Ourcival, D. Papale, K. Pilegaard, S. Rambal, G. Seufert, J. F. Soussana, M. J. Sanz, E. D. Shulze, T. Vesala, and R. Valentini, Europe-wide reduction in the primary productivity caused by the heat and drought in 2003, *Nature*, *437*, 529–533, 2005.

Clark, D. B., C. M. Taylor, and A. J. Thorpe, Feedback between the land surface and rainfall at convective length scales, *J. Hydrometeor*, *5*, 625–639, 2004.

Colacino, M., and M. Conte, Heat waves in the central mediterranean. a synoptic climatology, *Nuovo Cimento*, *18*, 295–304, 1995.

Collatz, G. J., J. T. Ball, C. Grivet, and J. A. Berry, Physiological and environmental regulation of stomatal conductance, photosynthesis and transpiration: a model that includes a laminar boundary layer, *Agr Forest Meteorol*, *54*, 107–136, 1991.

Cony, M., L. Martín, E. Hernández, and T. del Teso, Synoptic patterns that contribute to extremely hot days in Europe, *Atmósfera*, *23*, 295 – 306, 2010.

COPA-COGECA, Assessment of the impact of the heat wave and drought of the summer 2003 on agriculture and forestry, *Tech. rep.*, Committee of professional agricultural organisations in the European union-general confederation of agricultural co-operatives in the European Union, 2003.

Crétat, J., B. Pohl, Y. Richard, and P. Drobinski, Uncertainties in simulating regional climate of southern africa: sensitivity to physical parameterizations using wrf, *38*, 613–634, 2012.

da Rocha, H. R., M. L. Goulden, S. D. Miller, M. C. Menton, L. D. V. O. Pinto, H. C. de Frietas, and S. F. A. M, Seasonality of water and heat fluxes over a tropical forest in eastern amazonia, *Ecol. Appl.*, *14*, S22–S32, 2004.

Dai, A., I. Y. Fung, and A. Del Genio, Surface observed global land precipitation variations during 1900–88, *J. Climate*, *10*, 2943–2962, 1997.

D'Andrea, F., A. Provenzale, R. Vautard, and N. De Noblet-Decoudré, Hot and cool summers: Multiple equlibria of the continental water cycle, *Geophys. Res. Lett.*, *33*, L24,807, 2006.

Davis, R. E., D. Knight, D. Hondula, and P. C. Knappenberger, A comparison of biometeorological comfort indices and human mortality during heat waves in the united states, p. 10, 2006.

De Noblet-Ducoudré, N., personal communication, 2012.

De Rosnay, P., and J. Polcher, Modeling root water uptake in a complex land surface scheme coupled to a gcm, *Hydrol. Earth Sys. Sci.*, *2*, 239–256, 1998.

De Rosnay, P., J. Polcher, K. Laval, and M. Sabre, Integrated parameterization of irrigation in the land surface model ORCHIDEE. Validation over Indian Peninsula, *Geophysical Research Letters*, *30*, 1986, doi:10.1029/2003GL018024, 2003.

Dee, D. P., S. M. Uppala, A. J. Simmons, P. Berrisford, P. Poli, S. Kobayashi, U. Andrae, M. A. Balmaseda, G. Balsamo, P. Bauer, P. Bechtold, A. C. M. Beljaars, L. van de Berg, J. Bidlot, N. Bormann, C. Delsol, R. Dragani, M. Fuentes, A. J. Geer, L. Haimberger, S. B. Healy, H. Hersbach, E. V. Hólm, L. Isaksen, P. Kållberg, M. Köhler, M. Matricardi, A. P. McNally, B. M. Monge-Sanz, J.-J. Morcrette, B.-K. Park, C. Peubey, P. de Rosnay, C. Tavolato, J.-N. Thépaut, and F. Vitart, The era-interim reanalysis: configuration and performance of the data assimilation system, *Quart. J. Roy. Meteorol. Soc.*, *137*, 553–597, 2011.

Della-Marta, P. M., M. R. Haylock, J. Luterbacher, and H. Wanner, Doubled length of western european summer heat waves since 1880, *J. Geophys. Res*, *112*, D15,103, doi:10.1029/2007JD008510, 2007.

Dirmeyer, P. A., X. Gao, M. Zhao, Z. Guo, T. Oki, and N. Hanasaki, Gswp-2: Multimodel analysis and implications for our perception of the land surface, *Bull. Amer. Meteorol. Soc.*, *87*, 1381–1397, 2006.

Done, J., C. A. Davis, and M. Weisman, The next generation of nwp: explicit forecasts of convection using the weather research and forecasting (wrf) model, *Atmospheric Science Letters*, *5*(6), 110–117, 2004.

d'Orgeval, T., J. Polcher, and P. de Rosnay, Sensitivity of the west african hydrological cycle in orchidee to infiltration processes, *Hydrol. Earth Syst. Sci.*, *12*, 1387–1401, 2008.

Douville, H., and F. Chauvin, Relevance of soil moisture for seasonal climate predictions: a preliminary study, *Climate Dynamics*, *16*, 719–736, 2000.

Drobinski, P., and T. Dubos, Linear breeze scaling: From large-scale land/sea-breezes to mesoscale inland breezes, *Q. J. R. Meteorol. Soc.*, *135*, 1766–1775, 2009.

Drobinski, P., C. Flamant, J. Dusek, P. Flamant, and J. Pelon, Observational evidence and modeling of an internal hydraulic jump at the atmospheric boundary layer top during a tramontane event, *Boundary Layer Meteorol.*, *98*, 497–515, 2001.

Drobinski, P., S. Bastin, V. Guénard, J. Caccia, A. M. Dabas, P. Delville, A. Protat, O. Reitebuch, and C. Werner, Summer mistral at the exit of the rhône valley, *Q. J. R. Meteorol. Soc.*, *131*, 353–375, 2005.

Drobinski, P., S. Bastin, A. Dabas, P. Delville, and O. Reitebuch, Variability of three-dimensional sea breeze structure in southern france: observations and evaluation of empirical scaling laws, *Ann. Geophys.*, *24*, 1783–1799, 2006.

Drobinski, P., V. Ducrocq, P. Lionello, and the HyMeX ISSC, Hymex, a potential new ceop rhp in the mediterranean basin, *GEWEX newsletter*, *19*, 5–6, 2009.

Drobinski, P., V. Ducrocq, and P. Lionello, Studying the hydrological cycle in the mediterranean, *Trans. Am. Geophys. Union (EOS)*, *91*, 373, 2010.

Drobinski, P., A. Anav, C. Lebeaupin Brossier, G. Samson, M. Stéfanon, S. Bastin, M. Baklouti, K. Béranger, J. Beuvier, R. Bourdallé-Badie, L. Coquart, F. D'Andrea, N. De Noblet-Ducoudré, F. Diaz, J. C. Dutay, C. Ethe, A. M. Foujols, D. Khvorostyanov, G. Madec, M. Mancip, S. Masson, L. Menut, J. Palmieri, J. Polcher, S. Turquety, S. Valcke, and N. Viovy, Model of the regional coupled earth system (morce): application to process and climate studies in vulnerable regions, *Environ. Model. Soft*, *35*, 1–18, 2012.

Ducoudré, N., K. Laval, and A. Perrier, Sechiba, a new set of parametrizations of the hydrologic exchanges at the land/atmosphere interface within the lmd atmospheric general circulation model, *J. Clim.*, *6*, 248–273, 1993.

Dudhia, J., Numerical study of convection observed during the winter monsoon experiment using a mesoscale two-dimensional model, *J. Atmos. Sci.*, *46*, 3077–3107, 1989.

Dufrêne, E., H. Davi, C. François, G. le Maire, V. L. Dantec, and A. Granier, Modelling carbon and water cycles in a beech forest: Part i: Model description and uncertainty analysis on modelled nee, *Ecological Modelling*, *185*(2-4), 407–436, 2005.

Dümenil Gates, L., and S. Ließ, Impacts of deforestation and afforestation in the mediterranean region as simulated by the MPI atmospheric GCM, *Global and Planetary Change*, *30*, 309–328, 2001.

Easterling, D. R., G. A. Meehl, C. Parmesan, S. A. Changnon, T. R. Karl, and M. L. O, Climate extremes: Observations, modeling, and impacts, *Science*, *289*, 2068–2074, 2000.

Eckel, T., Perturbing mm5 moisture availability for ensemble forecasting, *Tech. rep.*, University of Washington, 2002.

Ellis, F. H., H. Prince, G. Lovatt, and R. Whittington, Mortality and morbidity in birmingham during the 1976 heat wave, *Quarterly journal of medicine*, *49*, 1–8, 1980.

Eltahir, E. A. B., A soil moisture rainfall feedback mechanism 1. theory and observations, *Water Resour. Res.*, *34*, 765–776, 1998.

Farquhar, G. D., S. Caemmerer, and J. A. Berry, A biochemical model of photosynthetic co2 assimilation in leaves of c3 species, *Planta*, *149*, 78–90, 1980.

Ferranti, L., and P. Viterbo, The european summer of 2003: Sensitivity to soil water initial conditions, *J. Climate*, *19*, 3659–3680, 2006.

Feudale, L., and J. Shukla, Influence of sea surface temperature on the european heat wave of 2003 summer. part i: an observational study, *Clim. Dynam.*, *36*, 1691–1703, 2010.

Filleul, L., S. Cassadou, S. Médina, P. Fabres, A. Lefranc, D. Eilstein, A. Le Tertre, L. Pascal, B. Chardon, M. Blanchard, C. Declercq, J.-F. Jusot, H. Prouvost, and M. Ledrans, The relation between temperature, ozone, and mortality in nine french cities during the heat wave of 2003, *Environ Health Perspect.*, *114*, 1344–1347, 2006.

Findell, K. L., E. Shevliakova, P. C. D. Milly, and R. J. Stouffer, Modeled impact of anthropogenic land cover change on climate, *J. Climate*, *20*, 3621–3634, 2007.

Findell, K. L., P. Gentine, B. R. Lintner, and C. Kerr, Probability of afternoon precipitation in eastern united states and mexico enhanced by high evaporation, *Nature Geoscience*, *4*, 434–439, 2011.

Fink, A. H., T. Bruecher, G. C. Leckebusch, A. Krueger, J. G. Pinto, and U. Ulbrich, The 2003 european summer heatwaves and drought - synopstic diagnosis and impacts, *Weather*, *59*, 209–216, 2004.

Fischer, E. M., S. I. Seneviratne, D. Lüthi, and C. Schär, Contribution of land-atmosphere coupling to recent European summer heat waves, *Geophysical Research Letters*, *34*, L06,707, doi: 10.1029/2006GL029068, 2007a.

Fischer, E. M., S. I. Seneviratne, P. L. Vidale, D. Lüthi, and C. Schär, Soil moisture–atmosphere interactions during the 2003 european summer heat wave, *J. Clim.*, *20*, 5081–5099, 2007b.

Flaounas, E., S. Bastin, and S. Janicot, Regional climate modelling of the 2006 west african monsoon: sensitivity to convection and planetary boundary layer parameterisation using wrf, *36*, 1083–1105, 2010.

Flaounas, E., P. Drobinski, M. Vrac, S. Bastin, C. Lebeaupin-Brossier, M. Stéfanon, M. Borga, and J.-C. Calvet, Precipitation and temperature space-time variability and extremes in the mediterranean region: Evaluation of dynamical and statistical downscaling methods, *Clim. Dynam.*, pp. –, doi:underpress., 2012.

Foley, J., S. Levis, I. C. Prentice, D. Pollard, and S. Thompson, Coupling dynamic models of climate and vegetation, *Global Change Biol.*, *4*, 561–579, 1998.

Forster, P., V. Ramaswamy, P. Artaxo, T. Berntsen, R. Betts, D. Fahey, J. Haywood, J. Lean, D. Lowe, G. Myhre, and et al, *Radiative forcing of climate change Climate Change 2007: The Physical Science Basis. Contribution of Working Group I to the Fourth Assessment Report of the Intergovernmental Panel on Climate Change*, 129–234 pp., Cambridge University Press, 2007.

Fouillet, A., G. Rey, F. Laurent, G. Pavillon, S. Bellec, C. Guihenneuc-Jouyaux, J. Clavel, E. Jougla, and D. Hémon, Excess mortality related to the august 2003 heat wave in france, *International Archives of Occupational and Environmental Health*, *80*, 16–24, 2006.

Fouillet, A., G. Rey, V. Wagner, K. Laaidi, P. Empereur-Bissonnet, A. Le Tertre, P. Frayssinet, P. Bessemoulin, F. Laurent, P. De Crouy-Chanel, E. Jougla, and H. D, Has the impact of heat waves on mortality changed in france since the european heat wave of summer 2003 ? a study of the 2006 heat wave, *Int. J. Epidemiol.*, *37*, 309–317, 2008.

Gaertner, M. A., O. B. Christensen, J. A. Prego, J. Polcher, C. Gallardo, and M. Castro, The impact of deforestation on the hydrological cycle in the western mediterranean: an ensemble study with two regional climate models, *Clim. Dyn.*, *17*, 857–873, 2001.

Garcia-Herrera, R., J. Diaz, R. M. Trigo, and E. Hernández, Extreme summer temperatures in iberia: health impacts and associated synoptic conditions, *Ann. Geophys.*, *23*, 239–251, 2005.

Gervois, S., N. de Noblet-Ducoudré, N. Viovy, P. Ciais, N. Brisson, B. Seguin, and A. Perrier, Including croplands in a global biosphere model: Methodology and evaluation at specific sites, *Earth Interact.*, *8*, 1–25, 2004.

Giorgi, F., Climate change hot-spots, *Geophys. Res. Lett.*, *33*, L08,707, doi:10.1029/2006GL025734, 1996.

Giorgi, F., C. Jones, and G. R. Asrar, Addressing climate information needs at the regional level: the cordex framework, *WMO Bulletin*, *58*, 175–183, 2009.

Gobron, N., B. Pinty, F. Mélin, M. Taberner, M. M. Verstraete, A. Belward, T. Lavergne, and J.-L. Widlowski, The state of vegetation in europe following the 2003 drought, *International Journal of Remote Sensing*, *26*, 2013–2020, 2005.

Granier, A., M. Reichstein, N. BrÃ©da, I. Janssens, E. Falge, P. Ciais, T. GrÃŒnwald, M. Aubinet, P. Berbigier, C. Bernhofer, N. Buchmann, O. Facini, G. Grassi, B. Heinesch, H. Ilvesniemi, P. Keronen, A. Knohl, B. KÃ¶stner, F. Lagergren, A. Lindroth, B. Longdoz, D. Loustau, J. Mateus, L. Montagnani, C. Nys, E. Moors, D. Papale, M. Peiffer, K. Pilegaard, G. Pita, J. Pumpanen, S. Rambal, C. Rebmann, A. Rodrigues, G. Seufert, J. Tenhunen, T. Vesala, and Q. Wang, Evidence for soil water control on carbon and water dynamics in european forests during the extremely dry year: 2003, *Agricultural and Forest Meteorology*, *143*(1-2), 123–145, 2007.

Guénard, V., P. Drobinski, J. Caccia, B. Campistron, and B. Bénech, An observational study of the mesoscale mistral dynamics, *Boundary Layer Meteorol.*, *115*, 263–288, 2005.

Guénard, V., P. Drobinski, J. Caccia, G. Tedeschi, and P. Currier, Dynamics of the map iop-15 severe mistral event: Observations and high-resolution numerical simulations, *Q. J. R. Meteorol. Soc.*, *132*, 757–778, 2006.

Guichard, F., J. C. Petch, J.-L. Redelsperger, P. Bechtold, J.-P. Chaboureau, S. Cheinet, W. Grabowski, H. Grenier, C. G. Jones, M. Köhler, J.-M. Piriou, R. Tailleux, and M. Tomasini, Modelling the diurnal cycle of deep precipitating convection over land with cloud-resolving models and single-column models, *Quart. J. Roy. Meteorol. Soc.*, *130*, 3139–3172, 2004.

Guillevic, P., R. D. Koster, M. J. Suarez, L. Bounoua, G. J. Collatz, S. O. Los, and S. P. P. Mahanama, Influence of the interannual variability of vegetation on the surface energy balance–a global sensitivity study, *J. Hydrometeorol.*, *3*, 617–629, 2002.

Haylock, M. R., N. Hofstra, A. M. G. Klein Tank, E. J. Klok, P. D. Jones, and M. New, A european daily high-resolution gridded data set of surface temperature and precipitation for 1950-2006, *J. Geophys. Res.*, *113*, D20,119, 2008.

Heck, P., D. Lüthi, H. Wernli, and C. Schär, Climate impacts of european-scale anthropogenic vegetation changes: A sensitivity study using a regional climate model, *J. Geophys. Res.*, *106*, 7817–7835, 2001.

Hémon, D., and E. Jougla, Surmortalité liée à la canicule d'août 2003, *Tech. rep.*, INSERM, Paris, 2003.

Hohenegger, C., P. Brockhaus, C. S. Bretherton, and C. Schär, The soil moisture–precipitation feedback in simulations with explicit and parameterized convection, *22*, 5003–5020, 2009.

Hong, S. Y., J. Dudhia, and S.-H. Chen, A revised approach to ice microphysical processes for the bulk parameterization of clouds and precipitation, *Mon. Wea. Rev.*, *132*, 103–120, 2004.

Hourdin, F., I. Musat, S. Bony, P. Braconnot, F. Codron, J.-L. Dufresne, L. Fairhead, M.-A. Filiberti, P. Friedlingstein, J.-Y. Grandpeix, G. Krinner, P. LeVan, Z.-X. Li, and F. Lott, The lmdz4 general circulation model: climate performance and sensitivity to parametrized physics with emphasis on tropical convection, *Clim. Dynam.*, *27*, 787–813, 2006.

Huang, J., and H. M. Van Den Dool, Monthly precipitation-temperature relations and temperature prediction over the united states, *J. Climate*, *6*, 1111–1132, 1992.

Hurrell, J. W., Y. Kushnir, G. Ottersen, and M. Visbeck, *The North Atlantic Oscillation: Climate Significance and Environmental Impact*, vol. 134, impact. geophys. monogr. ed., 279 pp., Amer. Geophys. Union, 2003.

Iglesias, A., L. Garrote, F. Flores, and M. Moneo, Challenges to manage the risk of water scarcity and climate change in the mediterranean, *Water Resources Management*, *21*, 775–788, 2007.

Jackson, R. B., J. T. Randerson, J. G. Canadell, R. G. Anderson, R. Avissar, D. D. Baldocchi, G. B. Bonan, K. Caldeira, N. S. Diffenbaugh, C. B. Field, B. A. Hungate, E. G. Jobbágy, L. M. Kueppers, M. D. Nosetto, and D. E. Pataki, Protecting climate with forests, *Environmental Research Letters*, *3*(4), 044,006, 2008.

Jolly, W. M., M. Dobbertin, N. E. Zimmermann, and M. Reichstein, Divergent vegetation growth responses to the 2003 heat wave in the swiss alps, *Geophys. Res. Lett.*, *32*, L18,409, doi:10.1029/2005GL023252, 2005.

Jung, M., M. Vetter, M. Herold, G. Churkina, M. Reichstein, S. Zaehle, P. Ciais, N. Viovy, A. Bondeau, Y. Chen, K. Trusilova, F. Feser, and M. Heimann, Uncertainties of modeling gross primary productivity over europe: A systematic study on the effects of using different drivers and terrestrial biosphere models, *Global Biogeochem Cy*, *21*, GB4021, doi:10.1029/2006GB002915, 2007.

Kain, J. S., The kain-fritsch convective parameterization: An update, *J. Appl. Meteorol.*, *43*, 170–181, 2004.

Kalnay, E., and et al, The ncep/ncar 40-year reanalysis project, *Bull. Amer. Meteorol. Soc.*, *77*, 437–471, 1996.

Katerji, N., M. Mastrorilli, and G. Rana, Water use efficiency of crops cultivated in the mediterranean region: Review and analysis, *Eur. J. Agronomy*, *28*, 493–507, 2008.

Kaufmann, R. K., L. Zhou, R. B. Myneni, C. J. Tucker, D. Slayback, N. V. Shabanov, and P. J, The effect of vegetation on surface temperature: A statistical analysis of ndvi and climate data, *Geophys. Res. Lett.*, *30*, 2147, doi:10.1029/2003GL018251, 2003.

Keenan, T., R. García, A. D. Friend, S. Zaehle, C. Gracia, and S. Sabate, Improved understanding of drought controls on seasonal variation in mediterranean forest canopy co_2 and water fluxes through combined in situ measurements and ecosystem modelling, *Biogeosciences*, *6*, 1423–1444, 2009.

Klein Tank, A. M. G., and G. P. Konnen, Trends in indices if daily temperature and precipitation extremes in europe, *J. Climate*, *16*, 3665–3680, 2003.

Klein Tank, A. M. G., G. P. Konnen, and S. F. M, Signals of anthropogenic influence on european warming as seen in the trend patterns of daily temperature variance, *Int. J. Climatol.*, *25*, 1–16, 2005.

Köppen, W., Das geographisca system der klimate, *Handbuch der Klimatologie*, *25*, 1–44, 1936.

Koster, e. a., R.D., Regions of strong coupling between soil moisture and precipitation, *Science*, *305*, 1138–1140, 2004.

Kovats, R. S., S. Hajat, and P. Wilkinson, Contrasting patterns of mortality and hospital admissions during hot weather and heat waves in greater london, uk, *Occup Environ Med*, *61*, 893–898, 2004.

Krinner, G., N. Viovy, N. de Noblet-Ducoudré, J. Ogeé, J. Polcher, P. Friedlingstein, P. Ciais, S. Sitch, and I. Colin Prentice, A dynamic global vegetation model for studies of the coupled atmosphere-biosphere system, *Global Biogeochem Cy*, *19*, GB1015, doi:10.1029/2003GB002199, 2005.

Laaidi, K., M. Lendrans, M. Pascal, P. Empereur-Bissonnet, A. Le Tertre, S. Medina, C. Caserio, and P. Beaudeau, Système d'alerte canicule et santé, *Tech. rep.*, INVS, operational report, 2004.

Lavee, H., A. C. Imeson, and P. Sarah, The impact of climate change on geomorphology and desertification along a mediterranean-arid transect, *Land Degrad. Develop.*, *9*, 407–422, 1998.

Lean, J., and P. R. Rowntree, Understanding the sensitivity of a gcm simulation of amazonian deforestation to the specification of vegetation and soil characteristics, *J. Climate*, *10*, 1216–1235, 1997.

Levinson, D. H., and A. M. Waple, State of the climate in 2003, *Bull. Amer. Meteorol. Soc.*, *85*, S1–S72, 2004.

Loew, A., T. Holmes, and R. de Jeu, The European heat wave 2003: Early indicators from multisensoral microwave remote sensing?, *Journal of Geophysical Research*, *114*, D05,103, doi:10.1029/2008JD010533, 2009.

Lorenz, R., E. B. Jaeger, and S. I. Seneviratne, Persistence of heat waves and its link to soil moisture memory, *Geophys. Res. Lett.*, *37*, L09,703, doi:10.1029/2010GL042764, 2010.

Loveland, T. R., B. C. Reed, J. F. Brown, D. O. Ohlen, Z. Zhu, L. Yang, and J. W. Merchant, Development of a global land cover characteristics database and IGBP DISCover from 1 km AVHRR data, *International Journal of Remote Sensing*, *21*, 1303–1330, 2000.

Lu, L., and W. J. Shuttleworth, Incorporating ndvi-derived lai into the climate version of rams and its impact on regional climate, *J. Hydrometeorol.*, *3*, 347–362, 2002.

Luterbacher, J., D. Dietrich, E. Xoplaki, M. Grosjean, and H. Wanner, European seasonal and annual ttemperature variability, trends, and extremes since 1500, *Science*, *303*, 1499–1503, 2004.

Mahecha, M. D., M. Reichstein, M. Jung, S. I. Seneviratne, S. Zaehle, C. Beer, M. C. Braakhekke, N. Carvalhais, H. Lange, G. Le Maire, and E. Moors, Comparing observations and process-based simulations of biosphere-atmosphere exchanges on multiple timescales, *Journal of Geophysical Research*, *115*, G02,003+, doi:10.1029/2009JG001016, 2010.

Mahrt, L., and H. L. Pan, A two-layer model of soil hydrology, *Bound.-Layer Meteor.*, *29*, 1–20, 1984.

Matsueda, M., Predictability of euro-russian blocking in summer of 2010, *Geophys. Res. Lett.*, *38*, L06,801, doi:10.1029/2010GL046557, 2011.

Meehl, G. A., and C. Tebaldi, More intense, more frequent, and longer lasting heat waves in the 21st century, *Science*, *305*, 994–997, 2004.

Meissner, K. J., A. J. Weaver, H. D. Matthews, and P. M. Cox, The role of land surface dynamics in glacial inception: a study with the uvic earth system model, *Clim. Dyn.*, *21*, 515–537, 2003.

Michelangeli, P. A., R. Vautard, and L. B, Weather regimes: recurrence and quasi stationarity, *J. Atmos. Sci.*, *52*, 1237–1256, 1995.

Mlawer, E. J., S. J. Taubnam, P. D. Brown, I. M. J, and C. S. A, A validated correlated k-model for the longwave, *J. Geophys. Res.*, *102*, 1663–1682, 1997.

Monin, A. S., and A. M. Obukhov, Basic laws of turbulent mixing in the surface layer of the atmosphere, *Contrib. Geophys. Inst. Acad. Sci.*, *151*, 163–187, 1954.

Morales, P., M. T. Sykes, C. I. Prentice, P. Smith, B. Smith, H. Bugmann, B. Zierl, P. Friedlingstein, N. Viovy, S. Sabate, A. Sanchez, E. Pla, C. A. Gracia, S. Sitch, A. Arneth, and J. Ogee, Comparing and evaluating process-based ecosystem model predictions of carbon and water fluxes in major European forest biomes, *Global Change Biology*, *11*, 2211–2233, 2005.

Nakamura, M., T. Enomoto, and S. Yamane, A simulation study of the 2003 heatwave in europe, *Journal of the Earth Simulator*, *2*, 55–69, 2005.

Nau, J.-Y., L'impact de la canicule sur les vins du millésime 2003, *LE MONDE*, p. 2, 2004.

Nemani, R. R., C. D. Keeling, H. Hashimoto, W. M. Jolly, S. C. Piper, C. J. Tucker, R. B. Myneni, and R. S. W, Climate-driven increases in global terrestrial net primary production from 1982 to 1999, *Science*, *300*, 1560–1563, 2003.

Ngo-Duc, T., K. Laval, G. Ramillien, J. Polcher, and A. Cazenave, Validation of the land water storage simulated by organising carbon and hydrology in dynamic ecosystems (orchidee) with gravity recovery and climate experiment (grace) data, *Water Resour. Res.*, *43*, W04,427, 2007.

Noh, Y., W. G. Cheon, S.-Y. Hong, and S. Raasch, Improvement of the k-profile model for the planetary boundary layer based on large eddy simulation data, *Bound.-Lay. Meteorol.*, *107*, 401–427, 2003.

Ogi, M., K. Yamazaki, and Y. Tachibana, The summer northern annular mode and abnormal summer weather in 2003, *Geophys. Res. Lett.*, *32*, L04,706, doi:10.1029/2004GL021528, 2005.

Omrani, H., P. Drobinski, and T. Dubos, Spectral nudging in regional climate modelling: how strongly should we nudge?, *Q. J. Roy. Meteor. Soc.*, pp. n/a–n/a, doi:10.1002/qj.1894, 2012.

Pascal, M., K. Laaidi, M. Ledrans, E. Baffert, C. Caserio-Schönemann, A. Le Tertre, J. Manach, S. Medina, J. Rudant, and P. Empereur-Bissonnet, France's heat health watch warning system, *International Journal of Biometeorology*, *50*, 144–153, 2006.

Peel, M. C., B. L. Finlayson, and T. A. McMahon, Updated world map of the Köppen-geiger climate classification, *Hydrology and Earth System Sciences Discussions*, *4*, 439–473, 2007.

Philip, J. R., and D. A. de Vries, Moisture movement in porous materials under temperature gradients, *38*, 222–232, 1957.

Pielke, R., R. Avissar, M. Raupach, A. J. Dolman, X. Zhen, and A. S. Denning, Interactions between the atmosphere and terrestrial ecosystems: Influence on weather and climate, *Global Change Biol*, *4*, 461–475, 1990.

Pielke, R. A., Influence of the spatial distribution of vegetation and soils on the prediction of cumulus convective rainfall, *Rev. Geophys.*, *39*, 151–177, 2001.

Pielke, R. A., and R. Avissar, Influence of landscape structure on local and regional climate, *Landscape Ecology*, *4*, 133–155, 1990.

Pielke, R. A., A. Pitman, D. Niyogi, R. Mahmood, C. McAlpine, F. Hossain, K. K. Goldewijk, U. Nair, R. Betts, S. Fall, M. Reichstein, P. Kabat, and N. de Noblet, Land use/land cover changes and climate: modeling analysis and observational evidence, *Wiley Interdisciplinary Reviews: Climate Change*, *2*, 828–850, 2011.

Pitman, e. a., A J, Uncertainties in climate responses to past land cover change: First results from the lucid intercomparison study, *Geophys. Res. Lett.*, *36*, L14,814, doi:10.1029/2009GL039076, 2009.

Plaut, G., and E. Simmonnet, Large-scale circulation classification, wheather regimes, and local climate over france, the alps and western europe, *Clim.Res.*, *17*, 303–324, 2001.

Pleim, J. E., and A. Xiu, Development and testing of a surface flux and planetary boundary layer model for application in mesoscale models.influence of landscape structure on local and regional climate, *J.Appl.Meteor.*, *34*, 16–32, 1995.

Pleim, J. E., and A. Xiu, Development of a land surface model. part ii: Data assimilation, *J.Appl.Meteor.*, *42*, 1811–1822, 2003.

Polcher, J., B. McAvaney, P. Viterbo, M.-A. Gaertner, A. Hahmann, J.-F. Mahfou, J. Noilhan, T. Phillips, A. Pitman, C. A. Schlosser, J.-P. Schulz, B. Timbal, D. Verseghy, and Y. Xue, A proposal for a general interface between land surface schemes and general circulation models, *Global Planet Change*, *19*, 261–276, 1998.

Quesada, B., R. Vautard, P. Yiou, M. Hirschi, and S. I. Seneviratne, Asymmetric european summer heat predictability from wet and dry southern winters and springs, *Nature Clim. Change*, doi:10.1038/nclimate1536, 2012.

Räisänen, J., Co2-induced changes in interannual temperature and precipitation variability in 19 cmip2 experiments, *J. Climate*, *15*, 2395–2411, 2002.

Ray, D. K., U. S. Nair, R. M. Welch, Q. Han, J. Zeng, T. Su, W Kikuchi, and T. J. Lyons, Effects of land use in southwest australia: 1. observations of cumulus cloudiness and energy fluxes, *J. Geophys. Res.*, *108*, 355–357, 2003.

Raymond, D., and M. Wilkening, Mountain-Induced Convection under Fair Weather Conditions., *J. Atmos. Sci.*, *37*, 2693–2706, 1980.

Reichstein, M., P. Ciais, D. Papale, R. Valentini, S. Running, N. Viovy, W. Cramer, A. Granier, J. Ogée, V. Allard, M. Aubinet, B. Chr., N. Buchmann, A. Carrara, T. Grünwald, M. Heimann, B. Heinesch, A. Knohl, W. Kutsch, D. Loustau, G. Manca, G. Matteucci, F. Miglietta, J. Ourcival, K. Pilegaard, J. Pumpanen, S. Rambal, S. Schaphoff, G. Seufert, J.-F. Soussana, M.-J. Sanz, T. Vesala, and M. Zhao, Reduction of ecosystem productivity and respiration during the european summer 2003 climate anomaly: a joint flux tower, remote sensing and modelling analysis, *Global Change Biology*, *13*, 634–651, 2007.

Robinson, P. J., On a definition of a heat wave, *J. Appl. Meteorol.*, *40*, 762–775, 2001.

Rodwell, M. J., and B. J. Hoskins, Monsoons and the dynamics of deserts, *Q. J. R. Meteorol. Soc.*, *122*, 1385–1404, 1996.

Ruti, P., S. Somot, C. Dubois, S. Calmanti, B. Ahrens, R. Aznar, J. Bartholy, K. Béranger, S. Bastin, J. Brauch, J. C. Calvet, A. Carillo, A. Alias, B. Decharme, A. Dell'Aquila, V. Djurdjevic, P. Drobinski, A. Elizalde Arellano, M. Gaertner, P. Galan, C. Gallardo, F. Giorgi, S. Gualdi, A. Bellucci, A. Harzallah, M. Herrmann, D. Jacob, S. Khodayar, S. Krichak, C. Lebeaupin, B. Lheveder, L. Li, G. Liguori, P. Lionello, O. Baris, B. Rajkovic, F. Sevault, and G. Sannino, The med-cordex initiative: towards fully coupled regional climate system models to study the mediterranean climate variability, change and impact, p. XX, 2012.

Salameh, T., P. Drobinski, and T. Dubos, The effect of indiscriminate nudging time on large and small scales in regional climate modelling: Application to the mediterranean basin, *Q. J. R. Meteorol. Soc.*, *136*, 170–182, 2010.

Santaren, D., P. Peylin, N. Viovy, and P. Ciais, Optimizing a process-based ecosystem model with eddy-covariance flux measurements: A pine forest in southern France, *Global Biogeochemical Cycles*, *21*, GB2013+, doi:10.1029/2006GB002834, 2007.

Schär, C., D. Lüthi, U. Beyerle, and E. Heise, The soil–precipitation feedback: a process study with a regional climate model, *J. Climate*, *12*, 722–741, 1999.

Schär, C., P. L. Vidale, D. Lüthi, C. Frei, C. Haberli, M. A. Liniger, and C. Appenzeller, The role of increasing temperature variability in european summer heatwaves, *Nature*, *427*, 332–336, 2004.

Semenza, J. C., C. H. Rubin, K. H. Falter, J. D. Selanikio, W. D. Flanders, H. L. Howe, and J. L. Wilhelm, Heat-related deaths during the july 1995 heat wave in chicago, *N. Engl. J. Med.*, *335*, 84–90, 1996.

Seneviratne, S. I., D. Lüthi, M. Litschi, and C. Schär, Land-atmosphere coupling and climate change in europe, *Nature*, *443*, 205–209, 2006.

Seneviratne, S. I., T. Corti, E. L. Davin, M. Hirschi, E. B. Jaeger, I. Lehner, B. Orlowsky, and A. J. Teuling, Investigating soil moisture-climate interactions in a changing climate: A review, *Earth-Science Reviews*, *99*, 125–161, 2010.

Shukla, J., C. Nobre, and P. J. Sellers, Amazon deforestation and climate change, *Science*, *247*, 1322–1325, 1990.

Simons, A., S. Uppala, D. Dee, and S. Kobayashi, Era-interim: New ecmwf reanalysis products from 1989 onwards, *ECMWF Newsletter*, *110*, 25–35, 2007.

Simpson, J. E., *Sea breeze and locals winds*, 1989.

Sitch, S., B. Smith, I. C. Prentice, A. Arneth, A. Bondeau, W. Cramer, d. L. S. Kaplan, J a, W. Lucht, M. Sykes, K. Thonicke, and S. Venevski, Evaluation of ecosystem dynamics, plant geography and terrestrial carbon cycling in the lpj dynamic vegetation, *Model. Glob. Change Biol.*, *9*, 161–185, 2003.

Skamarock, W. C., J. B. Klemp, J. Dudhia, D. O. Gill, D. M. Barker, M. G. Duda, X.-Y. Huang, W. Wang, and J. G. Powers, A description of the advanced research wrf version 3, *Tech. rep.*, NCAR, 2008.

Smirnova, T. G., J. M. Brown, and S. G. Benjamin, Performance of different soil model configurations in simulating ground surface temperature and surface fluxes, *Mon. Wea. Rev.*, *125*, 1870–1884, 1997.

Smirnova, T. G., J. M. Brown, S. G. Benjamin, and D. Kim, Parameterization of cold season processes in the maps land-surface scheme, *J. Geophys. Res.*, *105*, 4077–4086, 2000.

Smith, P. C., N. De Noblet-Ducoudré, P. Ciais, P. Peylin, N. Viovy, Y. Meurdesoif, and A. Bondeau, European-wide simulations of croplands using an improved terrestrial biosphere model: Phenology and productivity, *J. Geophys. Res.*, *115*, G01,014, 2010.

Smyth, P., M. Ghil, and K. Ide, Multiple regimes in northern hemisphere height fields via mixture model clustering, *J. Atmos. Sci.*, *56*, 3704–3723, 1999.

Snyder, P. K., C. Delire, and J. A. Foley, Evaluating the influence of different vegetation biomes on the global climate, *Clim. Dyn.*, *23*, 279–302, 2004.

Stauffer, D., and N. Seaman, Use of four-dimensional data assimilation in a limited-area mesoscale model. part i: Experiments with synoptic-mesoscale data, *Mon. Wea. Rev.*, *118*, 1250–1277, 1990.

Stéfanon, M., F. D'Andrea, and P. Drobinski, Heatwave classification over europe and the mediterranean region, *Environmental Research Letters*, *7*(1), 014,023, doi:10.1088/1748-9326/7/1/014023, 2012a.

Stéfanon, M., P. Drobinski, F. D'Andrea, and N. de Noblet-Ducoudré, Effects of interactive vegetation phenology on the 2003 summer heat waves, *J. Geophys. Res.*, *under press*, 2012b.

Stéfanon, M., P. Drobinski, F. D'Andrea, C. Lebeaupin-Brossier, and S. Bastin, Soil moisture-temperature feedbacks at meso-scale during heat waves over france in the hymex/med-cordex simulations, *Clim. Dynam.*, *submitted*, 2012c.

Stéfanon, M., S. Schindler, P. Drobinski, N. de Noblet-Ducoudré, and F. D'Andrea, Impact of anthropogenic land cover change on heat waves : the summer 2003 heat wave as a test bed, *J. Geophys. Res.*, p. in prep, 2012d.

Stohlgren, T. J., T. N. Chase, R. A. Pielke, . Sr, T. G. F. Kittel, and Jill, Evidence that local land use practices influence regional climate, vegetation, and stream flow patterns in adjacent natural areas, *Global Change Biology*, *4*, 495–504, 1998.

Sutton, C., T. M. Hamill, and T. T. Warner, Will perturbing soil moisture improve warm-season ensemble forecasts? a proof of concept, *Mon. Wea. Rev.*, *134*, 3174–3189, 2006.

Tan, P. N., M. Steinbach, and V. Kumar, *Introduction to data mining*, 769 pp., 2006.

Tank, A. M. G. K., J. B. Wijngaard, G. P. Können, R. Böhm, G. Demarée, A. Gocheva, M. Mileta, S. Pashiardis, L. Hejkrlik, C. Kern-Hansen, R. Heino, P. Bessemoulin, G. Müller-Westermeier, M. Tzanakou, S. Szalai, T. Pálsdóttir, D. Fitzgerald, S. Rubin, M. Capaldo, M. Maugeri, A. Leitass, A. Bukantis, R. Aberfeld, A. F. V. van Engelen, E. Forland, M. Mietus, F. Coelho, C. Mares, V. Razuvaev, E. Nieplova, T. Cegnar, J. A. López, B. Dahlström, A. Moberg, W. Kirchhofer, A. Ceylan, O. Pachaliuk, L. V. Alexander, and P. Petrovic, Daily dataset of 20th-century surface air temperature and precipitation series for the european climate assessment, *Int. J. Climatol.*, *22*, 1441–1453, 2002.

Teuling, A. J., S. I. Seneviratne, R. Stockli, M. Reichstein, E. Moors, P. Ciais, S. Luyssaert, B. van den Hurk, C. Ammann, C. Bernhofer, E. Dellwik, D. Gianelle, B. Gielen, T. Grunwald, K. Klumpp, L. Montagnani, C. Moureaux, M. Sottocornola, and G. Wohlfahrt, Contrasting response of european forest and grassland energy exchange to heatwaves, *Nature Geosci.*, *3*, 722–727, 2010.

Trenberth, K. E., Atmospheric moisture recycling: Role of advection and local evaporation, *J. Climate*, *12*, 1368–1381, 1999.

Trier, S. B., C. Fei, and K. W. Manning, A study of convection initiation in a mesoscale model using high-resolution land surface initial conditions, *Mon. Wea. Rev.*, *132*, 2954–2976, 2004.

Trigo, R. M., D. Pozo-Vàzquez, T. J. Osborn, Y. Castro-Díez, S. Gàmiz-Fortis, and M. J. Esteban-Parra, North atlantic oscillation influence on precipitation, river flow and water resources in the iberian peninsula, *Int. J. Climatol.*, *24*, 925–944, 2004.

Uvo, C. B., Analysis and regionalization of northern european winter precipitation based on its relationship with the north atlantic oscillation, *Int. J. Climatol.*, *23*, 1185–1194, 2003.

van den Hurk, B., F. Doblas-Reyes, G. Balsamo, R. Koster, S. Seneviratne, and H. Camargo, Soil moisture effects on seasonal temperature and precipitation forecast scores in europe, *Clim. Dyn.*, *38*, 349–362, 2012.

van der Velde, M., F. Tubiello, A. Vrieling, F. Bouraoui, M. Velde, F. N. Tubiello, A. Vrieling, and F. Bouraoui, Impacts of extreme weather on wheat and maize in France: evaluating regional crop simulations against observed data, *Climatic Change*, doi:10.1007/s10584-011-0368-2, 2011.

Vautard, R., C. Honoré, M. Beekman, and L. Rouil, Simulation of ozone during heat wave and emission control scenarios, *Atmos. Environ.*, *39*, 2957–2967, 2005.

Vautard, R., P. Yiou, F. D'Andrea, N. de Noblet, N. Viovy, C. Cassou, J. Polcher, P. Ciais, M. Kageyama, and Y. Fan, Summertime european heat and drought waves induced by wintertime mediterranean rainfall deficit, *Geophys. Res. Lett.*, *34*, L07,711, doi:10.1029/2006GL028001, 2007.

Vetter, M., G. Churkina, J. M, M. Reichstein, S. Zaehle, A. Bondeau, Y. Chen, P. Ciais, F. Feser, A. Freibauer, R. Geyer, C. Jones, D. Papale, J. Tenhunen, E. Tomelleri, K. Trusilova, N. Viovy, and M. Heimann, Analyzing the causes and spatial pattern of the european 2003 carbon flux anomaly using seven models, *Biogeosciences*, *5*, 561–583, 2008.

Viovy, N., and N. de Noblet-Ducoudré, Coupling water and carbon cycle in the biosphere, *Sci. Géol. Bull.*, *50*, 109–121, 1997.

von Randow, C., A. O. Manzi, B. Kruijt, P. J. de Oliveira, F. B. Zanchi, R. L. Silva, M. G. Hodnett, J. H. C. Gash, J. A. Elbers, M. J. Waterloo, F. L. Cardoso, and P. Kabat, Comparative measurements and seasonal variations in energy and carbon exchange over forest and pasture in south west amazonia, *Theoretical and Applied Climatology*, *78*, 5–26, 2004.

Wahid, A., S. Gelani, M. Ashraf, and M. R. Foolad, Heat tolerance in plants: An overview, *Environmental and Experimental Botany*, *61*, 199–223, 2007.

Warning, U. N. E. P. E., and E. E. Threats, Impacts of summer 2003 heat wave in europe, *Tech. rep.*, 2004.

Weisheimer, A., F. J. Doblas-Reyes, T. Jung, and T. N. Palmer, On the predictability of the extreme summer 2003 over europe, *Geophys. Res. Lett.*, *38*, L05,704, doi:10.1029/2010GL046455., 2011.

Weissmann, M., F. J. Braun, L. Gantner, G. J. Mayr, S. Rahm, and O. Reitebuch, The Alpine Mountain-Plain Circulation: Airborne Doppler Lidar Measurements and Numerical Simulations, *Mon. Wea. Rev.*, *133*, 3095–3109, 2005.

WHO, Heat-waves: risks and responses, *Tech. rep.*, World Health Organisation, 2004.

WHO, Wildfires and heat-wave in the russian federation, *Tech. rep.*, World Health Organisation, 2010.

Wilson, M., and A. Henderson-Sellers, A global archive of land cover and soils data for use in general circulation models, *5*, 119–143, 1985.

Xoplaki, E., Climate variability over the mediterranean, Ph.D. thesis.

Yiou, P., and N. M, Extreme climatic events and weather regimes over the north atlantic: When and where?, *Geophys. Res. Lett.*, *31*, L07,202, doi:10.1029/2003GL019119, 2004.

Zaitchik, B. F., A. K. Macalady, L. R. Bonneau, and R. B. Smith, Europe's 2003 heat wave: a satellite view of impacts and land–atmosphere feedbacks, *Int. J. Climatol.*, *26*, 743–769, 2006.

Zampieri, M., F. D'Andrea, R. Vautard, P. Ciais, N. de Noblet-Ducoudré, and P. Yiou, Hot european summers and the role of soil moisture in the propagation of mediterranean drought, *J. Climate*, *22*, 4747–4758, 2009.

Zheng, X. Y., and E. A. B. Eltahir, A soil moisture rainfall feedback mechanism 2. numerical experiments, *Water Resour. Res.*, *34*, 777–785, 1998.